Viral Aerosol Survivability, Transmission, and Sampling in an Environmental Chamber

A THESIS
SUBMITTED TO THE FACULTY OF THE GRADUATE SCHOOL
OF THE UNIVERSITY OF MINNESOTA
BY

Song Ge

IN PARTIAL FULFILLMENT OF THE REQUIREMENTS
FOR THE DEGREE OF
DOCTOR OF PHILOSOPHY

Thomas H. Kuehn, Adviser

February 2014

Acknowledgements

Firstly, I want to thank my advisor, Dr. Kuehn, for his guidance and patience. Dr. Kuehn was the first person I would talk to when I need help with my work. After every meeting with him, I became more motivated and creative.

I want to thank Dr. Raynor and Dr. Goyal for their advice and help through the progress of the study. I also want to thank Dr. Hogan and Dr. Pui for serving on my thesis committee. Their advice on my research was very important, helping me keep improving my research plan for the more meaningful and fruitful result.

I want to thank Zhili, Jessica, Ankur, Ash, Harsha, Helena, Martha, Sunil, Yogesh, Youssef, and others involved in this study for sharing thoughts and making the study progress smoothly, productively, and joyously. During the process, I gained new skills and knowledge outside mechanical engineering, so I have special thanks to the people in the Diagnostic Lab for their instruction and help.

I want to thank Andy, Ben, Brian, Nick, Nikhil, and Zhili for being a wonderful lab mate in the HVAC lab, and for their friendship.

I want to thank my family for their eternal support to my endeavor, for the familiar warmth from hometown on my road to completing this study.

I want to thank the Minnesota Supercomputing Institute (MSI) for allowing me to use their computing resources for my simulation work. The simulation is an indispensable part in this thesis, and required an advanced computer to run. Without their help, I would need another year to conclude this thesis.

Abstract

Viral aerosol survivability, transmission, and sampling were studied size-selectively in an environmental chamber, which simulated a typical indoor environment featuring a complex flow field and low viral aerosol concentration. MS2, HAdV-1, AIV, SIV, TGEV, and aMPV were tested as surrogates for common human viruses. Live virus titer, total virus concentration, and fluorescence intensity were measured to calculate virus relative recovery and survival.

Because of the low viral aerosol concentration in the chamber, long-term sampling had to be conducted for virus quantification. Long-term sampling performance of the eight-stage non-viable Andersen cascade impactor was tested first. All six viruses were sampled for one and six hours at 25 ˚C and 50% RH. The six-hour samples did not show much higher live virus titers than the one-hour samples, suggesting significant inactivation in the impactor. The six-hour tests did collect much higher total virus concentrations that resulted from PCR analysis. Impactor plate overloading which caused a decrease in sampling efficiency was observed in the six-hour tests.

Due to higher survivability and lower uncertainty, MS2, HAdV-1, and AIV were further tested at different temperatures and humidities. All three viruses had lower inactivation rates at 25 ˚C than at 30 ˚C, but the effect was not significant for HAdV-1. Absolute humidity (AH) was found to be a better predictor of survival than relative humidity (RH). Using AH also removed the significant interaction between temperature and humidity, which exists when RH is used. MS2 and HAdV-1 had the lowest inactivation rates at low AH, and AIV had the lowest inactivation rate at high AH for the AH range from 8.8 to 15.2 g/m^3, which is common in most indoor environments. Future tests are recommended at more extreme humidity levels.

In the UVGI tests, the survival of MS2, HAdV-1 and AIV was significantly reduced by UVGI, showing the good potential of this technology for indoor air disinfection. The inactivation damaged the nucleic acid, which reduced live virus titer and total virus concentration by similar rates. Based on relative recovery, virus inactivation rates due to UVGI were calculated for the three viruses. To quantify the virus susceptibility, a transient numerical simulation was conducted

with Lagrangian particle tracking and log-linear inactivation kinetics. The average susceptibility of MS2 was 0.057 cm^2/mJ with the range for one standard error to be [0.022, 0.098] cm^2/mJ. For HAdV-1, the susceptibility was 0.056 [0.035, 0.079] cm^2/mJ, and for AIV, it was 0.132 [0.031, 0.278] cm^2/mJ. The result suggests that virus susceptibility to UVGI may be similar for air and water environments. Tests for different irradiance and dose levels are recommended to further investigate the inactivation kinetics and verify the numerical model.

In the HVAC filter tests, the overall filtration efficiencies for fluorescein and for total virus were similar, but the filtration efficiency for total virus was significantly higher than that for fluorescein at about 1 μm particle diameter. This result suggests that using fluorescein may not accurately predict the filtration behavior of viruses for the small particles. For the chemical-free filters tested, no significant inactivation of MS2 was found in the filtration process.

More than 95% of the aerosol mass collected was smaller than 4.7 μm, with the mass median diameter of about 1.5 μm. The particle size distribution was affected by suspension medium but not virus. If the nucleic acid was not damaged during a test, the physical loss of virus was better predicted by total virus (PCR) rather than fluorescein, and their difference could be larger for larger viruses. In the nebulizer fluid, no significant virus inactivation was found after the one-hour tests with 20 psi (138 kPa) compressed air, or after the six-hour tests with 10 psi (69 kPa) compressed air. The evaporation effect was more obvious for longer test duration or greater compressed air pressure. The nebulization rate of fluorescein was higher than that of virus.

Table of Contents

List of Tables

List of Figures

List of Abbreviations

ACH	Air changes per hour
ACI	Andersen cascade impactor
AH	Absolute humidity
AHU	Air-handling unit
AIA	American Institute of Architects
AIV	Avian influenza virus
ANOVA	Analysis of variance
ANSI	American National Standards Institute
ASHRAE	American Society of Heating, Refrigerating, and Air-Conditioning Engineers
ATCC	American Type Culture Collection
aMPV	Avian metapneumovirus
BSL-2	Biosafety level-2
CDC	Centers for Disease Control
CFD	Computational fluid dynamics
COV	Coefficient of variation
CPE	Cytopathic effects
CSF	Classical swine fever
Ct	Cycle threshold
CV	Coefficient of variation
DAL	Double agar layer (procedure)
DIF	De-ionized and filtered (water)
dsDNA	Double-stranded DNA
ESP	Electrostatic precipitator
FI	Fluorescence intensity
FMD	Foot-and-mouth disease
HAdV-1	Human adenovirus serotype-1
HEPA	High-efficiency particulate air (filter)
HVAC	Heating, ventilation, and air-conditioning
ID	Inside diameter
IESNA	Illuminating Engineering Society of North America
LSI	Line-source integration (method)
LV	Live virus (titer)
MDCK	Madin-Darby canine kidney (cells)
MEM	Minimum essential medium
MERV	Minimum efficiency reporting value
MOUDI	Micro-orifice uniform deposit impactor
NDV	Newcastle disease virus
NIOSH	National Institute for Occupational Safety and Health
NLV	Norwalk-like virus
OD	Outside diameter
OPC	Optical particle counter
PCR	Polymerase chain reaction (technique)
PFU	Plaque forming unit
PRRSV	Porcine reproductive and respiratory syndrome virus
PSS	Point-source summation (method)
RANS	Reynolds-averaged Navier-Stokes (equations)
Re	Reynolds number

RH	Relative humidity
RR	Relative recovery
RMS	Root-mean-square (residual)
RNG	Renormalization group (turbulence model)
SARS	Severe acute respiratory syndrome
SH	Specific humidity
SIV	Swine influenza virus
ssRNA	Single-stranded RNA
SST	Shear stress transport (turbulence model)
ST	Swine testicular (cell)
TB	Tubercle bacillus or tuberculosis
$TCID_{50}$	Fifty percent tissue culture infective dose
TGEV	Transmissible gastroenteritis coronavirus
TKE	Turbulence kinetic energy
TSA	Trypticase soy agar
TSB	Tryptic soy broth
TV	Total virus (concentration)
ULPA	Ultra low penetration air (filter)
UVGI	Ultraviolet germicidal irradiation
VP	Vapor pressure

1 Introduction

1.1 Transmission of viral aerosol

It has been reported that nearly 60% of human disease infections are caused by viruses (Sattar 1987). An important reason for viruses' strong infectivity is their potential to survive and reach new hosts by different routes after being shed into the environment outside of cells (Sobsey 2003). One of the major transmission routes is by aerosol. Viral aerosol is the specific type of aerosol that carries infectious viruses. When viruses are encased in an aerosol particle, their infectivity is enhanced due to shielding from damaging effects including desiccation and radiation (Tyrrell 1967). Many researchers have found that viral aerosols are capable of traveling up to thousands of kilometers, and maintaining their infectivity for up to several days (Donaldson 1975; Ijaz 1985; Li 2008).

Several disease outbreaks have suggested the importance of the aerosol transmission route. The most famous ones are the 1960s outbreaks of smallpox (Wehrle 1970), the 1990s epidemics of classical swine fever (CSF) in Europe (Dewulf 2000; Weesendorp 2008), and the severe acute respiratory syndrome (SARS) epidemic in the early 2000s (CDC 2003; Olsen 2003; Public Health Agency of Canada 2003; Christian 2004; Yu 2004; Tseng 2005a). Other smaller cases have also shown the possibility of aerosol transmission of influenza, adenovirus, Norwalk-like virus (NLV), small pox, measles, and mumps (Moser 1979; Marks 2000; Tseng 2005a; Blachere 2009; Yao 2009; Yee 2009; Goyal 2011; Yang 2011). Serious study of viral aerosol transmission and infection started in the 1930s (Sattar 1987). Since then the aerosol transmission capacity of many viruses has been tested and proven in experiment. These viruses include adenovirus (Li 2008), CSF virus (Weesendorp 2008), coronavirus (Ijaz 1985), Ebola virus (Jaxx 1994), influenza virus (Andrews 1941; Hood 1963; Mubareka 2009; Munster 2009; van Hoeven 2009), Newcastle disease virus (NDV) (Hopkins 1971), porcine reproductive and respiratory syndrome virus (PRRSV) (Kristensen 2004), and severe acute respiratory syndrome (SARS) virus (Booth 2005; Chu 2005).

Virus transmission in the air includes two modes based on particle size or travelling distance. The aerosol mode is for particles smaller than 5 μm in diameter and capable of traveling indefinitely long distances in the air (Ijaz 1987; Bridges 2003; Blachere 2009; Memarzadeh 2012). Because they are usually dried-out residues of droplets, these particles are called droplet nuclei by some researchers (Bridges 2003; Stetzenbach 2004; Wong 2004; Atkinson 2009). Due to the small sizes, gravitational force is less dominant than diffusion and advection for their motion. In some other studies, the name of droplet nuclei was also used for particles between 5 and 10 μm (Tang 2006; Xie 2007). However, these larger particles are more involved in shorter range transmissions (Mubareka 2009).

It has been reported that particles smaller than 10 μm can be inhaled and retained in the human respiratory system. The smaller the particles, the deeper in the system they can reach. Generally, particles smaller than 5 μm can reach the lower respiratory tract in lungs, and particles greater than 5 μm can be more likely trapped in the upper respiratory tract in nose and throat (Stuart 1973; Ijaz 1987; Hinds 1999; Tellier 2006; Shen 2008; Verreault 2008; Atkinson 2009). Possibly due to the deep deposition, past studies found that the doses needed by aerosol route infections were several orders of magnitude lower than those for nasal route infections (Couch 1966; Ijaz 1987; Tellier 2006; Weber 2008).

The other mode of virus transmission in the air is the large droplet mode for particles usually much larger than 10 μm in diameter (Weber 2008; Mubareka 2009). These particles usually fall to the ground quickly due to the more dominating gravitational effect. They usually travel only a few meters in front of the generation point, and cannot easily reach the lower respiratory tract (Hatch 1964; Hinds 1999). Viruses travelling in the air in either transmission mode may finally deposit on surfaces, potentially causing indirect infection. In fact, for the cases of disease infection, it is usually difficult to distinguish each transmission mode (CDC 2003; Munster 2009).

1.2 Objectives and outline of thesis

Because of the enhanced infectivity and the capability of traveling over long distances while being difficult to detect or predict, viral aerosol transmission has become an important focus of

research. However, possibly due to the great variety of viruses, the uncertainty of measurement, or the differences in test methods, even though a large number of studies have been conducted, the data still do not provide conclusive results in many aspects. This study thus aims to contribute to the database, and more importantly to uncover unknown or ignored facts related to viral aerosol survivability, transmission, and sampling. With this goal in mind, tests were designed to size-selectively study different viruses with different temperatures and humidities, with ultraviolet germicidal irradiation (UVGI), and with the filters designed for common heating, ventilation, and air conditioning (HVAC) systems. All the tests were conducted in an environmental chamber with relatively low viral aerosol concentration to simulate a common indoor situation.

Particle size is a significant factor for viral aerosol transmission, since it affects the amount of virus carried by each particle, the route of travel, and the deposition in the human respiratory system. It was recently suggested that more tests are needed to study the particle size effect on viral aerosol survival and transmission (Yang 2011). In this study, the Andersen cascade impactor (ACI) was used to sample viral aerosols size-selectively. Before studying viral aerosol survivability and transmission, the performance of the ACI was first tested for its long-term sampling capability. The tests estimated the inactivation of collected viruses in the ACI, and determined the suitable sampling duration and other parameters for the rest of the viral aerosol tests.

In the second task, viral aerosols were tested under different temperatures and humidities. Not only the virus survival under different conditions was studied, the effects of the relative humidity and the absolute humidity were also compared.

Viral aerosols were then tested with two UVGI lamps. The inactivation effect of UVGI was assessed and compared for the test viruses. To further investigate the UVGI effect, a numerical model containing flow field simulation, particle tracking, and UVGI irradiance field simulation was developed. With the numerical model, susceptibilities of the test viruses to UVGI were quantified and compared with the published data.

In the last part of this thesis, viral aerosols were tested with two chemical-free HVAC filters of different minimum efficiency reporting values (MERV) using a test duct installed in the environmental chamber. Even though the performance of the test filters at their designed operating condition could not be evaluated due to the non-standard test condition, the tests could still determine whether the filtration efficiency for viruses could be predicted using fluorescein or typical particle counters. If the answer is yes, the current filter test standard or data could be relied on to predict filter performance for viruses as well, and tedious viral aerosol tests would be unnecessary in the future for this purpose.

2 Test facility and instruments

2.1 The environmental chamber

2.1.1 Background

In a lab environment, viral aerosol tests can be conducted in a rotating drum, a wind tunnel, or an environmental chamber. The rotating drum utilizes slow rotational motion (usually several revolutions per minute) to keep viral aerosol suspended and minimize physical loss (Harper 1961; Verreault 2008). Temperature and humidity are usually controlled in it as well. In a wind tunnel, air flow is one-directional, and is usually strictly controlled. These features make it an ideal facility for testing the performance of filters or samplers for viral aerosols (Farnsworth 2006). The environmental chamber is either a scaled or a full-size model of an indoor environment, such as an office, a hospital ward, or a barn. The temperature, humidity, and ventilation rate can usually be adjusted. Various instruments can be placed inside to expand its functionality, or to closely simulate a specific situation. Compared with rotating drums and wind tunnels, the aerosol concentration in the chamber can be much lower due to the larger volume for aerosol dissipation. This means a much larger volume of air may need to be sampled for viral aerosol detection or titration. The complex flow field and low concentration both make the environmental chamber an ideal test facility to simulate viral aerosol survivability, transmission, and sampling in the field.

2.1.2 Structure and specifications

Originally built as a half-scale room, the inside of the environmental chamber is 1.95 m (width) by 1.95 m (depth) by 1.45 m (height) (FIGURE 2.1.1). Its interior was painted white for better illumination.

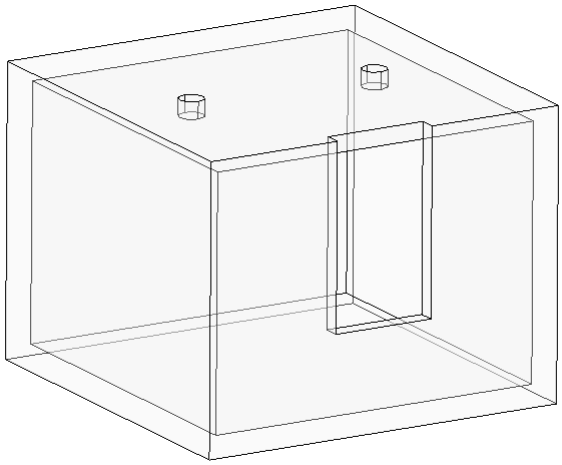

FIGURE 2.1.1 The empty environmental chamber shown without access door, supply air diffuser, return air grille, lamps, and other interior components.

A door made of acrylic glass is located on the front wall of the chamber, and is 1.09 m (height) by 0.57 m (width) (FIGURE 2.1.2). During testing, the door was sealed with rubber gaskets and fastened by three clamps. A pressure tap was placed on the door to monitor the negative pressure in the chamber during a test to prevent the escape of viral aerosol to the surrounding laboratory space. The negative pressure was measured with a Magnehelic differential pressure gauge (Dwyer Instruments, Inc., Michigan City, IN) with a range of 0-0.5 inch water (0-124 Pa) and a resolution of 0.01 inch water (2.5 Pa). In order to safely manipulate the instruments in the chamber during a test, two glove ports with Hypalon gloves were placed on the door. An access window between the two gloves was used to retrieve the nebulizer and impactors from the chamber after each test when the chamber interior had not been disinfected. The operation of the small window strictly followed the requirement for a biosafety level-2 (BSL-2) cabinet in that the inward velocity of at least 75 ft/min (0.38 m/s) must be maintained when the window was open. A test indicated that the minimum velocity was reached when the negative pressure in the chamber was above 0.16 inch water (40 Pa) before the window was opened. For the actual operations with the fan running at its maximum speed, the negative pressure was about 0.36 inch water (90 Pa).

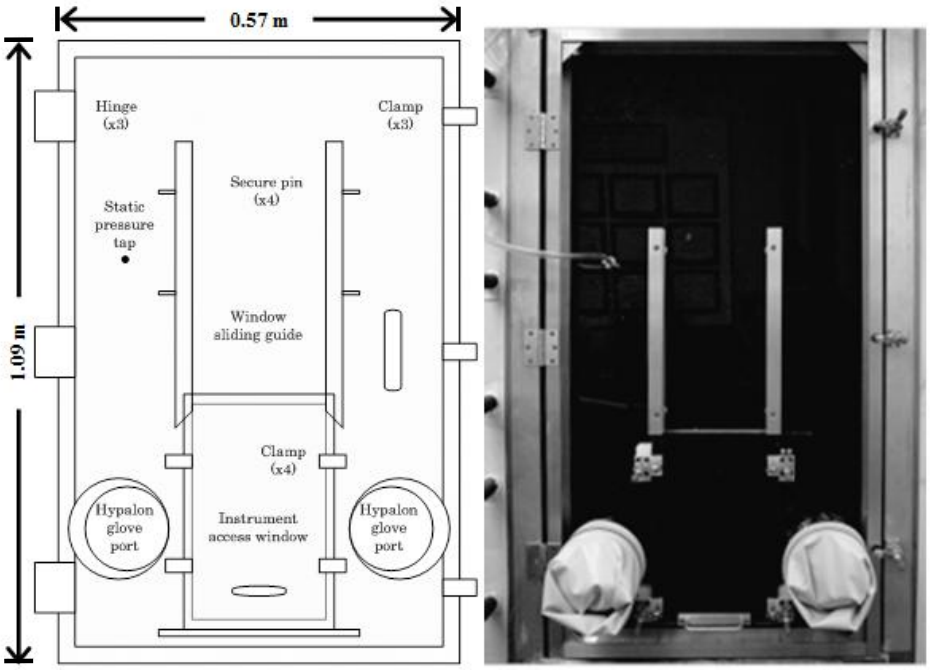

FIGURE 2.1.2 Schematic drawing (left) and photo (right) of the chamber door with two glove ports, an access window, and a static pressure tap.

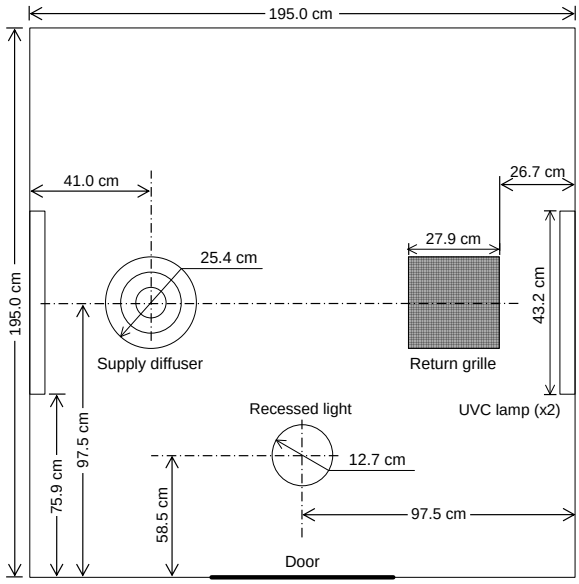

FIGURE 2.1.3 Top view of the chamber, showing the main dimensions and positions of round supply diffuser, square return grille, recessed light, and two UVGI lamps.

The chamber ceiling was built with foam boards covered in plastic sheeting which provided thermal insulation (FIGURE 2.1.3). A round supply diffuser (10 in or 25.4 cm diameter) and a square return grille (11 in or 27.9 cm side length) were placed on the centerline of the ceiling. A recessed light (5 in or 12.7 cm diffuser diameter) was installed to illuminate the chamber interior. The light fixture was thermally insulated, and its diffuser was vapor proof. Two linear fluorescent UVGI lamps using G25T8 tubes (General Electric) with 1 in (2.5 cm) diameter and approximately 17 in (43.2 cm) length were installed for viral aerosol inactivation tests and for chamber disinfection after each test as recommended by several studies (Hocking 2000; Booth 2005; Sze To 2009). The switches for the recessed light and the two UVGI lamps were placed outside the chamber.

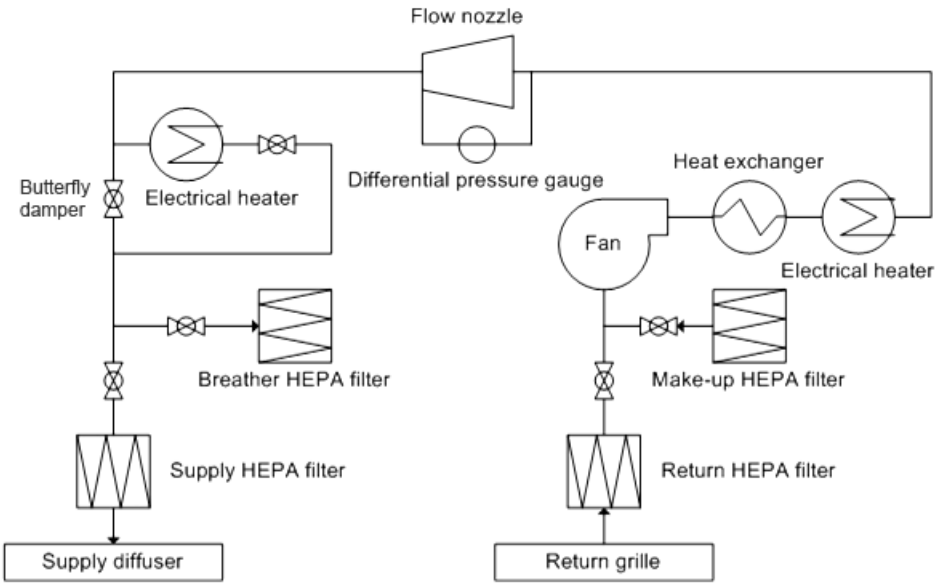

FIGURE 2.1.4 The chamber air handling unit (AHU) for air circulation and conditioning.

In the air handling unit (AHU), PVC pipe and insulated flexible ducts of 6 in (15.2 cm) inside diameter (ID) were used to connect a variable speed fan, four HEPA filters, and other air conditioning equipment (FIGURE 2.1.4). The fan could provide a maximum volumetric flow rate of about 150 ft^3/min (4250 l/min) to the chamber. The instantaneous chamber air flow rate was measured with a nozzle flow meter, which was calibrated using a duct traversing method shortly before the viral aerosol tests (ASHRAE 2009). The air flow rate was calculated from the pressure drop in the nozzle, which was measured with a Magnehelic differential pressure gauge (Dwyer

Instruments, Inc., Michigan City, IN) with a range of 0-5 inch water (0-1244 Pa) and a resolution of 0.1 inch water (24.9 Pa). Four HEPA filters in the AHU were placed on top of the chamber, and used to capture the viral aerosol generated in the chamber. Two of the HEPA filters were for supply and return air. A pre-filter was placed immediately upstream of the return air HEPA filter to collect large particles. The other two HEPA filters were used for make-up and breather air respectively. During the aerosol tests, these two HEPA filters were sealed otherwise the by-pass flow would cause an unknown offset in the measurement of the chamber air flow rate by the nozzle flow meter. A certification test was conducted for the four HEPA filters before the viral aerosol tests, and no leakage was detected.

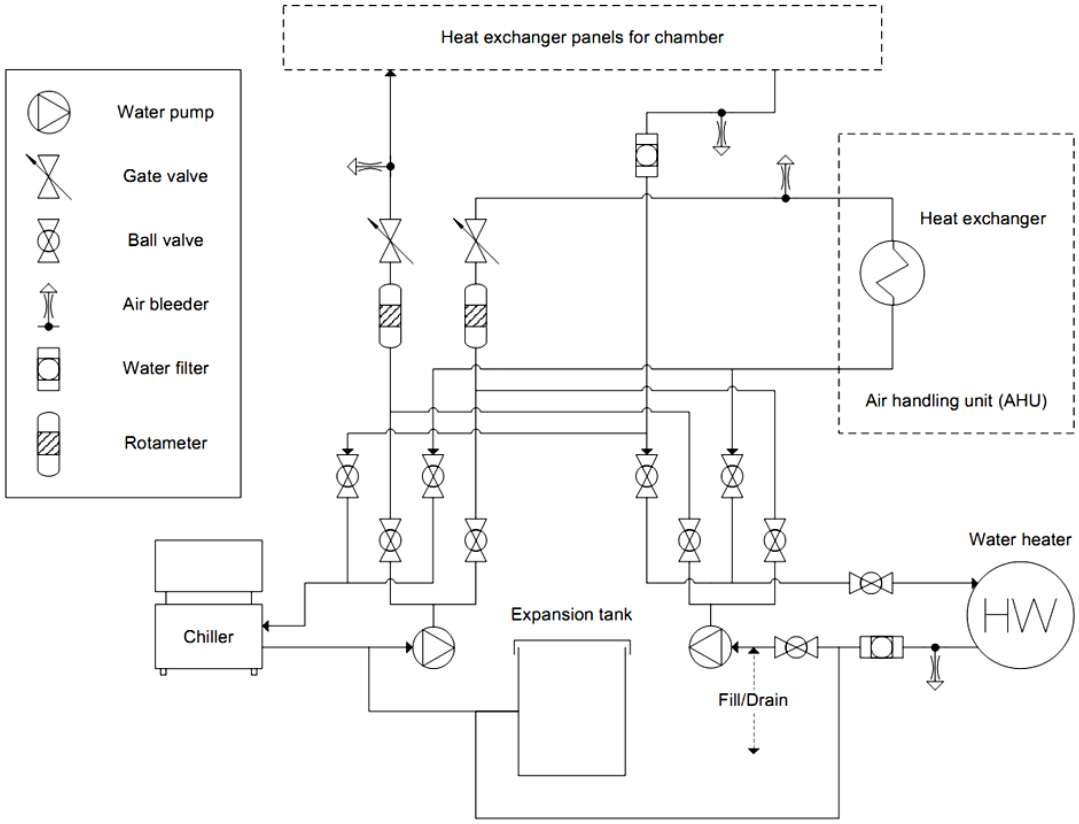

FIGURE 2.1.5 The piping and equipment for glycol solution for heat exchangers.

To change the temperature of the supply air, heat exchanger coils were installed in the AHU (FIGURE 2.1.5). The chamber walls and floor were constructed using plate heat exchangers

attached to aluminum plates that formed all the interior surfaces of the chamber except the ceiling. The working fluid for all the heat exchangers was a 50% ethylene glycol solution in water. A water heater and a water chiller were used to adjust the temperature of the working fluid. Two water pumps circulated the working fluid through the heater and chiller separately. Eight ball valves on the control panel were used to change the passages for hot and cold flows. Before the viral aerosol tests began, the working fluid was replaced, and new filters were installed. The heat exchanger coil in the AHU could operate in combination with the downstream electrical heater (FIGURE 2.1.4) to dry the air when needed. The electrical heater also provided more precise temperature control than using the heat exchanger coil alone.

Type T thermocouples (TFE-T-20, Omega Engineering, Inc., Stamford, CT) were installed on the interior surfaces of the walls, ceiling, floor, the UVGI lamps, and at various locations in the AHU to monitor temperature. A hygrometer (HX94C, Omega Engineering, Inc., Stamford, CT) was installed downstream of the return air HEPA filter to measure both temperature and relative humidity. Before the viral aerosol tests began, the thermocouples were calibrated using an ice bath. The hygrometer accuracy was checked using saturated salt solutions in a temperature controlled container, since it was purchased new with valid factory calibration. The temperature and humidity measured by the hygrometer were taken as the average values in the chamber environment, and were referred to when the test condition was being monitored. The electrical signals from the thermocouples and the hygrometer were picked up by a multimeter (2700, Keithley Instruments, Inc., Cleveland, OH) through a multimeter card (7706, Keithley Instruments, Inc., Cleveland, OH). The signals were first processed by the multimeter, and then transferred to a computer data logging program (Excelinx-1A, Version C04, Keithley Instruments, Inc., Cleveland, OH).

2.2 The Collison nebulizer

In this study, viral aerosols were generated from virus suspensions using a 6-jet modified MRE Collison nebulizer (BGI, Inc., Waltham, MA) (FIGURE 2.2.1). The Collison nebulizer was first introduced by W. E. Collison as the “inhaler” at a meeting of the British Medical Association in 1932 (Collison 1935). Detailed descriptions can be found in several publications (May 1973; Ijaz

1987; First 1998). The Collison nebulizer generates aerosol from liquid using compressed air. During operation, only a small portion of the fluid jets coming out of the nozzles is carried out by the compressed air as aerosol; the rest flows back to the jar (May 1973). Depending on the composition of the liquid medium, the liquid evaporates over time, causing the solution to become more and more concentrated (Chen 2001a; Finley 2001). Evaporation can also lower the nebulizer fluid temperature by 5-10 ˚C below ambient due to latent heat (May 1973; Placke 1990). The changes in concentration and temperature could gradually change the size distribution of the output aerosol, which would be significant for long-term operation (Phipps 1990; Chen 2001a; Hogan 2005). The fluid viscosity and compressed air pressure, however, were not found to significantly affect aerosol size distribution. Increasing fluid viscosity decreases the recirculation rate of the liquid in the jar. Increasing the compressed air pressure increases fluid consumption rate, but a small decrease in aerosol concentration at the nebulizer outlet has been observed (May 1973).

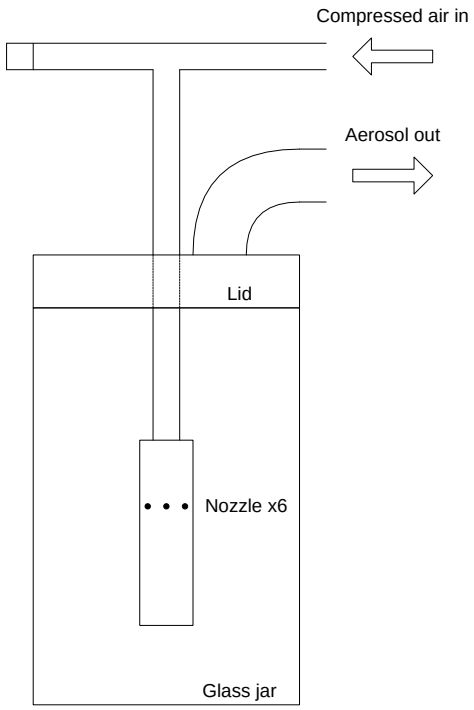

FIGURE 2.2.1 The 6-jet Collison nebulizer used in this study.

2.3 The Andersen impactor

2.3.1 The Andersen impactor

Impactors are among the most common viral aerosol samplers which also include impingers, filters, cyclones, and electrostatic precipitators (Grinshpun 1997; Agranovski 2005; Tseng 2005a; Verreault 2008; Fabian 2009). In a previous study, the eight-stage non-viable Andersen cascade impactor (ACI) (Thermo Scientific, Franklin, MA) (FIGURE 2.3.1) and the micro-orifice uniform deposit impactor (MOUDI) (MSP Co., Shoreview, MN) were compared. Both impactors were capable of size-selectively sampling viral aerosols, but the ACI achieved higher relative recoveries than the MOUDI (Appert 2012). Therefore, the ACI was further tested in the current study, and was used to investigate viral aerosol survivability and transmission. The ACI collected size-selective samples on eight 80 mm aluminum plates. At its standard sampling flow rate of 1 ft^3/min (28.3 l/min), the size range spanned from 0.4 to 10 μm, covering that of droplet nuclei and simulating particle deposition in the human respiratory system (TABLE 2.3.1).

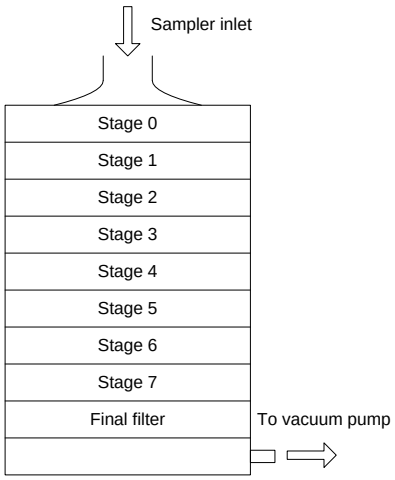

FIGURE 2.3.1 The eight-stage non-viable Andersen cascade impactor (ACI) used in this study.

TABLE 2.3.1 Size ranges of the Andersen impactor stages at the standard sampling flow rate.

Impactor stage	0	1	2	3	4	5	6	7
Lower limit (μm)	9.0	5.8	4.7	3.3	2.1	1.1	0.7	0.4
Upper limit (μm)	10.0	9.0	5.8	4.7	3.3	2.1	1.1	0.7

The ACI has been discussed in several publications (Andersen 1958; Liu 1986; Lodge 1986; Hinds 1999; Verreault 2008). In an ACI stage, aerosol is first accelerated in nozzles upstream of the collection plate. As the air flow direction is abruptly changed due to the presence of the plate, particles which are too large to follow the streamlines impact on the plate and are retained on it. With a number of impactor stages arranged in series, size-selective sampling is achieved. In the ACI, each following impactor stage in the downstream direction has smaller nozzles, gradually increasing the momentum of particles so that smaller particles can be collected. The sampling efficiencies of impactors for viral aerosols were generally satisfactory in previous studies (Verreault 2008). In dry impactors, the impaction force and desiccation may significantly inactivate collected viruses. As a result, an impactor with aqueous medium on the collection plates has been used for viral aerosols (Booth 2005). With the development of quantitative PCR, however, the inactivated viruses can also be detected and quantified. For long-term sampling, the collection plate may be overloaded, resulting in increased particle bounce and decreased sampling efficiency (Agranovski 2005).

2.4 Other equipment and test setup

Most of the test equipment was placed inside the chamber for the viral aerosol tests (FIGURES 2.4.1-2.4.2). The nebulizer and up to two ACIs were secured on a cart close to the chamber door for easy access. The compressed air for the nebulizer was dried, filtered, and regulated outside the chamber. Flexible Tygon tubing was attached to the nebulizer outlet for controlling the aerosol injection position and direction. For aerosol sampling, a 0.75 HP (0.55 kW) vacuum pump (NT10, Oerlikon Leybold Vacuum, Cologne, Germany) was used to draw air through up to two ACIs in this study. One mass flow meter (4100, TSI, Inc., Shoreview, MN) was used to monitor the sampling flow rate through each ACI. All of the mass flow meters were calibrated regularly during the study with a bubble meter (Sensidyne Gilian Gilibrator). Flexible Tygon tubing was attached to the inlet of each ACI to control the sampling position and direction. Neutralizers were not attached to either the nebulizer or the impactors, since their effect on virus inactivation was not known, and might not remain constant over time. One ultrasonic humidifier (Vicks V-5100NS) and one warm mist humidifier (Duracraft DWM250) were placed on the chamber floor to adjust humidity. The vacuum pump, the mass flow meters, and the humidifiers could be turned

on or off individually using a power strip with individual switches in the chamber accessible through the glove ports.

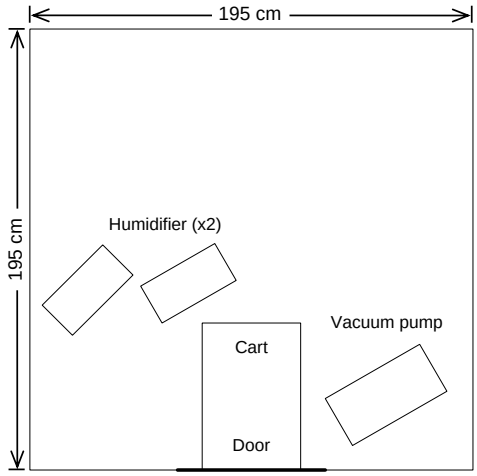

FIGURE 2.4.1 Chamber floor plan with cart, vacuum pump, and two humidifiers.

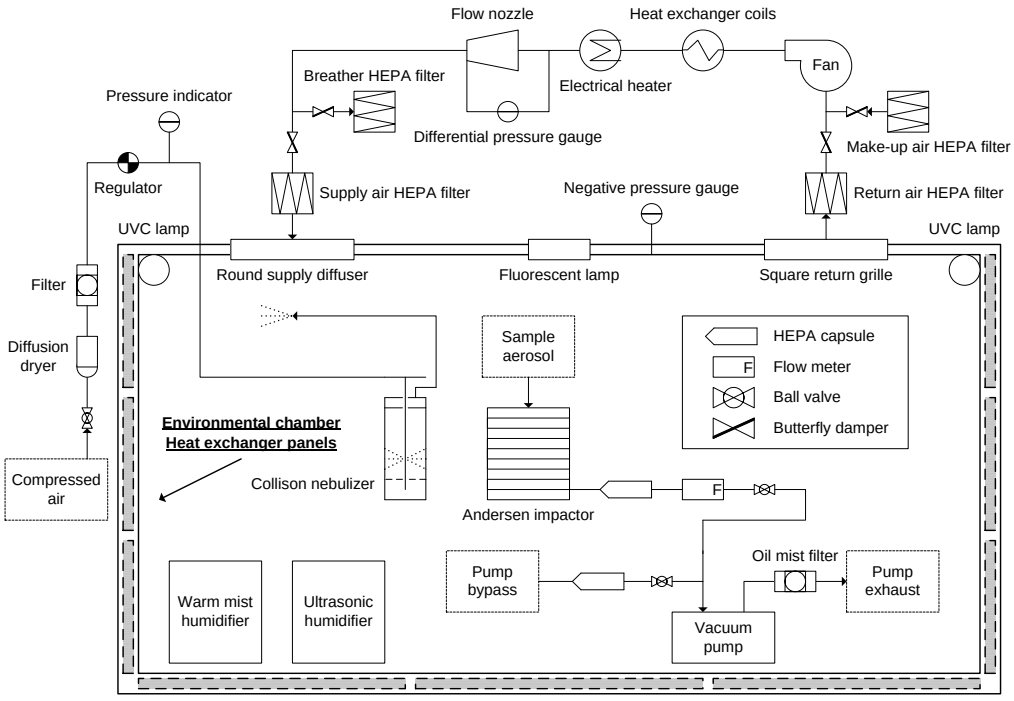

FIGURE 2.4.2 Schematic drawing of the test setup in the environmental chamber.

3 Test method and procedure

3.1 Virus growth and titration

3.1.1 Challenge Viruses

Viruses are the smallest infectious agents with size range from about 20 to 300 nm. They usually consist of a nucleic acid genome surrounded by a protein coat, and some of them have an outer layer called an envelope. Viruses can multiply and are only active within specific host cells (Cox 1995; Tseng 2005b; Verreault 2008). Six viruses were tested in this study: bacteriophage MS2, human adenovirus serotype-1 (HAdV-1), avian influenza virus (AIV), swine influenza virus (SIV), avian metapneumovirus (aMPV), and transmissible gastroenteritis virus (TGEV).

Bacteriophage MS2 has often been used as a general surrogate for animal and human viruses for its innocuousness and fast analysis (Harstad 1965; Hatch 1969; Trouwborst 1972; Comelis 1982; Yahya 1993; van Voorthuizen 2001; Thurston-Enriquez 2003; Cho 2005; Tseng 2005a; Eninger 2008; Verreault 2008; Lee 2009; Woo 2010; Appert 2012). MS2 is a non-enveloped, single-stranded RNA (ssRNA) coliphage with a small (25 to 30 nm) round icosahedral capsid. It has no tail, and is similar to many pathogenic viruses such as enterovirus, calicivirus, rotavirus, poliovirus, rhinovirus, and foot-and-mouth disease (FMD) virus (Cho 2005; Verreault 2008). Compared with the five animal viruses tested in this study, the titer of the MS2 stock was about 5-log higher, which was an advantage for better detection and lower uncertainty. However, as no surrogate is perfect, extrapolation of the MS2 results should be made carefully (Tseng 2005a; Appert 2012).

HAdV-1 is a non-enveloped virus with a diameter of about 70-100 nm (Kennedy 2009). It is the only DNA (double-stranded) virus tested in this study. DNA viruses are usually more stable than RNA viruses (Memarzadeh 2012).

AIV and SIV are both influenza A viruses. Influenza A viruses are spherical and enveloped ssRNA viruses with a diameter of about 80-120 nm. They infect and cause respiratory diseases in humans and other animal hosts including birds, horses, whales, and mink (Lamb 1983). Influenza A viruses are generally host specific, and rarely cross species barriers. However, pigs are postulated to act as a "mixing vessel" for the interspecies transmission of influenza A viruses, including human and avian strains, via the process called genetic reassortment (Kida 1994; Scholtissek 1994, 1998). Due to the physical and genetic similarities, the avian and swine strains could be used as surrogates for human strains (Lamb 1983). The avian strain has also been reported to be hardier than human or swine strains (Mitchell 1968, 1972).

The aMPV is responsible for causing respiratory diseases in turkeys and humans. The virus is typically spherical with a diameter range from 150 to 200 nm, but is also sometimes non-spherical with dimensions from 70 to 600 nm. It is an ssRNA virus enveloped with spikes, and used as the surrogate for human metapneumovirus and human respiratory syncytial virus (Juhasz 1994; Dani 1999; Jones 2000; Broor 2007).

TGEV is a coronavirus, which is named for its surface spikes (Spaan 1988; Cavanagh 1994). It is an enveloped and spherical ssRNA virus with a diameter range from about 100 to 150 nm (including the surface spikes) (Risco 1996). The Purdue strain for pigs used in this study causes gastrointestinal infections in pigs (Tajima 1970; Escors 2001), and shares physical and genetic similarities to human strains (Lamb 1983; Jackwood 2006). It has been used as a conservative surrogate for human severe acute respiratory syndrome (SARS) coronavirus (Casanova 2010).

3.1.2 Preparation of virus stocks

The host cell and preparation procedure depend on virus type. Classified by virus stock preparation method, the six viruses can be divided into two groups: MS2 and the other five animal viruses. For MS2, the virus stock preparation procedure was the same as that in Appert 2012 and Zuo 2013. Briefly, 0.1 ml of MS2 (15597-B1, ATCC) and 1 ml of a log-phase culture of E. coli C-3000 (700891, ATCC) were mixed in top agar tubes at 48 ˚C. The mixture was then poured on trypticase soy agar (TSA) plates. The top agar was allowed to solidify before the plates were inverted and incubated at 37 ˚C for 24 hours. After plaques were confluent (within 24 hours

of incubation), 5 ml of tryptic soy broth (TSB) was added to each plate. After 2 hours at room temperature, the solution was aspirated, centrifuged at 2500 xg for 15 min, and sterile-filtered. The final stock was stored at -80 ˚C in 50 ml aliquots until use.

The procedure of stock preparation was similar for the five animal viruses, but the host cells were different: HAdV-1 (VR-1, ATCC) was propagated in 24-hour old A-549 human lung carcinoma epithelial cells (CCL-185, ATCC), AIV (2007 Maryland H9N9 strain for chicken) and SIV (2010 Minnesota H3N2 strain for pigs) were propagated in Madin-Darby canine kidney (MDCK) cells (CCL-34, ATCC), aMPV was propagated in Vero cells, and the Purdue strain of TGEV was propagated in swine testicular (ST) cells. All these cells were grown in Eagle's minimum essential medium (MEM) (Mediatech, Herndon, VA) supplemented with 8% fetal calf serum, 150 IU/ml penicillin, 150 μg/ml streptomycin, 50 μg/ml neomycin, and 1 μg/ml fungizone. Cells were washed three times with Hanks' balanced salt solution (pH 7.3) before virus inoculation. After inoculation, the virus was allowed to adsorb to the host cells at 37 ˚C for 1 hour. MEM without fetal calf serum was added to the cells before the cells were incubated at 37 ˚C and 5% CO_2 with humidity control. After 4-5 days, when the virus-induced cytopathic effects (CPE) appeared, the cells were first processed with three freeze-thaw cycles (−80/+25 ˚C) and then the viruses were harvested from the infected cells. Cell debris was removed by centrifugation at 2000 xg for 20 min. The supernatant was then divided into 50 ml aliquots and stored at -80 ˚C before being tested.

3.1.3 Cell-culture based titration for live virus titers

The live virus titers of MS2 in virus stock and aerosol samples were determined by the double agar layer (DAL) procedure (Appert 2012). Briefly, top agar tubes (0.7% TSA) were prepared and held in a 48 ˚C water bath. Then, 0.1 ml MS2 sample and 1 ml of log-phase culture of E. coli C-3000 (13706, ATCC) were inoculated into each tube. Serial 10-fold dilutions (-1 to -10) of each sample were prepared in TSB, and were then added to prepared top agar tubes along with the log-phase E. coli. After being gently mixed, and poured onto 1.5% TSA bottom agar plates, the top agar was allowed to solidify, then inverted and incubated at 37 ˚C for 24 h. After incubation, DAL plates were examined for the appearance of plaques, and the results were expressed in plaque forming units per 100 μl (PFU/100 μl) of the sample. The lower detection

limit of this method was 1 PFU/100 µl. For any sample below the detection limit, 0.1 PFU/100 µl was used when needed.

For titration of the five animal viruses, 100 µl from each sample was taken for serial 10-fold dilutions (-1 to -6) in Eagle's MEM with 8% fetal bovine serum. The dilutions were then added to the cell monolayers in 96-well microtiter plates (Nunc, New York) using four wells per dilution. The cells were the same as with virus stock preparation. The inoculated cells in plates were incubated at 37 ˚C and 5% CO_2, and were examined daily with a microscope for five consecutive days for the appearance of virus-induced CPE. Virus titers expressed in $TCID_{50}$/100 µl were calculated by the Karber method (Karber 1931). The lower detection limit was 1 $TCID_{50}$/100 µl. If no virus was detected in any sample, 0.1 $TCID_{50}$/100 µl was used when needed.

3.1.4 Real-time quantitative PCR for total virus concentrations

A major weakness of some traditional viral aerosol samplers including filters and impactors is that a great proportion of the collected virus is inactivated and unculturable. PCR overcomes this problem by detecting the nuclei acid which is usually untouched. It has been reported that PCR can increase virus detection by 5-log compared with culture based titration. Due to its high stability and sensitivity, PCR benefits from longer sampling duration and performs well with low concentration samples (van Elden 2001; Whiley 2003; Richt 2004; Farnsworth 2006; Burton 2007; Li 2008; Verreault 2008; Weesendorp 2008; Yao 2009; Dong 2010; Blachere 2011).

PCR procedures for DNA and RNA viruses were slightly different. For HAdV-1, virus DNA was extracted from 200 µl of sample using the QIAamp DNA Mini kit and protocol (Qiagen, Valencia, CA). For the other five RNA viruses, virus RNA was extracted from 140 µl of sample using the QIAamp viral RNA kit and protocol (Qiagen, Valencia, CA). The DNA/RNA extraction was added to 40 µl elution buffer, and stored at -20 ˚C until being quantified with real-time quantitative PCR which was performed in a Mastercycler Realplex thermocycler (Eppendorf, Hamburg, Germany) using QIAGEN One-Step RT-PCR Kit (Qiagen, Valencia, CA). Forward primers, reverse primers, and probes have been described in Spackman 2002 and O'Connell 2006. Samples were loaded in a 96-well plate and analyzed in duplicate, each of which contained 3 µl of viral RNA/DNA template in the final volume of 20 µl. Standard curves were constructed with

serial 10-fold dilutions of DNA/RNA extracted from the virus stock of known titer. For each run of PCR, standard curve samples and water were used as positive and negative controls respectively. For HAdV-1, the initial cycle of PCR was 50 ˚C preheat for 2 min followed by 95 ˚C heat activation for 15 min. For the five RNA viruses, the initial cycle was 50 ˚C reverse transcription for 30 min followed by 95 ˚C heat activation for 15 min. The thermal amplification cycle for HAdV-1 was 40 cycles of 95 ˚C for 15 s and 56 ˚C for 45 s. For MS2, it was 40 cycles of 95 ˚C for 15 s and 55 ˚C for 45 s. For AIV and SIV, it was 45 cycles of 94 ˚C for 1 s and 60 ˚C for 20 s. For aMPV, it was 40 cycles of 94 ˚C for 15 s and 60 ˚C for 45 s. Finally, for TGEV, it was 40 cycles of 95 ˚C for 15 s and 60 ˚C for 45 s. After each run of quantitative PCR, a cycle threshold (Ct) value for each sample was generated. The amplification efficiency was then determined for each sample using the DART-PCR method to correct the raw Ct values (Peirson 2003). The corrected Ct values were finally projected onto the standard curve to calculate the total virus concentrations, which were also expressed in PFU/100 µl for MS2, or $TCID_{50}$/100 µl for the animal viruses.

3.2 Physical loss of virus and fluorescein tracer

Viral aerosol travelling in the air is subject to both physical and biological losses. Analysis of live virus usually underestimates actual viral aerosol survival (Thorne 1992; Yang 2011). By measuring physical loss of the viral aerosol, the underestimation could be corrected. Physical loss is usually caused by gravitational settling, convection, diffusion, electrostatic attraction, or dilution (Harper 1958), and it can be determined in several ways including direct count using a microscope or a particle counter. A test virus can also be tagged radioactively for measuring its physical loss, but the method needs additional work to address the safety issues. Currently, chemical tracers are more commonly used for such purpose. They have been considered economical, simple, fast, and reliable by several researchers (Ijaz 1987; Agranovski 2005; Verreault 2008). They usually have inert properties and the similar physical loss rates with viruses. More importantly, they do not affect the survival and quantification of test viruses (Harper 1958, 1961; Ijaz 1987; Sattar1987).

In this study, fluorescein was used as the chemical tracer: fluorescein solution was added to the nebulizer fluid before each test, and was collected together with the virus samples. For measurement, each sample was added to a fused quartz cuvette with 3 ml 0.01N NaOH solution in de-ionized and filtered (DIF) water. The cuvettes were then put into a spectrofluorometer (Model RF-5201PC, Shimadzu Scientific Instruments, Columbia, MD) one by one to measure the fluorescence intensity (FI). FI was measured at 515 nm wavelength after excitation at 485 nm. The spectrofluorometer was calibrated with solutions of standardized fluorescein concentrations before this study. Before evaluating each batch of samples, the spectrofluorometer was zeroed with a blank made of DI water. The lower detection limit of this method was 0.1 FI.

In this study, the measurement of the total virus (TV) concentration using quantitative PCR was theoretically an ideal method to calculate the physical loss of virus, given that the RNA/DNA was not damaged significantly. Therefore, both FI and TV were analyzed. The biological loss based on each of them was calculated and compared with each other.

3.3 Relative recovery and survival

As discussed in the previous sections, the total loss of virus in aerosol transmission includes physical loss and biological loss (Songer 1967):

$$1 - Biological\ loss = \frac{1-Total\ loss}{1-Physical\ loss}. \tag{3.3.1}$$

Total loss could be calculated using live virus (LV) titer. Physical loss could be calculated based on either fluorescence intensity (FI) or total virus (TV) concentration, resulting in two biological losses calculated for each sample. To differentiate the two, relative recovery is used for the biological loss based on FI and survival is used for the biological loss based on TV (Hood 1963; Agranovski 2005; Zuo 2013):

$$Relative\ recovery = \frac{(\frac{Impactor}{Nebulizer})_{LV}}{(\frac{Impactor}{Nebulizer})_{FI}}, \tag{3.3.2}$$

$$Survival = \frac{(\frac{Impactor}{Nebulizer})_{LV}}{(\frac{Impactor}{Nebulizer})_{TV}}. \tag{3.3.3}$$

The nebulizer value in EQUATIONS 3.3.2 and 3.3.3 was the geometric mean of the nebulizer samples taken before and after nebulization, namely “pre” and “post”. Because the impactor stage concentrations were normalized using a corresponding nebulizer concentration, virus inactivation during sample transportation or storage should not affect relative recovery or survival. On the other hand, virus inactivation in the chamber, in the impactor, and during the elution process contributed to the final relative recovery and survival. As the elution process was standardized in this study, the inactivation during elution for each virus could be assumed to be constant.

3.4 Test procedure

Before each test, fresh virus stock was carried from the -80 ˚C freezer in the Veterinary Diagnostics Lab (St Paul, MN) to the Environmental Health Lab in the School of Public Health (Minneapolis, MN) to make the nebulizer fluid in a certified biosafety level-2 (BSL-2) cabinet. The volume of nebulizer fluid varied depending on test duration, but the proportion of each ingredient was constant throughout this study. The ingredients were virus stock, 0.05 g/ml fluorescein solution (Fluka, Buchs, Switzerland), and anti-foam Y204 (Sigma Chemical Co., St. Louis, MO). The proportion of the three ingredients was 48:1:0.1. After sufficient mixing, a 1 ml sample was taken from the nebulizer fluid as “pre”, and was kept in an ice box. A clean nebulizer and impactors with clean impaction plates were secured in a biosafety labeled thermal insulated foam box, and carried to the environmental chamber in the HVAC lab in the Department of Mechanical Engineering (Minneapolis, MN) for the tests.

In the HVAC lab, the chamber air handling unit and data logging system were first started to allow for warm-up and necessary adjustment. When the desired test conditions were reached, the nebulizer and impactors were taken out of the insulated box, placed in the chamber through the access window, connected to the appropriate tubing, and started simultaneously. After the desired test duration, the nebulizer and impactors were stopped simultaneously, their exterior surfaces wiped with 70% alcohol wipes using the glove ports in the door, removed from the chamber through the access window, secured inside the insulated box, and transported back to the Environmental Health Lab.

Using the biosafety cabinet in the Environmental Health Lab, a 1 ml sample from the nebulizer was first taken as "post". The plates were then removed from the impactors to be eluted with elution buffer. The elution buffer stock was prepared by adding 15 g 3x beef extract powder, and 1.875 g (0.05 M) glycine amino acid (molecular weight 75.07) into 500 ml DIF water. The solution was mixed and autoclaved in the Veterinary Diagnostics Lab, and kept at 4 ˚C before use. For plate elution, all plates were first removed from the impactors, and placed in petri-dishes. Each plate was eluted with 1 ml elution buffer using a clean cell scraper. After having scraped all areas at least twice, and removed all visible dots on the plate, the eluate was collected with a pipette and transferred to a 1.5 ml Eppendorf tube. A blank Andersen impactor plate served as the blank control and was also eluted using the same procedure. The elution process was standardized to improve test repeatability. Each sample was divided into two parts: a 50 µl aliquot for fluorescein measurement, and the rest for virus titration. The fluorescein part was stored at 4 ˚C in the same lab. The remaining samples were transported to the Veterinary Diagnostics Lab in an ice box, and stored at -80 ˚C before titration.

Both the biosafety cabinet in the Environmental Health Lab and the environmental chamber in the HVAC lab were disinfected after each test. Cell scrapers, impactor plates, petri-dishes, and the nebulizer were washed with 1:32 bleach solution, rinsed with DIF water at least twice, and kept in a clean pan to dry for the next test. The chamber was disinfected with the UVGI lamps on and the ventilation system operating for at least 3 hours. The next test was conducted at least 15-hr after the end of the disinfection process. The disinfection effectiveness was verified by leaving several stainless steel plates in petri-dishes in the chamber throughout the entire test and disinfection process. No live virus was found on any of the plates, indicating that most surfaces were properly disinfected. The disinfection effectiveness was also verified by doing a one-hour sampling test without aerosol generation and operation of the chamber AHU. No virus was detected in the impactor samples, indicating that the air was virus free. A small amount of viruses deposited on surfaces might not be inactivated by UVGI due to a blocking effect by equipment or shielding effect. A previous study also showed that about 3% to 10% of deposited viruses were protected from UVGI (Sagripanti 2011). In order to prevent interference between different types of viruses for titration, additional chamber interior disinfection was carried out using bleach spray and manual wiping of the interior surfaces after each group of tests for the same virus. Additionally, the exterior surfaces of the instruments inside the chamber were wiped with 70% isopropanol

wipes, and the washable parts were washed with 1:32 bleach solution. Remaining viruses still not inactivated should not be resuspended, or cause any test error in the rest of the study.

4 One-hour and six-hour viral aerosol sampling tests

4.1 Introduction

In a previous study, the ACI collected viral aerosols size-selectively with satisfactory concentration and recovery on most impactor stages in 15-minute sampling tests using the same viral aerosols (Appert 2012). Before testing the viral aerosol survivability and transmission in the environmental chamber, however, it was necessary to know how the ACI would perform in the low concentration environment, and how well the collected viruses would survive during the long-term sampling. The goal of this group of tests was to resolve the above questions, and to determine the proper sampling duration and viruses to be used for the remainder of this study.

4.2 Modification and test of the nebulizer

During long-term nebulization, the fluid level in the nebulizer dropped continuously, making it necessary to adjust the height of the nebulizer nozzle stem periodically for continuous aerosol generation. To make this task easier, a modification to the nebulizer was done by attaching six flexible plastic tubes to the end of the stem to extend its effective length (FIGURE 4.2.1). This modification significantly reduced the frequency of adjustment during a test. However, it could also affect the consumption rate of nebulizer fluid, thus the modified nebulizer was tested.

The most important parameter for viral aerosol generation rate from a specified fluid is the compressed air pressure. If the pressure is too high, virus could be significantly inactivated due to excess stress, or the nebulizer fluid would be used up earlier than the planned test duration. The maximum volume in the nebulizer for proper operation was about 150 ml, thus the fluid consumption rate should be less than 25 ml/hr for the six-hour tests. A nebulization rate test was conducted with the nebulizer fluid identical with viral aerosol tests, except using MEM and TSB

to replace the corresponding virus stock. Each condition was tested five times. With the tubes attached, for 10 psi (69 kPa) compressed air, the fluid consumption rate was 15+/-1.5 ml/hr, and for 20 psi (138 kPa) the rate was 25+/-2 ml/hr. Without tubes, for 10 psi (69 kPa) the rate was 11+/-1 ml/hr. Therefore, using 20 psi (138 kPa) may lead to a lack of nebulizer fluid approaching the end of a six-hour test, and 10 psi (69 kPa) was chosen for this group of tests. In a previous study using the same nebulizer fluid (Appert 2012), 20 psi (138 kPa) was used for 15 minutes of nebulization, and no significant inactivation of virus in the nebulizer fluid was found. In another study, viral aerosols were generated from the same nebulizer for 10 min using the compressed air pressure of 180 kPa, and no significant inactivation of virus was found as well (Ijaz 1987). Therefore, virus inactivation due to nebulization stress should also be negligible in this group of tests.

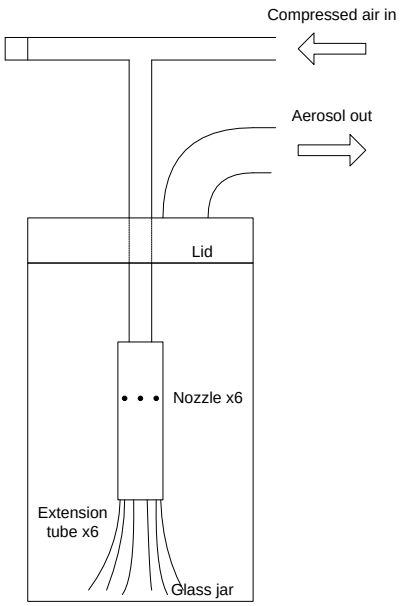

FIGURE 4.2.1 Modified 6-jet Collison nebulizer with extension tubes used for this study.

In addition, the nebulizer test results showed that the attached tubes increased the fluid consumption rate. Although the mechanism is not clear, it is a desirable outcome for the higher concentrations preferred in the impactor samples. To make all the test results comparable, the tubes were always attached throughout this study.

4.3 Test method

All six viruses (MS2, HAdV-1, AIV, SIV, aMPV, and TGEV) were tested for one and six hours. The long test durations offered good challenges to test the impactor's performance of longer-term sampling.

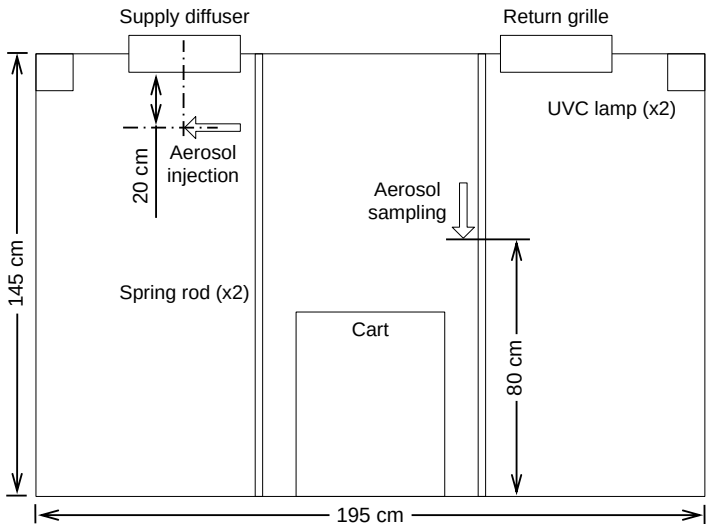

FIGURE 4.3.1 The chamber center plane schematic showing the main dimensions and positions of viral aerosol injection and sampling.

As shown in FIGURE 4.3.1, viral aerosol was injected 20 cm below the center of the supply diffuser and directed toward the left chamber wall. This was to avoid direct movement of the injected aerosol toward the return air grille without being circulated in the chamber. Viral aerosol was sampled 80 cm above the floor in the downward direction below the return grille. Flexible Tygon tubing of 1/2 in (1.27 cm) inside diameter (ID), and 3/4 in (1.91 cm) outside diameter (OD) was used to control the positions and directions of aerosol injection and sampling. The length of the Tygon tubing used for injection was 55 in (139.70 cm), and that for sampling was 53 in (134.62 cm). The Tygon tubing was attached to two spring rods that assisted in positioning them. The overall sampling efficiency was estimated to be greater than 85% for impactor stages 3-7 (0.4-4.7 μm), greater than 90% for impactor stages 4-7 (0.4-3.3 μm), and greater than 95% for impactor stages 5-7 (0.4-2.1 μm) (Appendix A).

For these tests, the air change rate in the chamber was 15 air changes per hour (ACH), which is similar to some typical indoor environments, such as a computer room, a dining room, or an examination room in the hospital (Atkinson 2009; Blachere 2009). The chamber volume was approximately 6 m^3, thus the corresponding volumetric flow rate was about 53 ft^3/min (1500 l/min). At this ventilation rate, the negative pressure of the chamber environment compared to lab was greater than 25 Pa, which was recommended by the American Institute of Architects to ensure containment of generated viral aerosol (Garner 1996; AIA 2001). The thermal condition was maintained at 25 ˚C with a variation less than 1 ˚C, and 50% RH with a variation less than 5%. The nebulizer compressed air pressure was 10 psi (69 kPa) as was determined in the previous section. The nebulizer fluid volume was 49.1 ml for one-hour tests, and was increased to 147.3 ml for the six-hour tests. The proportion among virus stock, fluorescein dye (50 mg/ml), and anti-foam was always 48:1:0.1 by volume.

The tests were conducted in triplicate, and the test order was randomized. Analysis of uncertainty and analysis of variance (ANOVA) were carried out on a logarithmic scale as variance was assumed to be log-normally distributed about the mean. ANOVA was performed in R (Version 2.15.0, the R Foundation for Statistical Computing) to test the significance of the factors including virus type, test duration, particle size, and their interactions to responses including relative recovery and survival. A factor or an interaction was significant if its p-value was smaller than 0.05. Considering accuracy, ANOVA was performed for samples from impactor stages 3-7 only, as for impactor stages 0-2, their concentrations were much lower, and uncertainties were much higher. For the figures, however, the results for all impactor stages are shown whenever possible.

4.4 Results and discussion

4.4.1 Viability analysis of impactor stage samples

Live virus (LV) titer from the impactor stage samples normalized with respect to the nebulizer fluid titer was related to the total loss:

$$\left(\frac{Impactor}{Nebulizer}\right)_{LV} = 1 - Total\ loss. \tag{4.4.1}$$

Size distributions of normalized live virus titer are plotted in FIGURE 4.4.1. The pooled relative standard deviations in TABLE 4.1.1 were calculated by assuming that the uncertainty did not depend on particle size (Appendix D). From these results, MS2 had the lowest total loss, followed by AIV and HAdV-1. These three viruses also had much lower uncertainties than SIV, TGEV, and aMPV. To compare the viruses and test durations more clearly, the overall normalized live virus titer for all impactor stages for each virus is shown in FIGURE 4.4.2. The p-values for normalized live virus titer are shown in TABLE 4.4.2. Virus type, particle size, and test duration were all significant factors. No interaction was significant, which means the size distribution of live virus did not significantly change with test duration or virus type.

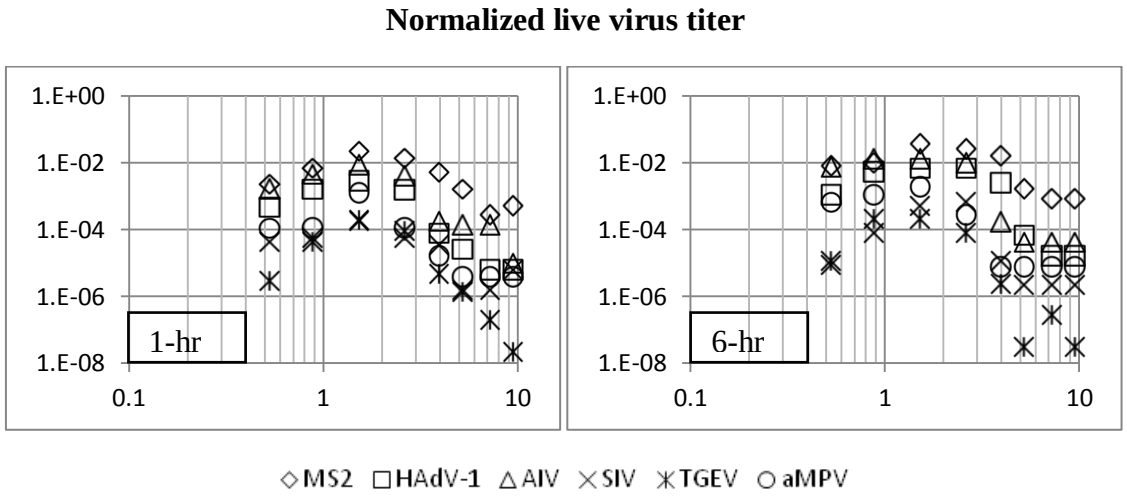

FIGURE 4.4.1 Normalized live virus titer (dimensionless, vertical axes) versus particle aerodynamic diameter [μm] (horizontal axes) for all six viruses for one-hour and six-hour tests.

TABLE 4.4.1 Pooled relative standard deviation for each data series shown in FIGURE 4.4.1.

Virus	MS2	HAdV-1	AIV	SIV	TGEV	aMPV
1-hr	+100.4% -50.1%	+318.1% -76.1%	+320.4% -76.2%	+1246.8% -92.6%	+1029.2% -91.1%	+848.7% -89.5%
6-hr	+130.7% -56.7%	+112.9% -53.0%	+187.5% -65.2%	+2212.4% -95.7%	+3050.5% -96.8%	+467.6% -82.4%

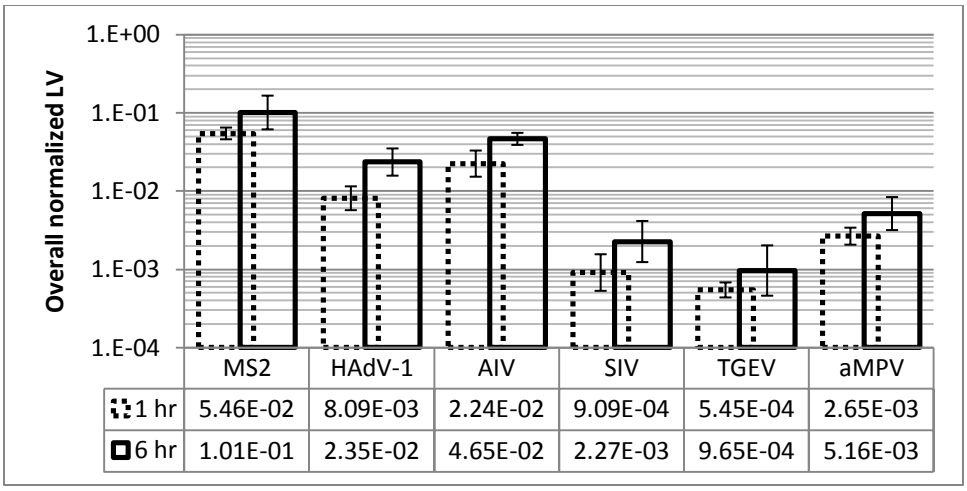

FIGURE 4.4.2 Overall normalized live virus (LV) titer (dimensionless) for all six viruses for one-hour and six-hour tests with error bars showing standard errors.

TABLE 4.4.2 P-values for normalized live virus titer with significant factors in bold.

Factor	Virus	Size	Duration	V:S	V:D	S:D	V:S:D
P-value	**<0.001**	**<0.001**	**0.001**	0.268	0.736	0.916	0.905

Total virus (TV) concentration or fluorescence intensity (FI) of the impactor samples normalized with respect to the nebulizer fluid value was related to the physical loss:

$$\left(\frac{Impactor}{Nebulizer}\right)_{TV\ or\ FI} = 1 - Physical\ loss. \quad (4.4.2)$$

For normalized fluorescence intensity, both the size distributions (FIGURE 4.4.3 and TABLE 4.4.3) and the overall values (FIGURE 4.4.4) were very similar for the test viruses. The uncertainties of the normalized fluorescence intensity were much smaller than those of the normalized live virus titer. ANOVA (TABLE 4.4.4) shows that, however, virus type was a significant factor. By further comparing the viruses, MS2 was significantly different from HAdV-1 (p=0.001), but the other four animal viruses were not (p=0.527 for AIV, 0.979 for SIV, 0.166 for TGEV, and 0.142 for aMPV). The interaction between virus type and particle size was not significant, meaning that the particle size distribution was not significantly affected by virus type for particles smaller than 4.7 μm. However, it seems from FIGURE 4.4.3 that the five animal viruses had similar particle size distributions, but MS2 was a slightly different, especially for impactor stages 0-2 (>4.7 μm), which were not considered in ANOVA. The differences between

MS2 and the animal viruses could be due to the different types of suspension media, as TSB was used for MS2, while MEM was used for the animal viruses. For the five animal viruses, virus type did not seem to affect either particle size distribution or overall particle size as concluded in some past studies (Ijaz 1987; Xu 2003; Hogan 2005).

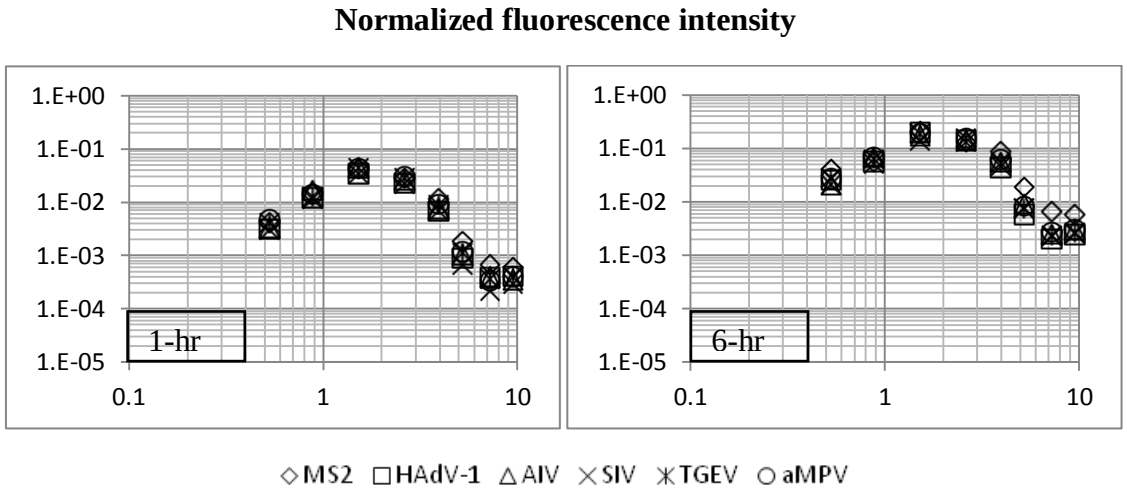

FIGURE 4.4.3 Normalized fluorescence intensity (dimensionless, vertical axes) versus particle aerodynamic diameter [μm] (horizontal axes) for all six viruses for one-hour and six-hour tests.

TABLE 4.4.3 Pooled relative standard deviation for each data series shown in FIGURE 4.4.3.

Virus	MS2	HAdV-1	AIV	SIV	TGEV	aMPV
1-hr	+31.1% -23.7%	+42.6% -29.9%	+44.0% -30.5%	+17.7% -15.0%	+12.9% -11.4%	+11.2% -10.1%
6-hr	+48.6% -32.7%	+67.0% -40.1%	+8.5% -7.9%	+8.5% -7.8%	+14.5% -12.6%	+18.8% -15.8%

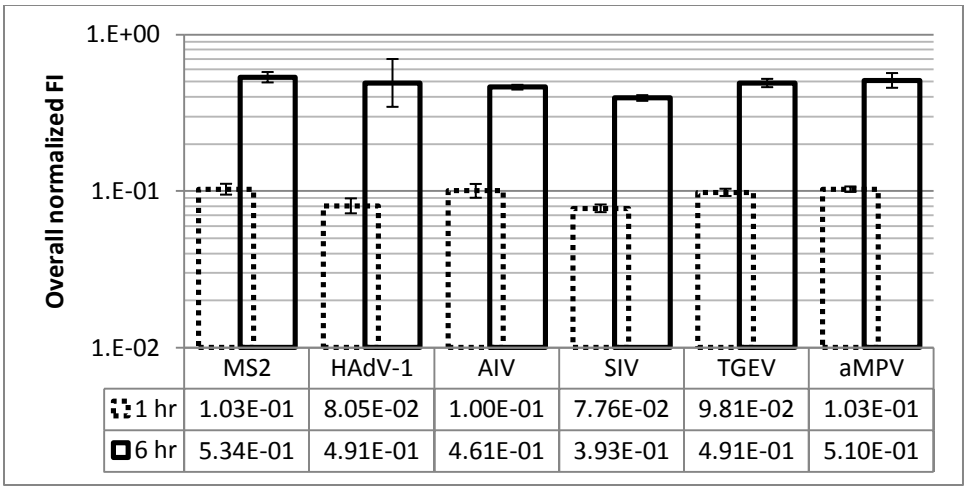

FIGURE 4.4.4 Overall normalized fluorescence intensity (FI) (dimensionless) for all six viruses for one-hour and six-hour tests with error bars showing standard errors.

TABLE 4.4.4 P-values for normalized fluorescence intensity with significant factors in bold.

Factor	Virus	Size	Duration	V:S	V:D	S:D	V:S:D
P-value	**<0.001**	**<0.001**	**<0.001**	0.373	0.829	**<0.001**	0.989

Particle size and test duration were both significant factors for normalized fluorescence intensity as expected. No interactions were significant except for that between particle size and test duration, meaning that the particle size distribution was different for one-hour and six-hour tests. To help explain this, the normalized fluorescein size distributions for both test durations are plotted in FIGURE 4.4.5 using the data for all the viruses. The normalized particle size distributions were calculated by normalizing the fluorescence intensity of each impactor stage by the sum of all impactor stage values. The figure shows that the particle size distributions for the six-hour tests were more uniform than those for the one-hour tests according to the lower peak on impactor stage 5. One possible reason was that the aerosol collected on impactor stage 5 in the six-hour tests overloaded the collection plate as stated in Agranovski 2005. Plate overloading caused the unevenness on its surface, and could negatively affect its collection efficiency. During the elution process, the unevenness was observed in the six-hour test samples. Another possibility could be that the size distribution of the generated aerosol from the nebulizer changed over time, as the nebulizer fluid was gradually concentrated.

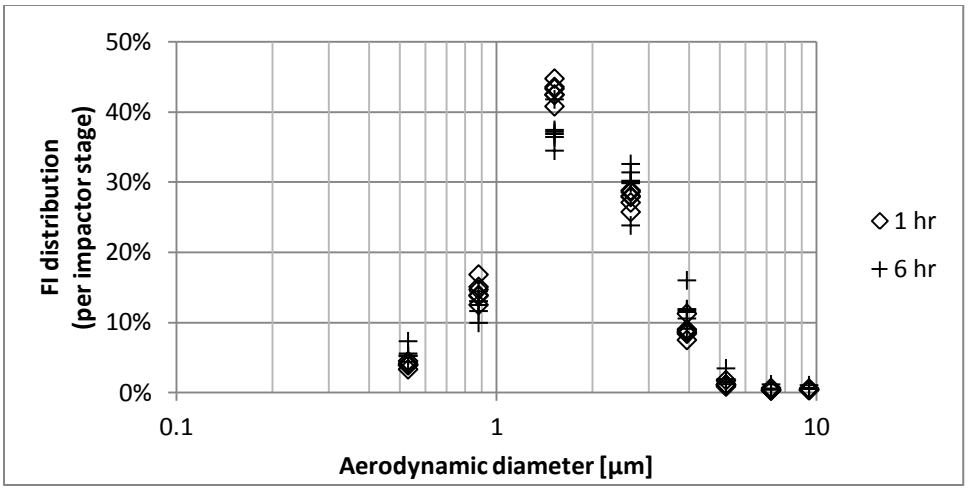

FIGURE 4.4.5 Fluorescence intensity (FI) distribution (per impactor stage) plotted with data of all six viruses (labels not shown) for one-hour and six-hour tests.

TABLE 4.4.5 Pooled relative standard deviation for each virus and test duration in FIGURE 4.4.5.

Virus	MS2	HAdV-1	AIV	SIV	TGEV	aMPV
1-hr	+19.4% -16.2%	+24.2% -19.5%	+28.7% -22.3%	+11.9% -10.6%	+8.5% -7.8%	+6.6% -6.2%
6-hr	+46.5% -31.8%	+57.7% -36.6%	+8.9% -8.2%	+3.9% -3.7%	+7.0% -6.5%	+9.1% -8.4%

The results of normalized total virus concentration are presented in the same way as for live virus titer and fluorescence intensity in FIGURES 4.4.6-4.4.7 and TABLES 4.4.6-4.4.7. From ANOVA (TABLE 4.4.7), virus type was a significant factor. It is the same as the normalized fluorescence intensity result: when compared with HAdV-1, MS2 was significantly different ($p<0.001$), but the other viruses were not ($p=0.244$ for AIV, 0.928 for SIV, 0.460 for TGEV, and 0.464 for aMPV). From the size distributions (FIGURE 4.4.6 and TABLE 4.4.6), it can be seen that the physical loss of MS2 was smaller than those of the five animal viruses for all impactor stages. This was different than the fluorescein result where MS2 had smaller losses only for the larger particles. By comparing FIGURES 4.4.6 and 4.4.3, it can be seen that the physical losses of MS2 were not very different, while for the five animal viruses their physical losses calculated using total virus were greater than those calculated using fluorescein, indicating that the actual physical loss of virus may not be accurately represented by fluorescein, and the accuracy would be lower for larger viruses. For the other ANOVA results (TABLE 4.4.7), particle size and test duration were both

significant factors as expected. No interactions were significant, meaning that the size distribution for particles smaller than 4.7 μm was not significantly affected by either virus type or test duration. In contrast with the fluorescein result, the decrease in collection efficiency on impactor stage 5 was not significant, probably due to the greater uncertainty associated with the PCR measurements.

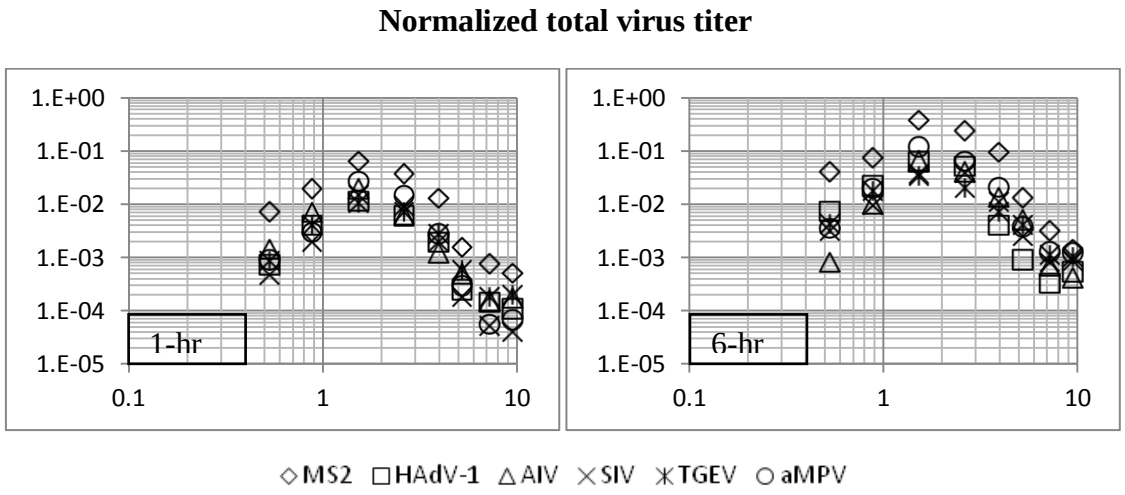

FIGURE 4.4.6 Normalized total virus concentration (dimensionless, vertical axes) versus particle aerodynamic diameter [μm] (horizontal axes) for all six viruses for one-hour and six-hour tests.

TABLE 4.4.6 Pooled relative standard deviation for each data series shown in FIGURE 4.4.6.

Virus	MS2	HAdV-1	AIV	SIV	TGEV	aMPV
1-hr	+57.7% -36.6%	+105.3% -51.3%	+139.8% -58.3%	+69.1% -40.9%	+80.6% -44.6%	+49.9% -33.3%
6-hr	+147.0% -59.5%	+87.4% -46.6%	+162.7% -61.9%	+147.4% -59.6%	+55.4% -35.6%	+61.0% -37.9%

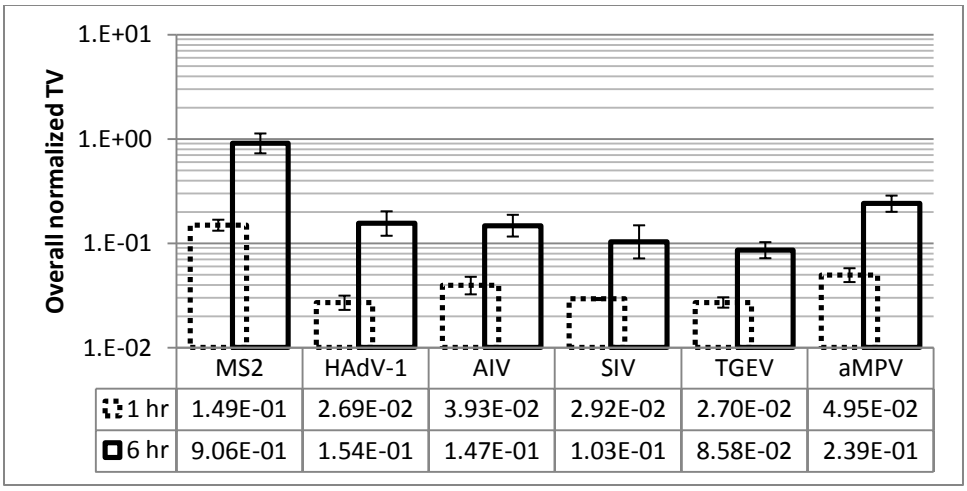

FIGURE 4.4.7 Overall normalized total virus (TV) concentration (dimensionless) for all six viruses for one-hour and six-hour tests with error bars showing standard errors.

TABLE 4.4.7 P-values for normalized total virus concentration with significant factors in bold.

Factor	Virus	Size	Duration	V:S	V:D	S:D	V:S:D
P-value	**<0.001**	**<0.001**	**<0.001**	0.189	0.183	0.699	**0.049**

Based on live virus titer, total virus concentration, and fluorescence intensity for all viruses, stage 5 (1.1-2.1 μm) of the Andersen impactor collected about 40% of the total amount collected, and impactor stages 3-7 (0.4-4.7 μm) collected more than 95%, indicating that the most particles collected were small droplet nuclei that could be inhaled and retained in the lower tract of the human respiratory system. This size distribution is similar to some previous studies (Yang 2011; Appert 2012).

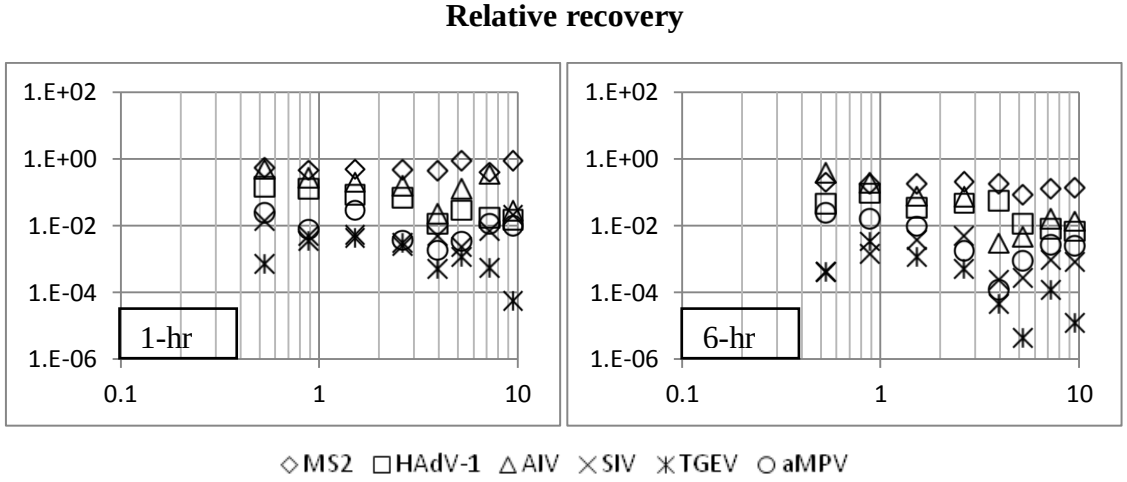

FIGURE 4.4.8 Relative recovery (dimensionless, vertical axes) versus particle aerodynamic diameter [μm] (horizontal axes) for all six viruses for one-hour and six-hour tests.

TABLE 4.4.8 Pooled relative standard deviation for each data series shown in FIGURE 4.4.8.

Virus	MS2	HAdV-1	AIV	SIV	TGEV	aMPV
1-hr	+96.0% -49.0%	+320.1% -76.2%	+457.8% -82.1%	+1208.3% -92.4%	+1030.9% -91.2%	+797.4% -88.9%
6-hr	+133.6% -57.2%	+90.8% -47.6%	+197.0% -66.3%	+2093.6% -95.4%	+2911.6% -96.7%	+521.1% -83.9%

Relative recovery and survival were calculated by isolating physical loss from total loss as discussed in Chapter 3. For relative recovery, size distributions are plotted in FIGURE 4.4.8 with the uncertainties given in TABLE 4.4.8. Overall relative recovery calculated using the sum of live virus titer and sum of fluorescence intensity from all impactor stages is plotted in FIGURE 4.4.9. The corresponding ANOVA p-values are listed in TABLE 4.4.9. For survival, corresponding plots and tables are presented in FIGURES 4.4.10-4.4.11 and TABLES 4.4.10-4.4.11.

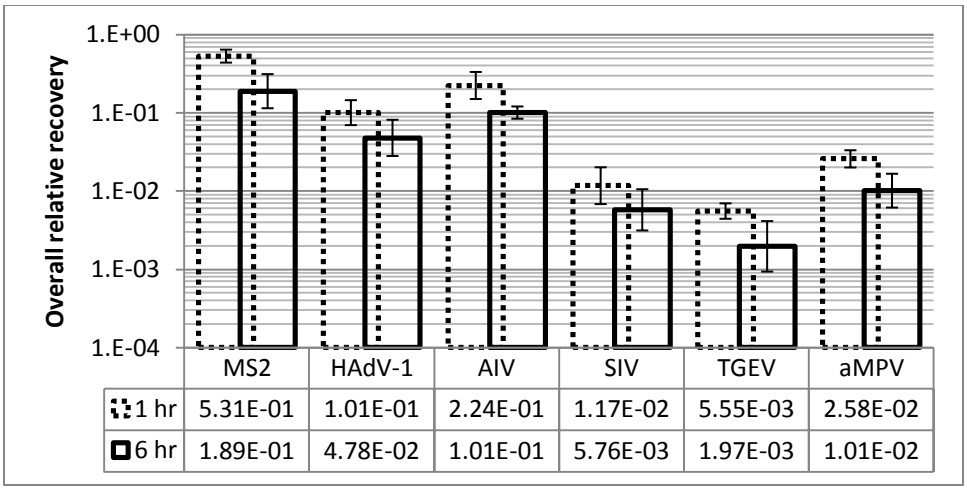

FIGURE 4.4.9 Overall relative recovery (dimensionless) for all six viruses for one-hour and six-hour tests with error bars showing standard errors.

TABLE 4.4.9 P-values for relative recovery with significant factors in bold.

Factor	Virus	Size	Duration	V:S	V:D	S:D	V:S:D
P-value	**<0.001**	**<0.001**	**0.001**	0.367	0.814	0.757	0.911

ANOVA results were similar for relative recovery and survival. Virus type was significant; MS2, HAdV-1, and AIV were higher in both parameters than SIV, TGEV, and aMPV. Test duration was significant; the one-hour tests showed higher relative recovery and survival results than the six-hour tests, showing obvious virus inactivation in the impactor. Particle size was also significant. It can be seen from FIGURES 4.4.8 and 4.4.10 that both parameters of the animal viruses tended to decrease with the increasing particle size. The trend, however, was not obvious for MS2. This difference agrees with Appert 2012. No interaction between the above factors was significant, showing that the size distributions of either relative recovery or survival were similar for all viruses and both test durations. By comparing FIGURES 4.4.9 and 4.4.11, it can be seen that except for MS2, virus survival was generally greater than relative recovery. This was because that the same physical loss measured with total virus was greater than that measured with fluorescein. The discrepancy might depend on virus size.

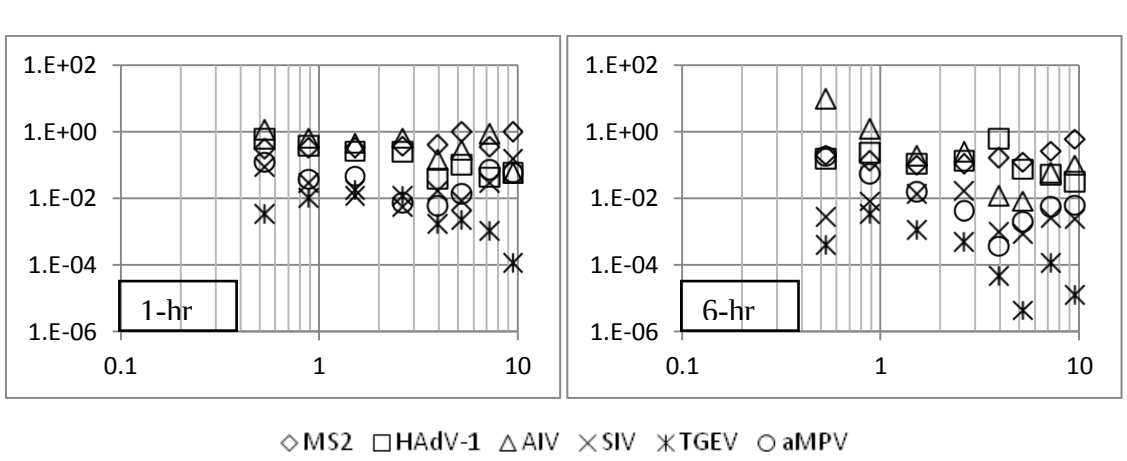

FIGURE 4.4.10 Survival (dimensionless, vertical axes) versus particle aerodynamic diameter [μm] (horizontal axes) for all six viruses for one-hour and six-hour tests.

TABLE 4.4.10 Pooled relative standard deviation for each data series shown in FIGURE 4.4.10.

Virus	MS2	HAdV-1	AIV	SIV	TGEV	aMPV
1-hr	+122.3% -55.0%	+490.4% -83.1%	+526.0% -84.0%	+1085.2% -91.6%	+1482.7% -93.7%	+671.0% -87.0%
6-hr	+320.1% -76.2%	+200.1% -66.7%	+371.7% -78.8%	+1233.2% -92.5%	+2395.0% -96.0%	+317.1% -76.0%

In order to evaluate virus inactivation in the impactor, six-hour to one-hour ratios were calculated for normalized live virus titer, normalized total virus concentration, normalized fluorescence intensity, relative recovery, and survival (FIGURE 4.4.12.). All ratios were calculated based on all viruses collected in the impactor. For normalized fluorescence intensity, the mean ratio for MS2 was 5.20 with a standard error of +0.61/-0.54. The ratio for the five animal viruses was 5.12 (+0.45/-0.41). For normalized total virus concentration, the ratio for MS2 was 6.08 (+1.73/-1.35), and for the five animal viruses was 4.11 (+0.72/-0.61). Ideally the ratios of normalized total virus concentration and normalized fluorescence intensity should be close to 6. However, as the actual ratios were generally close to 5, the aerosol collection rate of the Andersen impactor was decreasing during a test. The reason could be the decrease of the aerosol generation rate, the sampling efficiency, or both. The ratio of the normalized total virus concentration of the five animal viruses was lower than that for MS2 and that for normalized fluorescence intensity,

showing that the nebulizer output might have decreased faster for the five animal viruses. The decrease rate possibly depended on virus size.

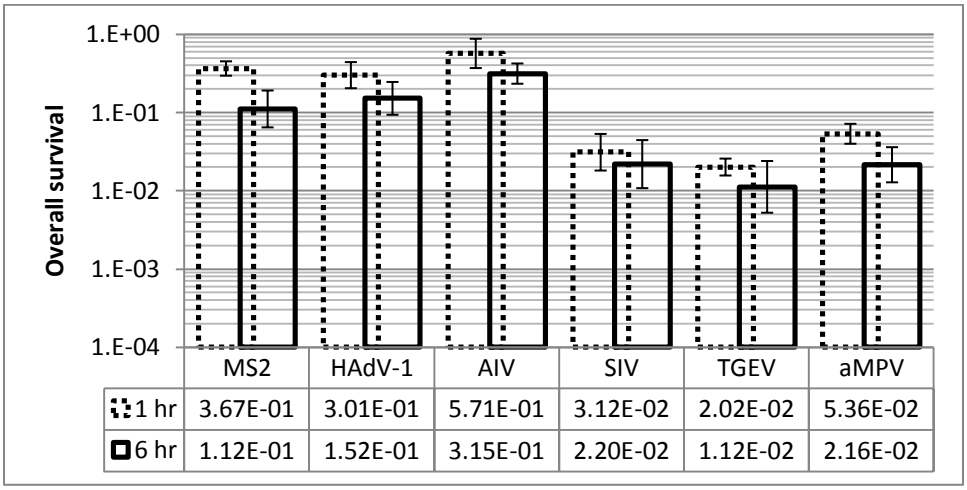

FIGURE 4.4.11 Overall survival (dimensionless) for all six viruses for one-hour and six-hour tests with error bars showing standard errors.

TABLE 4.4.11 P-values for survival with significant factors in bold.

Factor	Virus	Size	Duration	V:S	V:D	S:D	V:S:D
P-value	**<0.001**	**<0.001**	**0.014**	0.263	0.835	0.841	0.395

Given that inactivation of virus in the nebulizer fluid can be neglected, as will be proven in the next section, and if no significant inactivation occurs in the impactor, the live virus ratio should be comparable to the total virus ratio. On the other hand, if all virus collected was inactivated within one hour, the ratio could be slightly smaller than unity, considering the decrease in collection rate over time. In this study, the ratios of normalized live virus titer for the six viruses were lower than those of normalized total virus concentration and greater than unity, indicating virus inactivation in the impactor, but the collected viruses remained infectious longer than one hour. Inactivation can also be seen from the ratios of relative recovery and survival, which are very similar in value, and generally lower than one. For the six viruses, the relative recovery or survival for the six-hour tests are about 30%-60% of that for the one-hour tests. Due to large uncertainties, however, more tests are needed to determine which virus was inactivated faster or slower. The comparison of one-hour and six-hour results shows that due to significant virus inactivation in the dry impactor, when detecting viruses with the Andersen impactor, PCR could

benefit from longer sampling duration, but live virus titration may not. As a result of this investigation, one-hour tests were conducted for the rest of this study.

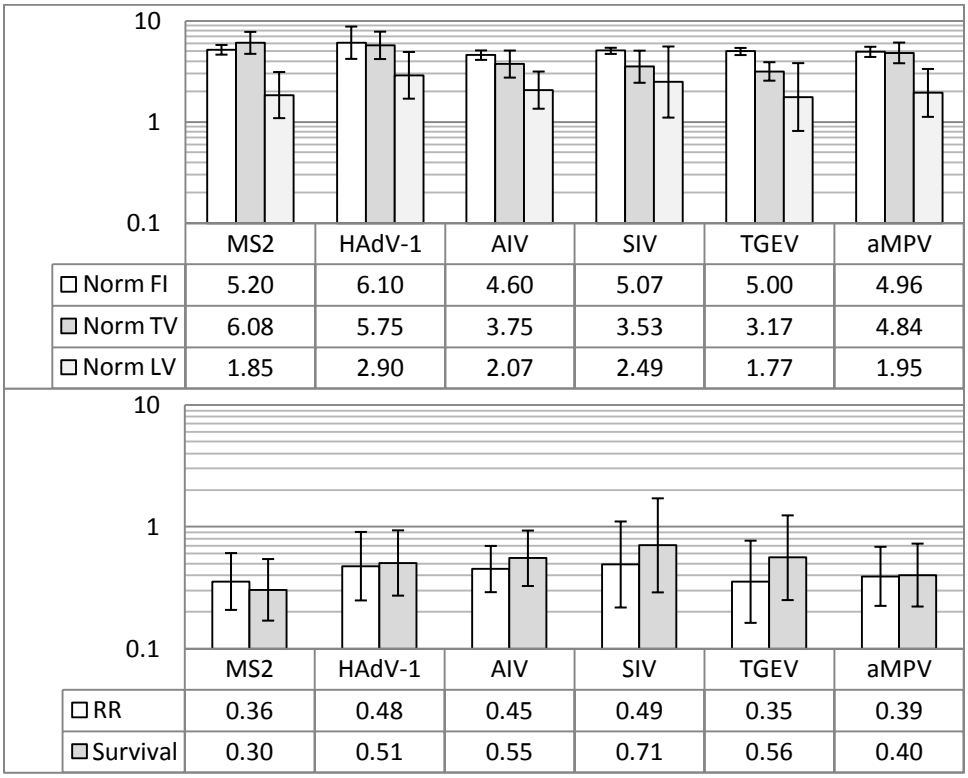

FIGURE 4.4.12 Ratios (dimensionless) of six-hour results over one-hour results for overall normalized fluorescence intensity (Norm FI), normalized total virus (Norm TV) concentration, normalized live virus (Norm LV) titer, relative recovery (RR), and survival for each virus with error bars showing standard errors.

Virus inactivation rate in the impactor could not be estimated with surface tests, since the virus on a collection plate is subjected to continuous impaction, and is covered and shielded by newly collected material. However, the inactivation curve could be solved by conducting tests with different sampling durations. For the same virus with the same test conditions and procedure, but different sampling durations, the inactivation rates in the airborne state and during the elution process could be considered a constant. For the other processes including transportation and storage, relative recovery or survival should not be affected as the same inactivation rate should apply to both impactor and nebulizer samples. As a result, differences in relative recovery and survival would be solely due to the virus inactivation in the impactor for different sampling durations. Large propagated uncertainties as shown in FIGURE 4.4.12, however, could be a

major problem when utilizing this method. Therefore, more repeats and improved virus analysis techniques especially for live virus titration are desirable.

4.4.2 Inactivation of virus in the nebulizer

Evaporation during nebulization gradually concentrates the nebulizer fluid. The effect can be calculated by dividing the "post" concentration with the "pre". The ratio of fluorescein for the one-hour tests was 1.11 with a standard error of 0.04. For the six-hour tests, the ratio was 1.21+/-0.06. The ratio did not significantly depend on the virus type (p=0.481) or test duration (p=0.105) by ANOVA, but based on the mean value, the evaporation effect seemed to be more obvious in the six-hour tests.

In order to check virus inactivation in the nebulizer, γ was calculated using live virus (LV) titer and fluorescence intensity (FI) as defined in Appert 2012:

$$\gamma = \frac{(\frac{LV}{FI})_{post}}{(\frac{LV}{FI})_{pre}} = \frac{(\frac{post}{pre})_{LV}}{(\frac{post}{pre})_{FI}}. \quad (4.4.3)$$

If inactivation was significant during nebulization, γ should be smaller than unity. From ANOVA, γ did not significantly depend on the virus type (p=0.887) or test duration (p=0.663). Its average was 1.12 with a 95% confidence interval from 0.89 to 1.40, which means the virus inactivation during the nebulization process was not significant up to six hours of nebulization with 10 psi (69 kPa) compressed air.

TABLE 4.4.12 Concentration ratios and γ calculated based on total virus instead of fluorescein.

Evaporation			
1-hour post/pre (standard error)	6-hour post/pre (standard error)	Virus p-value	Time p-value
1.27 (+0.12/-0.11)	1.32 (+0.13/-0.12)	0.320	0.490
Inactivation			
γ [95% confidence interval]		Virus p-value	Time p-value
0.98 [0.80, 1.20]		0.847	0.634

The same process of evaluating evaporation and virus inactivation in the nebulizer was performed using total virus instead of fluorescein, and the same conclusion was reached (TABLE 4.4.12). The concentration ratios based on total virus were greater than those based on fluorescein,

suggesting that the nebulization of fluorescein was faster. This should be one of the reasons causing the different physical losses between total virus and fluorescein. In the next tests for temperature, humidity, and UVGI effects, 10 psi (69 kPa) compressed air was used with one-hour of nebulization, thus the virus inactivation during the nebulization process could still be neglected.

4.5 Conclusions

MS2, HAdV-1, AIV, SIV, aMPV, and TGEV were size-selectively sampled with the ACI for one and six hours. The ACI collected detectable virus on most stages at the current test settings for one-hour sampling. Six hour samples did not show much higher live virus titers than one-hour samples, suggesting that inactivation of virus in the impactor was significant. For field tests using dry impactor plates, longer sampling durations may not lead to better live virus detection, thus PCR for total virus detection is recommended.

In the impactor samples, more than 95% of the collected aerosol by mass was smaller than 4.7 μm, and about 40% was collected on impactor stage 5 (1.1-2.1 μm). Thus most particles collected were in the region of small droplet nuclei, which can be inhaled and retained in the lower tract of the human respiratory system. The size distribution slightly depended on suspension medium. In the six-hour tests, the impactor collection efficiency may have decreased due to overloading especially for impactor stage 5. This could be seen from the change in size distribution of fluorescence intensity, and should be noted for long-term sampling.

For MS2, the physical loss measured using fluorescein was similar to that measured using total virus. For the other five viruses, however, physical loss measured using total virus was greater. Therefore, the actual physical loss of virus may not be accurately represented by fluorescein, and the discrepancy may depend on virus size, since MS2 is much smaller than the five animal viruses. Virus type was not significant for particle size distribution based on the five animal viruses.

In Appert 2012, MS2, HAdV-1, and TGEV had higher relative recovery than AIV and SIV. In this study, the relative recovery of AIV was similar to that of MS2 or HAdV-1, and higher than

that of SIV, TGEV, or aMPV, among which TGEV had the lowest relative recovery. The reason for this difference is not clear yet, given that virus sources, preparation, and analysis were the same for the two studies. The current results also show that MS2, HAdV-1, and AIV had higher survival and lower uncertainty than SIV, TGEV, and aMPV. Therefore, only MS2, HAdV-1, and AIV were further tested in this study.

For MS2, the relative recovery and survival were similar for aerosol sizes from 0.4 to 10 μm, but for the five animal viruses, a decrease in relative recovery and survival was observed as the particle size increased. The reason is possibly the lower concentration or higher uncertainty for the larger particle sizes for the five animal viruses.

Using 10 psi (69 kPa) compressed air for up to six hours did not significantly inactivate virus in the nebulizer suspension. Although not statistically conclusive, the evaporation effect appeared to be more significant for six-hour tests than one-hour tests. Viruses were concentrated faster than fluorescein in the nebulizer fluid, suggesting the nebulization of fluorescein was faster. This should be one of the reasons leading to the different physical losses measured using total virus and using fluorescein.

For future work, more repeats and test durations are recommended to reduce uncertainties, and to determine the inactivation rate as a function of time for the collected viruses in the impactor. Improvement in the method of live virus titration is desirable as it was the main contributor to the uncertainties of relative recovery and survival.

5 Viral aerosol tests at different temperatures and humidities

5.1 Background

For viral aerosols, higher temperature generally results in lower survival (Harper 1961; Mbithi 1991; Farnsworth 2006; Zuk 2009; McDevitt 2010; Memarzadeh 2012), but the vulnerability to high temperature can be different for different viruses. For adenovirus, a previous study found that its survival was stable between 4 and 36 ˚C, and was significantly lower at higher temperatures (Ginsberg 1956). A more recent study showed that its infectivity dropped dramatically at temperatures above 29 ˚C (Li 2008). Relative humidity (RH) is another significant factor that affects viral aerosol survival and transmission. RH affects the amount of water in the aerosol. Some studies reported that RH had an effect on the aerosol size distribution (Lowen 2007; Verreault 2008), but others did not find significant changes for the RH range from 30% to 80% (Ijaz 1987; Peccia 2001a). For viral aerosol survival, unlike temperature, the RH effect is more complex, and depends on virus type (Akers 1969, 1973; Benbough 1971; de Jong 1973; Farnsworth 2006; Verreault 2008). Generally, lipid viruses (influenza viruses, aMPV, and TGEV) have higher survival at lower RH (< 30%), and non-lipid viruses (adenovirus) are more stable at higher RH (> 70%) (Benbough 1971; de Jong 1973; Mohr 1991; Cox 1995; Assar 2000; Farnsworth 2006; Tang 2009; McDevitt 2010). This generalization is based on a number of observed cases, but exceptions exist (Mbithi 1991). As viral aerosol inactivation depends on humidity and virus lipid coating, it has been proposed that the inactivation might be due to stress at the air-water interface, but not the toxicity of concentrated salt solution in the aerosol droplet (Dubovi 1970; Trouwborst1973; Sattar 1987; Casanova 2010). The virus survival response to RH also depends on suspension ingredients, especially the content of salts, proteins, and polyhydroxy (Harper 1963; Webb 1963; Akers 1969, 1973; Rechsteiner 1969; Dubovi 1970; Benbough 1969, 1971; de Jong 1973; Trouwborst 1973; Schaffer 1976; Cox 1995; Appert 2012; Yang 2012).

In previous studies, MS2 aerosol generally had highest survival at RH lower than 30%, lowest survivability near 60% RH, and increasing survivability at RH greater than 60% (Dubovi 1970; Trouwborst1973; Woo 2010). For some suspensions, such as tryptone, the recoveries at all RH levels were similar (Dubovi 1970). MS2 in TSB, which was the same as the current study, was found to have the highest relative recovery at 50% compared with results at 15% and 85% (Appert 2012). Adenovirus was reported to be more stable at high RH than low RH, and was most stable at RH above 80% (Harper 1961; Miller 1967; Davis 1971; Appert 2012). HAdV-1 in MEM had the lowest relative recovery at 50% RH compared with 15% and 85% RH (Appert 2012). Influenza A virus was reported to survive better at RH lower than 40%, and have higher inactivation at higher RH (Loosli 1943; Hemmes 1960; Harper 1961; Buckland 1962; de Jong 1964, 1973; Tellier 2006; Zuk 2009; McDevitt 2010). Some other studies showed that influenza A virus had the lowest recovery at about 50% RH, the highest recovery at low RH, and moderate recovery at high RH (Shechmeister 1950; Hood 1963; Schaffer 1976; Yang 2012). In Appert 2012, the relative recovery of AIV in MEM was lowest at 50% RH, highest at 85%, and moderate at 15%. It was also reported that both extremely low and high RH could reduce the survival of influenza A virus (Memarzadeh 2012). One reason for the different findings might be the different virus suspensions.

Interaction between temperature and RH has been discussed for viral aerosol survival and transmission (Tang 2009; Zuk 2009). Some studies suggested that absolute humidity (AH) might be a better predictor than RH for the survival, transmission, and seasonality of influenza viruses, and using AH could eliminate the interaction term between temperature and humidity. Generally, as AH increases at a constant temperature, the survival or transmission of influenza virus was found to decrease exponentially (Shaman 2009, 2010; McDevitt 2010; Memarzadeh 2012). However, one study on the seasonality of influenza A virus reached the opposite conclusion that temperature and RH were significant factors, while AH was not (Tang 2010). Therefore, further tests on the effect of AH are still needed for influenza viruses as well as for other types of viruses.

5.2 Test method

Based on the capacity of the chamber AHU, MS2, HAdV-1, and AIV were tested at five thermal conditions chosen for at least two levels of temperature, RH, and AH (FIGURE 5.2.1 and TABLE 5.2.1). For each condition, the temperature variation was kept below 1 ℃, and RH variation below 5%. The chamber was always operated isothermally, which means the heat exchangers in the chamber walls and in the AHU were run at the same temperature. This was to keep the flow fields, particle trajectories, and residence times for different test conditions comparable.

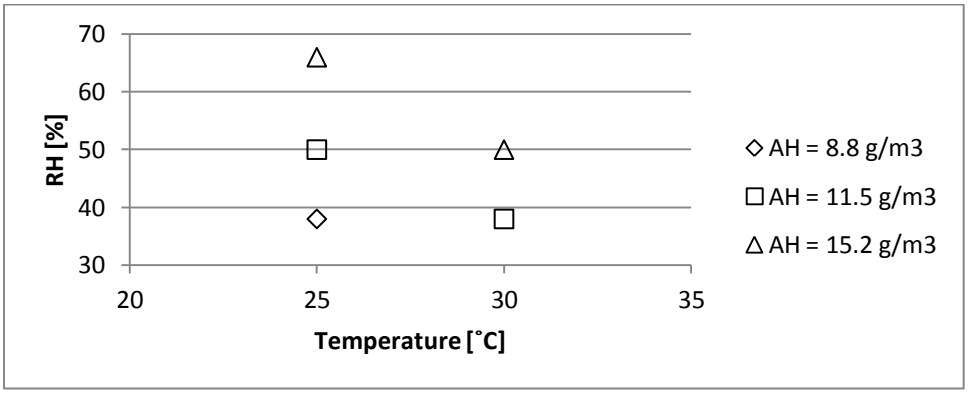

FIGURE 5.2.1 Five thermal and moisture conditions tested for MS2, HAdV-1, and AIV aerosols.

TABLE 5.2.1 Five thermal conditions tested for MS2, HAdV-1, and AIV aerosols.

Condition	I	II	III	IV	V
Temperature [˚C]	25	25	25	30	30
RH [%]	38	50	66	38	50
AH [g/m^3]	8.8	11.5	15.2	11.5	15.2

AH is the actual water vapor content in the air, or the mass of vapor content (m_v [g]) per volume of air (V_a [m^3]):

$$AH = \frac{m_v}{V_a}. \tag{5.2.1}$$

To calculate AH, saturated vapor pressure (p_s [Pa]) needs to be calculated first from absolute temperature (T [K]) (Hyland 1983):

$$p_s = exp\left(\sum_{i=0}^{5}\left(c_i T^{i-1}\right) + c_6 lnT\right). \tag{5.2.2}$$

TABLE 5.2.2 Values of the coefficients in EQUATION 5.2.2 for saturated vapor pressure.

C_0	C_1	C_2	C_3	C_4	C_5	C_6
-5.80022e3	1.39150	-4.86402e-2	4.17648e-5	-1.44521e-8	0	6.54597

EQUATION 5.2.2 is valid for the temperature range between 0 and 200 ˚C, which fully covers that of the chamber tests. Then, vapor pressure (p_v [Pa]) can be determined using the definition of RH for an ideal gas:

$$p_v = RH \times p_s. \tag{5.2.3}$$

Finally, AH in kg/m^3 can be calculated using the ideal gas law, given that the molar mass of water vapor (M_v) is 18.015e-3 kg/mol, and the universal gas constant (R) is 8.314 J/(mol K):

$$AH = \frac{m_v}{V_a} = \frac{p_v M_v}{RT}. \tag{5.2.4}$$

In this study, AH is given in g/m^3 as normally found in the literature. In some publications, AH could be expressed as specific humidity (SH) or humidity ratio which is the vapor mass per unit dry air mass [kg/kg], or as vapor pressure (VP) [mbar]. The values in different units for the tested humidity levels are listed in TABLE 5.2.3.

TABLE 5.2.3 AH levels tested in the current study expressed in various common units.

AH [g/m^3]	8.8	11.5	15.2
SH [kg/kg]	0.008	0.010	0.013
VP [mbar]	12.1	15.7	20.7

The test setup, including aerosol injection, sampling, and chamber ventilation rate was the same as the previous one-hour tests. The tests were conducted in triplicate with randomized order for each virus. ANOVA was carried out on a logarithmic scale for impactor stages 3-7 (0.4-4.7 μm) to test the significance of temperature, RH, AH, and their interactions for responses including relative recovery and survival.

5.3 Results and discussion

Normalized live virus titer versus particle aerodynamic diameter was plotted for each virus and test condition in FIGURE 5.3.1. One uncertainty was obtained for each virus by assuming it did not significantly depend on particle size, temperature, or humidity (TABLE 5.3.1). The overall normalized live virus titers are shown in FIGURE 5.3.2.

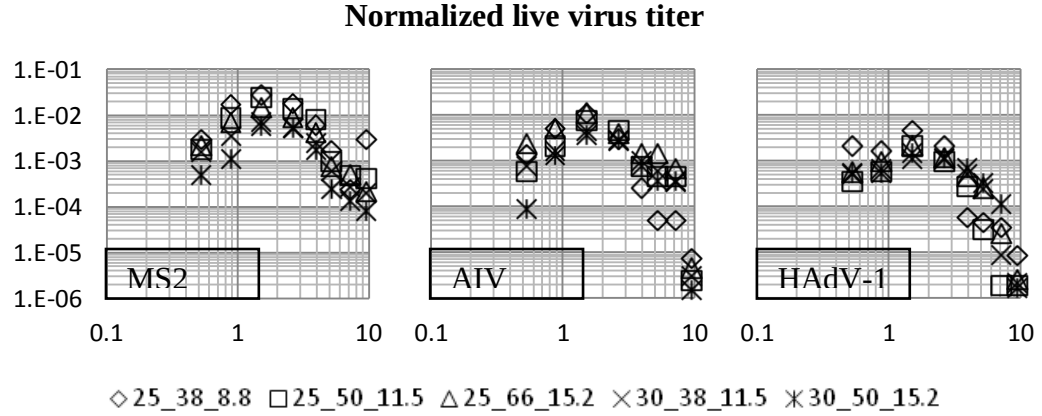

FIGURE 5.3.1 Normalized live virus titer (dimensionless, vertical axes) versus particle aerodynamic diameter [μm] (horizontal axes). Temperature [˚C], RH [%], and AH [g/m^3] are respectively used in the data series' names.

TABLE 5.3.1 Pooled relative standard deviation for each virus in FIGURE 5.3.1.

Virus	MS2	AIV	HAdV-1
Relative standard deviation	+167.7%/-62.6%	+271.9%/-73.1%	+135.7%/-57.6%

ANOVA was carried out with two models. One consisted of virus type, particle size, temperature, and RH. The other used AH instead of RH. The p-values of the two models are listed in TABLE 5.3.2. Virus was a significant factor; in FIGURE 5.3.2, MS2 had lowest total loss, and HAdV-1 had the highest. Particle size was significant as expected. Temperature was significant; all three viruses seemed to have greater total losses at the higher temperature, but the difference was not as obvious for HAdV-1 as for MS2 and AIV, which was reflected in the significant interaction between virus and temperature. Neither RH nor AH was significant.

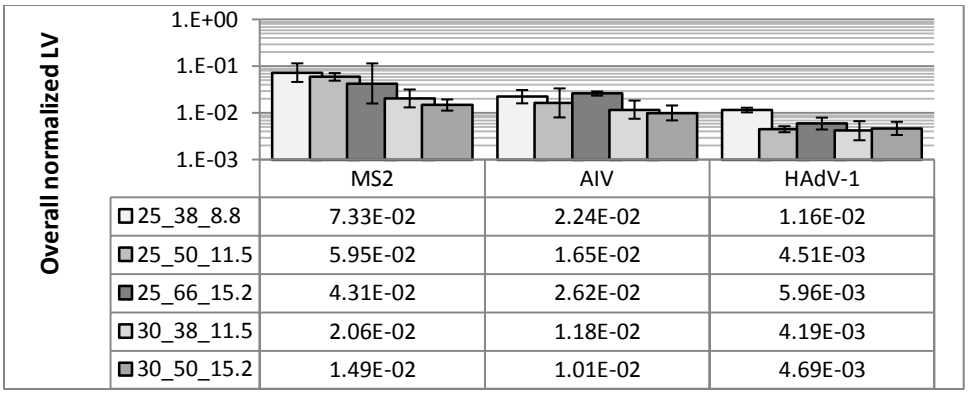

	MS2	AIV	HAdV-1
25_38_8.8	7.33E-02	2.24E-02	1.16E-02
25_50_11.5	5.95E-02	1.65E-02	4.51E-03
25_66_15.2	4.31E-02	2.62E-02	5.96E-03
30_38_11.5	2.06E-02	1.18E-02	4.19E-03
30_50_15.2	1.49E-02	1.01E-02	4.69E-03

FIGURE 5.3.2 Overall normalized live virus (LV) titer (dimensionless) with error bars showing standard errors. Temperature [˚C], RH [%], and AH [g/m^3] are respectively used in the data series' names.

TABLE 5.3.2 P-values for normalized live virus titer with significant factors in bold.

Factor	Virus	Size	Temp	RH	V:S	V:T	S:T	V:R	S:R	T:R
P	**<0.001**	**<0.001**	**<0.001**	0.117	0.108	**0.018**	0.077	0.297	0.099	0.877
Factor	Virus	Size	Temp	AH	V:S	V:T	S:T	V:A	S:A	T:A
P	**<0.001**	**<0.001**	**<0.001**	0.528	0.108	**0.020**	0.077	0.252	0.177	0.074

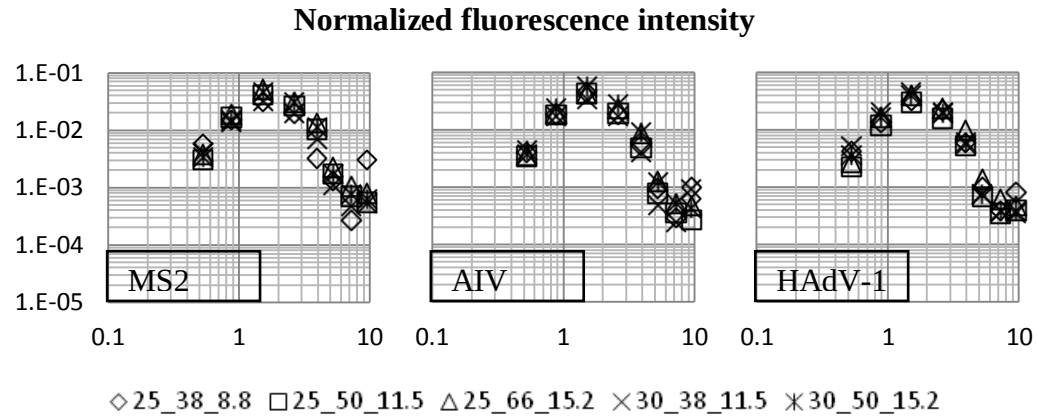

FIGURE 5.3.3 Normalized fluorescence intensity (dimensionless, vertical axes) versus particle aerodynamic diameter [μm] (horizontal axes). Temperature [˚C], RH [%], and AH [g/m^3] are respectively used in the data series' names.

Physical loss versus particle size measured with fluorescein for each virus and condition is shown in FIGURE 5.3.3. By assuming that the uncertainty did not significantly depend on virus type, particle size, and thermal condition, one pooled relative standard deviation was calculated for all

the data points in FIGURE 5.3.3, and the result was +33.2%/-24.9%. The overall normalized fluorescence intensities for each virus are shown in FIGURE 5.3.4. The p-values are listed in TABLE 5.3.3.

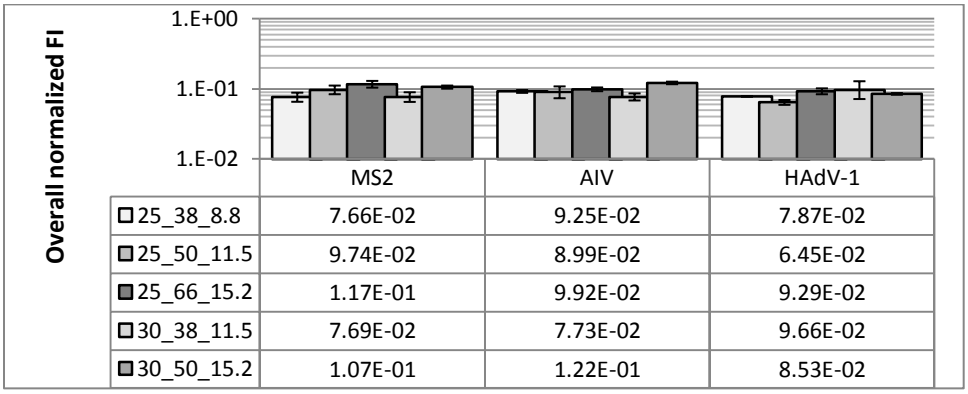

	MS2	AIV	HAdV-1
25_38_8.8	7.66E-02	9.25E-02	7.87E-02
25_50_11.5	9.74E-02	8.99E-02	6.45E-02
25_66_15.2	1.17E-01	9.92E-02	9.29E-02
30_38_11.5	7.69E-02	7.73E-02	9.66E-02
30_50_15.2	1.07E-01	1.22E-01	8.53E-02

FIGURE 5.3.4 Overall normalized fluorescence intensity (FI) (dimensionless) with error bars showing standard errors. Temperature [˚C], RH [%], and AH [g/m^3] are respectively used in the data series' names.

TABLE 5.3.3 P-values for normalized fluorescence intensity with significant factors in bold.

Factor	Virus	Size	Temp	RH	V:S	V:T	S:T	V:R	S:R	T:R
P	**0.015**	**<0.001**	0.166	**<0.001**	0.068	0.166	0.753	**<0.001**	**<0.001**	**0.013**
Factor	Virus	Size	Temp	AH	V:S	V:T	S:T	V:A	S:A	T:A
P	**0.015**	**<0.001**	0.166	**<0.001**	0.068	0.171	0.753	**0.009**	**<0.001**	0.403

As shown in FIGURES 5.3.3 and 5.3.4, normalized fluorescence intensity did not change much from virus to virus, or between different thermal conditions. In ANOVA, however, virus type was significant. By comparing the three viruses, it was found that MS2 was significantly different than HAdV-1 (p=0.010), while AIV was not (p=0.707). This result is similar to that in the previous tests for different sampling durations, and the reason could be the different types of suspension media. Interaction between particle size and virus had a p-value of 0.068, close to the critical value, also showing the likely effect of the suspension medium. Both RH and AH were significant, as well as their interactions with particle size, suggesting that humidity affected both overall aerosol size and size distribution. Interactions between virus and both humidities were significant, indicating that different suspensions may have different responses to the change of humidity. Temperature was not significant, suggesting that the flow field was relatively stable, and a similar amount of aerosol was collected for different temperatures. This was desirable, as

comparison between different thermal conditions required similar aerosol residence times and trajectories. Interaction between temperature and RH was significant, while that between temperature and AH was not, meaning that to predict aerosol physical loss, using AH may eliminate the interaction term between temperature and humidity.

Normalized total virus concentration versus particle size for each virus and condition is plotted in FIGURE 5.3.5 with the pooled relative standard deviation for each virus listed in TABLE 5.3.4. The overall normalized total virus concentrations are plotted in FIGURE 5.3.6. The p-values are listed in TABLE 5.3.5.

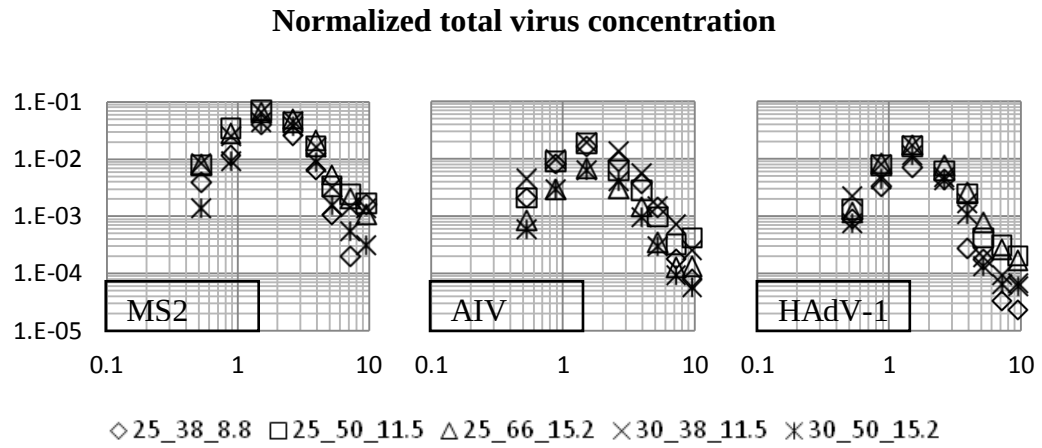

FIGURE 5.3.5 Normalized total virus concentration (dimensionless, vertical axes) versus particle aerodynamic diameter [μm] (horizontal axes). Temperature [˚C], RH [%], and AH [g/m^3] are respectively used in the data series' names.

TABLE 5.3.4 Pooled relative standard deviation for each virus in FIGURE 5.3.5.

Virus	MS2	AIV	HAdV-1
Relative standard deviation	+119.4%/-54.4%	+99.5%/-49.9%	+115.5 %/-53.6%

In the ANOVA results, the virus type was a significant factor. From FIGURES 5.3.6 and 5.3.4, the physical losses of AIV and HAdV-1 calculated using total virus were higher than those calculated using fluorescein. For MS2, both physical losses were similar. This result is similar to that of the previous tests for different sampling durations, and suggests that using fluorescein to calculate the physical loss of virus would be valid only for small viruses such as MS2.

Temperature and RH were not significant for normalized total virus, but AH was significant. Interactions between virus and RH, and between virus and AH were both significant, showing the possibility of different hygroscopic properties for different suspension media or viruses. Interaction between particle size and RH, and that between particle size and AH were not significant, meaning the humidity effect on particle size distribution was not significant. This was different from the fluorescein result, probably due to larger uncertainty in the PCR measurements. Interaction between temperature and RH was significant, but neither temperature nor RH was significant by itself. Interaction between temperature and AH was significant, which was different from the fluorescein result. This was probably due to larger uncertainty associated with the PCR measurements as well. Further tests are recommended.

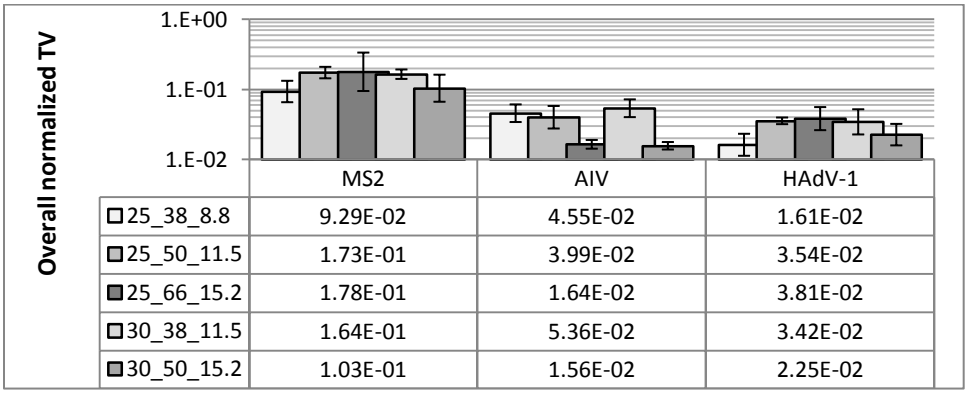

	MS2	AIV	HAdV-1
25_38_8.8	9.29E-02	4.55E-02	1.61E-02
25_50_11.5	1.73E-01	3.99E-02	3.54E-02
25_66_15.2	1.78E-01	1.64E-02	3.81E-02
30_38_11.5	1.64E-01	5.36E-02	3.42E-02
30_50_15.2	1.03E-01	1.56E-02	2.25E-02

FIGURE 5.3.6 Overall normalized total virus (TV) concentration (dimensionless) with error bars showing standard errors. Temperature [˚C], RH [%], and AH [g/m^3] are respectively used in the data series' names.

TABLE 5.3.5 P-values for normalized total virus concentration with significant factors in bold.

Factor	Virus	Size	Temp	RH	V:S	V:T	S:T	V:R	S:R	T:R
P	**<0.001**	**<0.001**	0.488	0.214	0.079	0.636	0.980	**<0.001**	0.614	**<0.001**
Factor	Virus	Size	Temp	AH	V:S	V:T	S:T	V:A	S:A	T:A
P	**<0.001**	**<0.001**	0.488	**<0.001**	0.079	0.654	0.980	**<0.001**	0.392	**0.004**

Based on normalized live virus titer and normalized fluorescence intensity, size distribution of relative recovery was calculated for each virus and condition, and is shown in FIGURE 5.3.7 with uncertainties listed in TABLE 5.3.6. Overall relative recovery for each virus is plotted in FIGURE 5.3.8. Since virus type was significant ($p<0.001$) as expected, and different viruses

reacted differently to changes of thermal condition, ANOVA was carried out for each virus individually (TABLE 5.3.7).

Overall, MS2 had the highest relative recovery, and HAdV-1 had the lowest. For MS2, particle size was not significant, meaning relative recovery was constant for all impactor stages. Temperature was significant, and MS2 had a higher relative recovery at the lower temperature. RH and AH were both significant. MS2 had a higher relative recovery at lower RH or AH, which was different than the previous study using the same suspension medium (Appert 2012), where MS2 had the highest relative recovery in the mid-range of RH. The difference could be likely due to the smaller range of RH tested in this study than in Appert 2012. None of the interactions were significant for MS2.

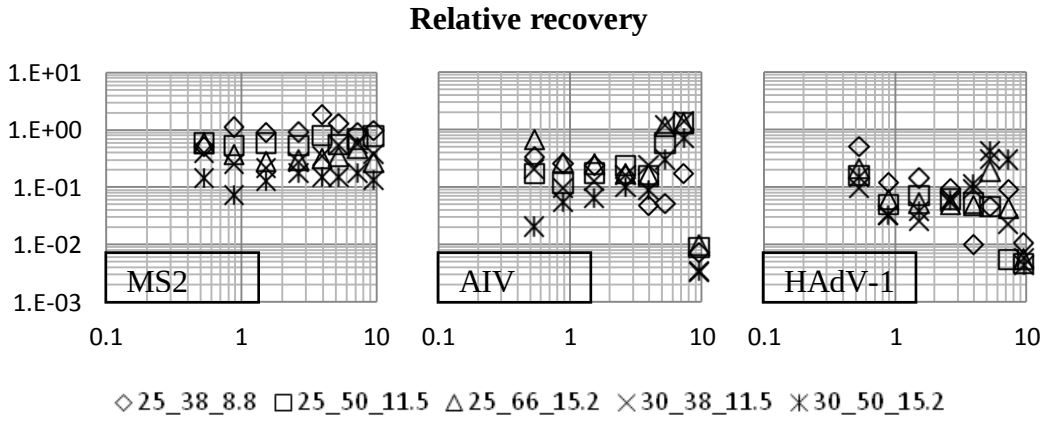

FIGURE 5.3.7 Relative recovery (dimensionless, vertical axes) versus particle aerodynamic diameter [µm] (horizontal axes). Temperature [˚C], RH [%], and AH [g/m^3] are respectively used in the data series' names.

TABLE 5.3.6 Pooled relative standard deviation for each virus in FIGURE 5.3.7.

Virus	MS2	AIV	HAdV-1
Relative standard deviation	+160.9%/-61.7%	+311.0%/-75.7%	+167.0%/-62.5%

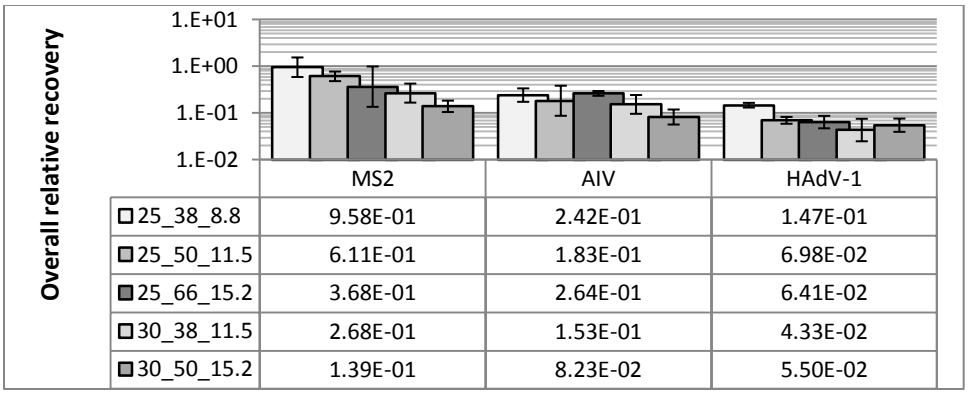

	MS2	AIV	HAdV-1
25_38_8.8	9.58E-01	2.42E-01	1.47E-01
25_50_11.5	6.11E-01	1.83E-01	6.98E-02
25_66_15.2	3.68E-01	2.64E-01	6.41E-02
30_38_11.5	2.68E-01	1.53E-01	4.33E-02
30_50_15.2	1.39E-01	8.23E-02	5.50E-02

FIGURE 5.3.8 Overall relative recovery (dimensionless) with error bars showing propagated standard errors. Temperature [˚C], RH [%], and AH [g/m^3] are respectively used in the data series' names.

TABLE 5.3.7 P-values for relative recovery for individual virus with significant factors in bold.

Factor	Size	Temp	RH	S:T	S:R	T:R	S:T:R
MS2	0.838	**<0.001**	**0.003**	0.897	0.916	0.502	0.930
AIV	0.958	**0.034**	0.228	0.428	0.920	0.191	0.843
HAdV-1	**0.001**	0.223	0.800	**0.027**	0.580	0.318	0.375
Factor	Size	Temp	AH	S:T	S:A	T:A	S:T:A
MS2	0.838	**<0.001**	**0.003**	0.897	0.936	0.540	0.884
AIV	0.958	**0.034**	0.693	0.428	0.981	**0.049**	0.631
HAdV-1	**0.001**	0.223	0.549	**0.027**	0.250	0.620	0.986

For AIV, particle size was not a significant factor, showing similar relative recovery for all impactor stages. Temperature was significant; AIV had higher relative recovery at the lower temperature. Neither RH nor AH was significant, but from FIGURE 5.3.8, AIV had the lowest relative recovery at 50% RH by mean value. This trend agrees with Appert 2012 using the same suspension medium. None of the interactions were significant except for that between temperature and AH, but the p-value was 0.049, just on the threshold of significance.

HAdV-1 behaved quite differently than the other two viruses. Particle size was significant. FIGURE 5.3.7 shows that relative recovery decreased as particle size increased, similar to the results in the previous tests for different sampling durations. Temperature was not significant. From FIGURE 5.3.8, relative recovery was quite similar except for the 25 ˚C 38% RH condition. RH and AH were not significant. Still from FIGURE 5.3.8, HAdV-1 might have the lowest

inactivation rate at low AH, but this needs to be proven with further tests. The current tests did not show the possible increase of relative recovery at high RH (> 80%) as discussed in other studies (Harper 1961; Miller 1967; Davis 1971; Appert 2012). The test facility needs to be improved in order to test more extreme conditions. None of the interactions were significant, except for that between temperature and particle size, meaning that temperature significantly affected the size distribution of relative recovery. This, however, could be due to test uncertainties.

Similar to relative recovery, survival was calculated from normalized live virus titer and normalized total virus concentration. The size distributions are shown in FIGURE 5.3.9 with pooled relative standard deviations listed in TABLE 5.3.8. The overall survival is plotted in FIGURE 5.3.10. P-values for each virus are shown in TABLE 5.3.9.

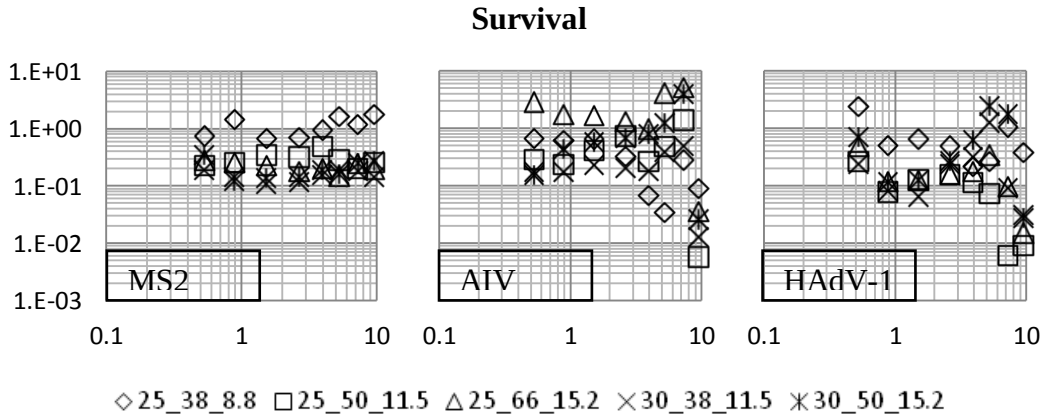

FIGURE 5.3.9 Survival (dimensionless, vertical axes) versus particle aerodynamic diameter (horizontal axes). Temperature [˚C], RH [%], and AH [g/m^3] are respectively used in the data series' names.

TABLE 5.3.8 Pooled relative standard deviation for each virus in FIGURE 5.3.9.

Virus	MS2	AIV	HAdV-1
Relative standard deviation	+176.4%/-63.8%	+398.6%/-79.9%	+250.2%/-71.4%

For MS2, particle size was not significant. Temperature was significant, and MS2 had higher survival at the lower temperature. RH and AH were both significant, and from FIGURE 5.3.10 MS2 had the highest survival at 8.8 g/m^3 AH. The trend agrees with the Dubovi 1970 buffered

saline solution result, Trouwborst 1973 NaCl solution result, and Woo 2010 result. None of the interactions were significant, except for that between temperature and RH, implying that modeling with AH would decouple the effects of humidity and temperature.

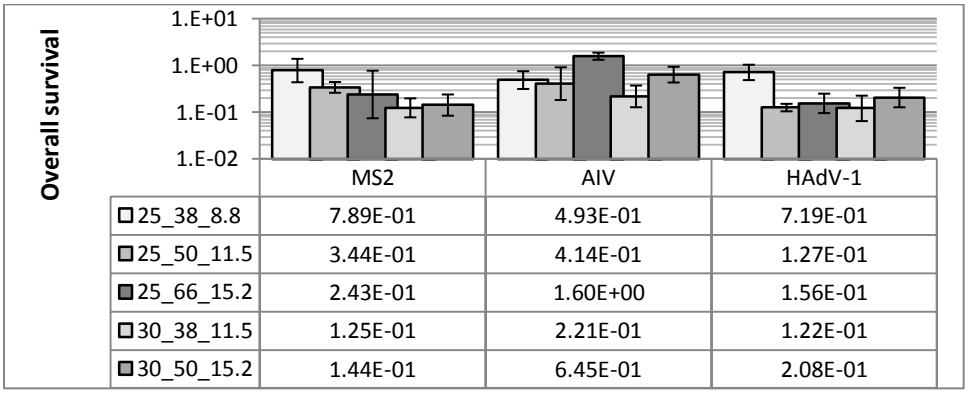

	MS2	AIV	HAdV-1
25_38_8.8	7.89E-01	4.93E-01	7.19E-01
25_50_11.5	3.44E-01	4.14E-01	1.27E-01
25_66_15.2	2.43E-01	1.60E+00	1.56E-01
30_38_11.5	1.25E-01	2.21E-01	1.22E-01
30_50_15.2	1.44E-01	6.45E-01	2.08E-01

FIGURE 5.3.10 Overall survival (dimensionless) with error bars showing propagated standard errors. Temperature [˚C], RH [%], and AH [g/m^3] are respectively used in the data series' names.

TABLE 5.3.9 P-values for survival for individual virus with significant factors in bold.

Factor	Size	Temp	RH	S:T	S:R	T:R	S:T:R
MS2	0.885	**<0.001**	**0.015**	0.799	0.985	**0.023**	0.970
AIV	0.846	0.075	**0.011**	0.590	0.903	0.276	0.963
HAdV-1	**0.022**	0.666	0.178	0.304	0.993	**0.002**	0.858
Factor	Size	Temp	AH	S:T	S:A	T:A	S:T:A
MS2	0.885	**<0.001**	**0.003**	0.799	0.988	0.278	0.957
AIV	0.846	0.075	**0.008**	0.590	0.967	0.449	0.794
HAdV-1	**0.022**	0.666	**0.002**	0.304	0.956	0.619	0.996

For AIV, particle size was not significant. Temperature was not significant, but from FIGURE 5.3.10 AIV had lower survival at higher temperature for the same AH by mean value. RH and AH were significant. From FIGURE 5.3.10, the AH effect is more obvious than RH as suggested in other studies. However, a significant difference with past studies is that the survival of AIV was higher at 15.2 g/m^3 than at 11.5 g/m^3, but did not monotonically decrease as AH increased (Loosli 1943; Hemmes 1960; Harper 1961; Buckland 1962; de Jong 1964, 1973; Tellier 2006; Zuk 2009; McDevitt 2010). The reason could be the different suspension ingredients used in the current tests with the natural suspension or those used in the above studies. For the RH effect, survival at 50%

was not lower than that at 38%. How survival would change at even lower RH could not be seen from the current test results. Survival at 66% was much higher than that at the two lower levels, agreeing with some studies (Shechmeister 1950; Hood 1963; Schaffer 1976; Appert 2012; Yang 2012). None of the interactions for AIV was significant.

For HAdV-1, particle size was a significant factor as for the relative recovery results and as in the previous tests for different sampling durations. From FIGURE 5.3.9, survival decreased for larger particles. Temperature was not significant. From FIGURE 5.3.10, the overall survival at 30 ˚C was not lower than that at 25 ˚C. RH was not significant, but the interaction between temperature and RH was significant. AH was significant. HAdV-1 had the highest survival at 8.8 g/m^3, the lowest at 11.5 g/m^3, and the medium at 15.2 g/m^3. None of the other interactions were significant. ANOVA results show that when modeling HAdV-1 survival with AH, the interaction term between temperature and humidity disappeared. This agrees with the MS2 result and the published studies on AIV.

5.4 Conclusions

The test results show that with current test setup and sampling method, the relative recovery and survival of the viral aerosol collected by the Andersen impactor depended on temperature and humidity. Based on the fluorescein measurement, the viral aerosol size distribution was also affected by humidity. Generally, viruses survived better at 25 ˚C than at 30 ˚C, however, the difference was not significant for HAdV-1, suggesting that HAdV-1 is less vulnerable than MS2 and AIV to the moderately high temperatures. Based on the survival results, AH had lower p-values than RH for the three viruses, showing that AH could be a better predictor than RH for virus survival. Using AH also decoupled the effects of humidity and temperature for MS2 and HAdV-1. This result agrees with past studies on AIV, and suggests that the conclusion could be extended to other viruses. It is thus suggested that AH should be documented in future viral aerosol tests. For the three test viruses, MS2 had higher survival at 8.8 g/m^3 AH than 11.5 g/m^3 or 15.2 g/m^3, with the latter two had similar survival. AIV had higher survival at 15.2 g/m^3 than 11.5 g/m^3 or 8.8 g/m^3, with the latter two had similar survival. HAdV-1 had the highest survival at 8.8 g/m^3, and the lowest at 11.5 g/m^3. Its survival at 15.2 g/m^3 was slightly higher than that at 11.5

g/m^3. The changes of relative recovery and survival of the three viruses due to the changes of temperature and humidity agree with some of the past studies. The main limitations, however, were the number of data points and the range of test conditions, even though it covered the most common indoor environments. Since the relationship could be non-linear, the complete response of virus inactivation especially that to humidity was still unknown. To fully explore the responses and compare with the published data, the method used in this group of tests should be extended for broader test conditions in the future. For example, AIV aerosol transmission has been studied for the AH range covering 0-30 g/m^3, much greater than the range tested in this study (8.8-15.2 g/m^3). Additionally, more tests are suggested for other viruses and suspension media.

Relative recovery showed similar trends with survival for the three viruses, but ANOVA did not indicate significant interaction between temperature and RH, which was different from the survival result. The disagreement suggests that the physical loss of fluorescein was different from that of virus in this study, resulting in the different ANOVA conclusion using the two methods. One reason could be in the different nebulizer output rates for virus and fluorescein as discussed in Chapter 4.

As virus inactivation occurred both in the airborne state and on the impactor plates in these tests, the virus relative recovery and survival should not be used directly to compare viral aerosol inactivation rates, unless the trend of inactivation in the airborne state and in the impactor could be assumed to be the same for the same virus. This assumption, however, should be verified with further study. As the chamber conditions were selected to simulate real indoor environments, the results should predict field sampling situations within the tested temperature and humidity ranges using a similar aerosol sampler.

6 Experimental tests of viral aerosol inactivation by UVGI

6.1 Background

6.1.1 Introduction

Ultraviolet germicidal irradiation (UVGI) systems are designed to disinfect air, water, and surfaces. The germicidal range of UV wavelength is 200-320 nm that includes part of the UVC band (200-280 nm), all of the UVB band (280-320 nm), but none of the UVA band (320-400 nm) (CDC 1994; Kowalski 2009). Unlike inactivation due to desiccation or adverse humidity when inactivation most likely happens at the virus coating, UVGI reduces infection by photochemical reaction which damages the genetic material by producing dimers and other photo products, causing the microorganism to be incapable of replicating (Sattar 1987; Navy Environmental Health Center 1992; Rahn 1999; Chandrasekhar 2000; Miller 2000; Beggs 2002a; Noakes 2004b, 2006; Ko 2005; Kowalski 2009; Rudnick 2009). The UV absorption by nucleic acid peaks around 260 nm, at lower and higher (up to 320 nm) wavelengths the sensitivity decreases, but increases again below 230 nm (Luckiesh 1946; Summer 1962; NIOSH 1972; Jacobs 1992; Rahn 1999; Hijnen 2006; Kowalski 2009). In applications, low-pressure mercury lamps are often used to generate 253.7 nm UVC light to reduce disease transmission in indoor environments. This wavelength is very close to the absorption peak and ready to be absorbed by microorganisms (Rudnick 2009).

Generally, UVGI is effective in inactivating viruses and most bacteria, and its effectiveness depends on the type of microorganism (Miller 2000; Kowalski 2001; Noakes 2004a, 2004b, 2006; Memarzadeh 2010). Virus resistance to UVGI was reported to be lower than bacteria and fungi spores by some researchers (Jensen 1964; Brickner 2003; Tseng 2005b), but others reported that viruses were on average more resistant to UVGI than bacteria (Kowalski 2009). For viruses, the resistance to UVGI was observed to depend on the type of nucleic acid. Viruses with double-stranded genomes are less susceptible than those with single-stranded ones. This is possibly

because of the redundancy of genetic information which helps the double-stranded type have more chance to be repaired (Bishop 1967; Deshmukh 1969; Harm 1980; Becker 1989; Kallenbach 1989; Gerba 2002; Thurston-Enriquez 2003; Tseng 2005b; Kowalski 2009). Generally, adenoviruses are extremely resistant to UVGI compared to other enteric viruses, possibly due to its double-stranded DNA (Meng 1996; Gerba 2002; Thurston-Enriquez 2003; Nwachuku 2005; Hijnen 2006). Adenoviruses were found to be much more resistant to UVGI than influenza viruses and slightly more resistant than MS2 (Jensen 1964; Thurston-Enriquez 2003; Ko 2005; Nwachuku 2005; Tseng 2005b).

Virus susceptibility to UVGI does not depend on temperature (Rentschler 1941). Viral aerosol susceptibility to UVGI has been reported to be affected by RH, but the trend is not conclusive, and may be species dependent (Rentschler 1941; Wells 1942a; Riley 1971, 1976; Blatchley 2007; Kowalski 2009). Most recent studies mentioned that high RH (>60%) reduced the effectiveness of UVGI (Peccia 2001a, 2004; Beggs 2002b; Xu 2003; Tseng 2005b; Verreault 2008; Tang 2009; Memarzadeh 2010, 2012). This was possibly due to reduced susceptibility of microorganisms, as studies did not find a decrease in irradiance at high RH up to 95% (Miller 2000; Peccia 2001a). At extremely high RH, virus susceptibility to UVGI would approach that in water (Kowalski 2009).

Compared to chemical disinfection methods, although UVGI is harmful to human skin and eyes, it has several advantages. First, it has little toxic byproduct or emissions (Ko 2005). Second, it has no smell. Third, it does not require storage of hazardous materials. Fourth, it does not have an overdosing problem. However, a significant amount of work is still needed to make UVGI safer and more efficient for viral aerosol disinfection. Lack of data and standards for measurement and application of UVGI systems is the main obstacle preventing its widespread use. Therefore, more tests are needed to build the database on how well UVGI disinfects viral aerosols under various conditions.

Based on the damage level in nucleic acid, microorganisms inactivated by UVGI may partially recover. The repair process requires the presence of 320-410 nm wavelength, thus it is called photoreactivation (Liao 2010). Photoreactivation is usually available for bacteria or when cells are present for virus (Lennox 1954; Jagger 1965; Deshmukh 1969; Peccia 2001b; Beggs 2002a;

Masschelein 2002; Nuanualsuwan 2002; Thurston-Enriquez 2003; Xu 2003). Photoreactivation in bacteria was discovered and studied a long time ago (Prat 1936; Kelner 1949). Due to the randomness of the repair process, mutation could occur in the recovered microorganisms (Beggs 2002a). For viruses, photoreactivation is usually not applicable due to the lack of enzymes for repair out of a cell host (Bishop 1967; Deshmukh 1969; Samad 1987; Nuanualsuwan 2002, 2003). The photoreactivation effect was therefore neglected in this study.

6.1.2 History and applications

Studies of UV effects on microorganisms including viruses started in the late 1800s (Widmark 1889; Ward 1892; Henri 1914; Rivers 1928; Sturm 1932). Use of UVGI for disinfecting water, surfaces, and air for disease reduction also has a long history (Hollander 1942; Wells 1942a, 1955; Luckiesh 1946; Riley1957, 1976; Summer 1962; Jensen 1964; Collins 1971; David 1973; Goldner 1980; Kowalski 2009). Especially for water disinfection, the history has been more than a hundred years (Downes 1877; von Recklinghausen 1914). Since then, UVGI has been most widely used in water treatment and food process industries (Blatchley 1997; Xu 2003; Ko 2005; Hijnen 2006).

Use of UVGI for indoor air disinfection started in the 1930s (Hart 1937; Wells 1955). In 1942, the use of UVGI in schools greatly reduced the spread of measles, chickenpox, and mumps (Wells 1942b). In 1957, UVGI was demonstrated to be able to control the spread of tuberculosis (TB) (Riley 1957). Many other studies also showed the effectiveness of UVGI in infection control (McLean 1961; Kundsin 1984; Tseng 2005b). However a few studies that failed to show the effectiveness of UVGI have been cited as proof of its ineffectiveness, and hindered the development of its application, which is still far from being common in modern buildings (Kowalski 2009).

Until very recently, with the development of drug resistant TB, UVGI effectiveness for air disinfection was officially acknowledged, and was recommended for use in hospitals as a supplement to other air cleaning methods, such as pressurization, dilution, or filtration (CDC 1994, 2005; Beggs 2002a, 2002b; Kowalski 2009; Memarzadeh 2010). UVGI effectiveness to prevent infection on its own was still not considered to be reliable (Memarzadeh 2000b; Miller

2000). When working with ventilation systems, UVGI can disinfect areas where ventilation is not effective (Memarzadeh 2000b). The relationship between UVGI effectiveness and ventilation rate is not simple, but generally UVGI works best at low ventilation rates (< 6 ACH) (Beggs 2002b; Xu 2003). UVGI is also believed to work complementarily with filtration systems, since filtration generally has high efficiency for larger particles, while UVGI is more effective for smaller particles, for which the protection from irradiation is much weaker (Jensen 1964; Kowalski 2001).

UVGI has been suggested to be a better method for indoor air disinfection than changing temperature or humidity, as the latter would cause discomfort and cost more energy (Memarzadeh 2012). For indoor applications of UVGI, the upper-room system and the in-duct system are the two configurations that have been most commonly studied and used (Wells 1938; McLean 1961; Riley 1962; Jagger 1965; Ko 2002; CDC 2005; van Osdell 2002; Xu 2003, 2005; Kujundzic 2007; Rudnick 2009). When installed in an air handling unit, UVGI also reduces mold growth on coils and saves energy by minimizing pressure drop. When installed as an upper-room system, louvers are used to direct and confine UV light to the upper part of room to avoid direct exposure to the occupants. Ventilation is also designed to create multiple passes of air in the UV irradiated region to maximize the disinfection effect. UVGI disinfection systems can be also designed as a moveable unit, which can be used to decontaminate unoccupied rooms.

The low pressure mercury lamps which are most frequently used in UVGI systems generate 253.7 nm UVC with about 90% of their spectral output (Luckiesh 1946; Summer 1962; NIOSH 1972; Navy Environmental Health Center 1992; Rahn 1999; IESNA 2000; Xu 2003; Hijnen 2006). In fluorescent lamps for illumination, the glass is coated on the inside with phosphors which absorb UV and re-emit the energy as visible light. In UV lamps, no phosphor is used, and the quartz glass is almost transparent to the UVC wavelength. Softglass (sodium-barium glass) is often used instead of quartz glass to block 185 nm light for ozone-free requirements (Xu 2003; Kowalski 2009; Schalk 2006). Cooling of the lamp surface by an airstream can reduce its output. For optimal operation, airstreams directed toward the lamps should be avoided and an ambient temperature between 20 ˚C and 24 ˚C is recommended (Kowalski 2001, 2009; Memarzadeh 2010).

6.2 Test method

UVGI effectiveness was tested with MS2, AIV, and HAdV-1 by comparing virus relative recovery and survival with and without UVGI. The test condition was 25 ˚C, 50% RH, and 15 ACH, the same as the one-hour tests described in Chapter 4. The test setup was not changed from the previous tests either. Two UVGI lamps in opposite corners of the chamber ceiling were used as described in Chapter 2. Each lamp tube was Model G25T8 from General Electric, with a 6.9 W nominal output at 253.7 nm. The lamps were ozone free, thus virus inactivation due to ozone effect was unlikely. Before each UVGI test, both lamps were turned on for 30 min to warm up as in other studies (Thurston-Enriquez 2003; Xu 2003). The UVGI strength was assumed to be constant afterwards. In this study, the service time of the two UVGI lamps during these tests were between 200 and 300 hours; comparing with the 8000 hour designed service life, the output should be close to the peak (Kowalski 2009). Tests were conducted in triplicate, and the test order was randomized. The uncertainties were the same as those calculated in the previous tests, as they were assumed to be independent on the operation of the UVGI system. ANOVA was performed on a logarithmic scale to test the significance of UVGI to virus inactivation based on the samples from stages 3-7 in an Andersen impactor.

6.3 Results and discussion

The size distributions of the normalized live virus titer for each virus are plotted in FIGURE 6.3.1. The corresponding uncertainties are listed in TABLE 6.3.1. The overall normalized live virus titers for all impactor stages are shown in FIGURE 6.3.2. ANOVA p-values are listed in TABLE 6.3.2. For normalized live virus titer, the virus type, particle size, and UVGI operation were all significant factors, but none of their interactions was significant. From FIGURE 6.3.2, all viruses had higher total loss when UVGI was on.

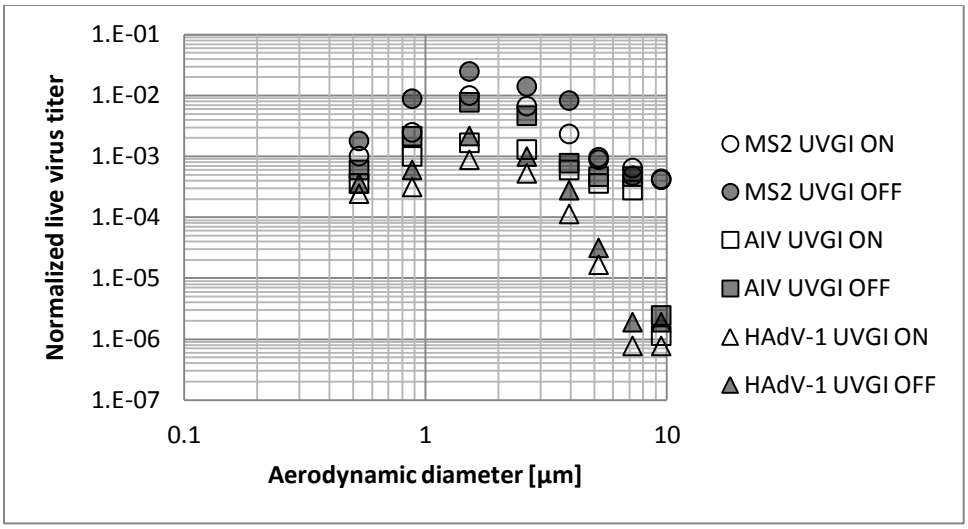

FIGURE 6.3.1 Normalized live virus titer (dimensionless) versus particle aerodynamic diameter [µm] for MS2, AIV, and HAdV-1 with and without UVGI.

TABLE 6.3.1 Pooled relative standard deviation for each virus in FIGURE 6.3.1.

Virus	MS2	AIV	HAdV-1
Relative standard deviation	+167.7%/-62.6%	+271.9%/-73.1%	+135.7%/-57.6%

The size distributions of the normalized fluorescence intensity are shown in FIGURE 6.3.3. The pooled relative standard deviation for all viruses was calculated to be +33.2%/-24.9%. The ratios plotted on the right part of FIGURE 6.3.4 are all close to unity, showing that fluorescein was not damaged by UVGI. It also implies that the amount of aerosol collected by the Andersen impactor with and without UVGI was constant.

By ANOVA (TABLE 6.3.3), virus type and the interaction between virus type and particle size were both significant, which is similar to the previous results in Chapters 2 and 3. The difference was likely caused by suspension medium, as MS2 was significantly different from HAdV-1 ($p=0.002$), while AIV was not ($p=0.779$). The interaction between virus type and UVGI was significant, meaning that for different viruses or suspensions UVGI had different effects on normalized fluorescence intensity. From FIGURE 6.3.4, the difference is not obvious, and might be due to test uncertainties.

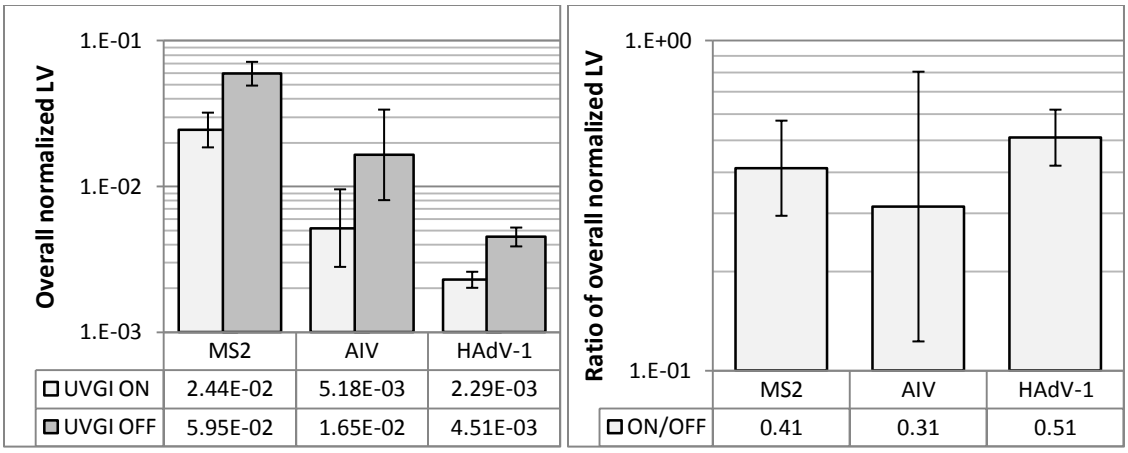

FIGURE 6.3.2 Overall normalized live virus (LV) titer (dimensionless): left is the direct comparison of UVGI "on" and "off"; right is the ratio of "on" over "off". Error bars are standard errors.

TABLE 6.3.2 P-values for normalized live virus titer with the significant factors in bold.

Factor	Virus	Size	UVGI	V:S	V:U	S:U	V:S:U
P-value	**<0.001**	**<0.001**	**<0.001**	0.735	0.868	0.911	0.986

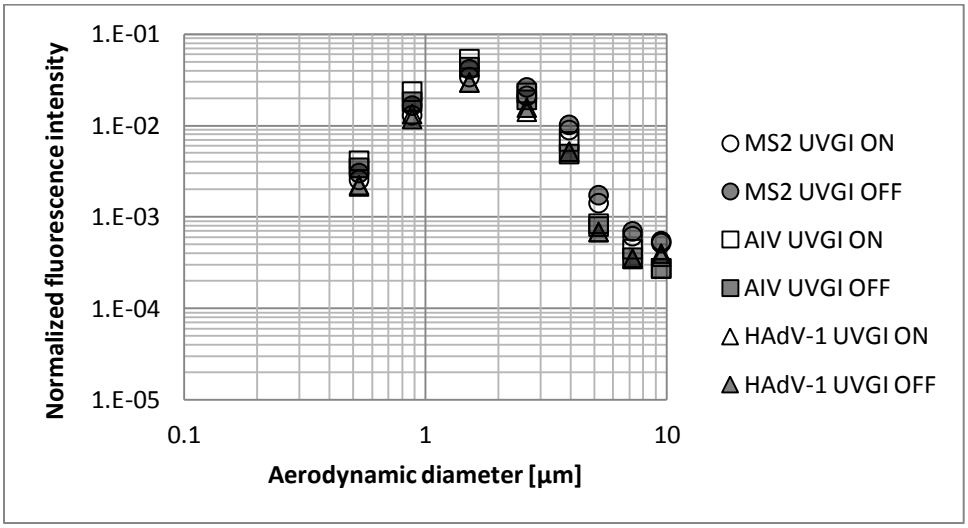

FIGURE 6.3.3 Normalized fluorescence intensity (dimensionless) versus particle aerodynamic diameter [µm] for MS2, AIV, and HAdV-1 with and without UVGI.

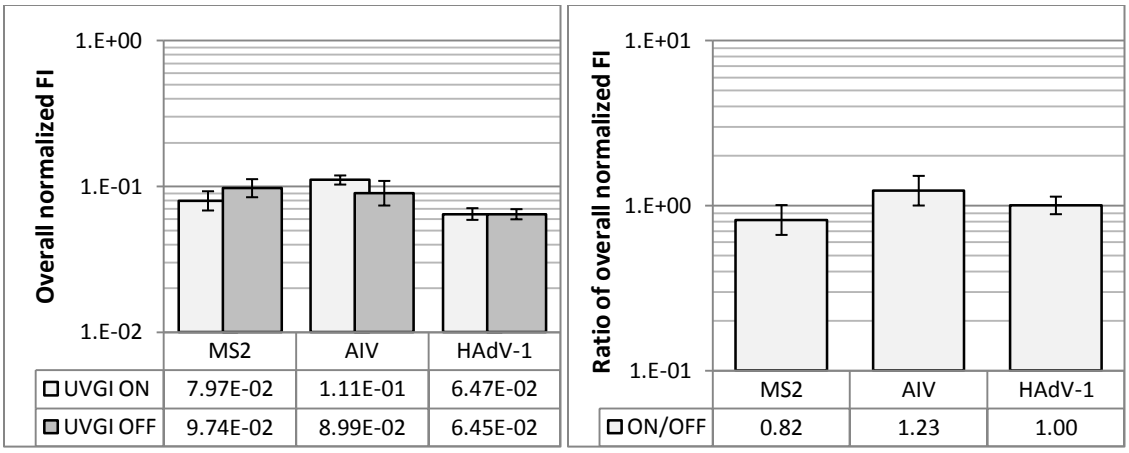

FIGURE 6.3.4 Overall normalized fluorescence intensity (FI) (dimensionless): left is the direct comparison of UVGI "on" and "off"; right is the ratio of "on" over "off". Error bars are standard errors.

TABLE 6.3.3 P-values for normalized fluorescence intensity with the significant factors in bold.

Factor	Virus	Size	UVGI	V:S	V:U	S:U	V:S:U
P-value	**<0.001**	**<0.001**	0.843	**0.006**	**0.012**	0.971	1.000

The normalized total virus concentration results are shown in a similar way in FIGURES 6.3.5-6.3.6 and TABLES 6.3.4-6.3.5. From the UVGI on/off ratio plot (FIGURE 6.3.6) and the significant p-value of UVGI effect, it can be seen that some of the viruses were damaged by UVGI, and could not be detected by PCR. Since UVGI damages the nucleic acid, and PCR measurements rely on the sequence of the DNA or RNA, the reduction in total virus measurement was reasonable. However, the issue also means that using the total virus concentration would falsely overestimate the physical losses of virus in these tests. Virus type was also a significant factor; similar to previous tests, MS2 was significantly different from HAdV-1 (p=0.003), while AIV was not (p=0.808). The reason could be the difference in suspension medium, virus size, or genetic material.

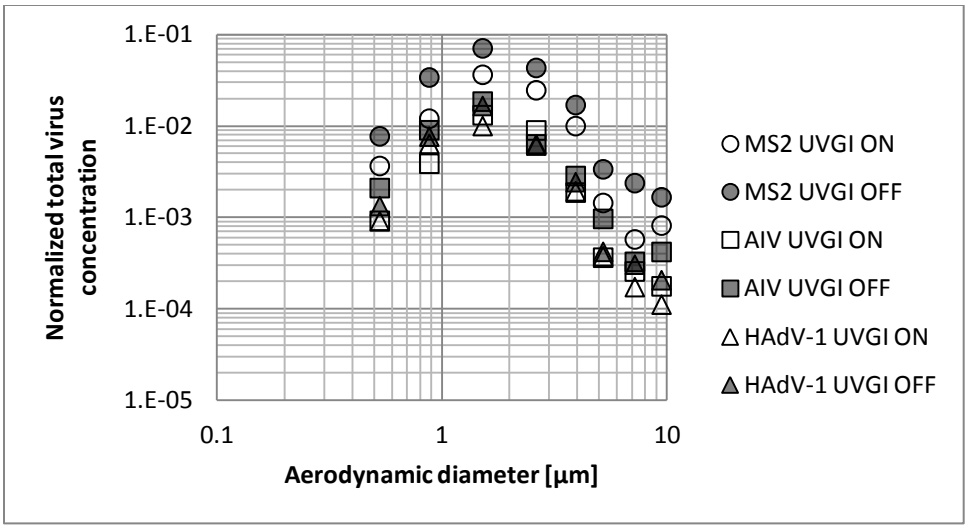

FIGURE 6.3.5 Normalized total virus concentration (dimensionless) versus particle aerodynamic diameter [µm] for MS2, AIV, and HAdV-1 with and without UVGI.

TABLE 6.3.4 Pooled relative standard deviation for each virus in FIGURE 6.3.5.

Virus	MS2	AIV	HAdV-1
Relative standard deviation	+119.4%/-54.4%	+99.5%/-49.9%	+115.5 %/-53.6%

For biological losses, the results of relative recovery are shown in FIGURES 6.3.7-6.3.8 and TABLES 6.3.6-6.3.7. The results of survival are shown in FIGURES 6.3.9-6.3.10 and TABLES 6.3.8-6.3.9. UVGI significantly reduced the relative recovery of the three viruses, but the effect is not significantly different from virus to virus by ANOVA. In FIGURE 6.3.8, the inactivation of AIV might be the greatest by mean value, but the uncertainty is also the greatest. Relative recovery is not significantly affected by the interaction between particle size and UVGI, showing that the UVGI effect is similar for the particle size range from 0.4 to 4.7 µm.

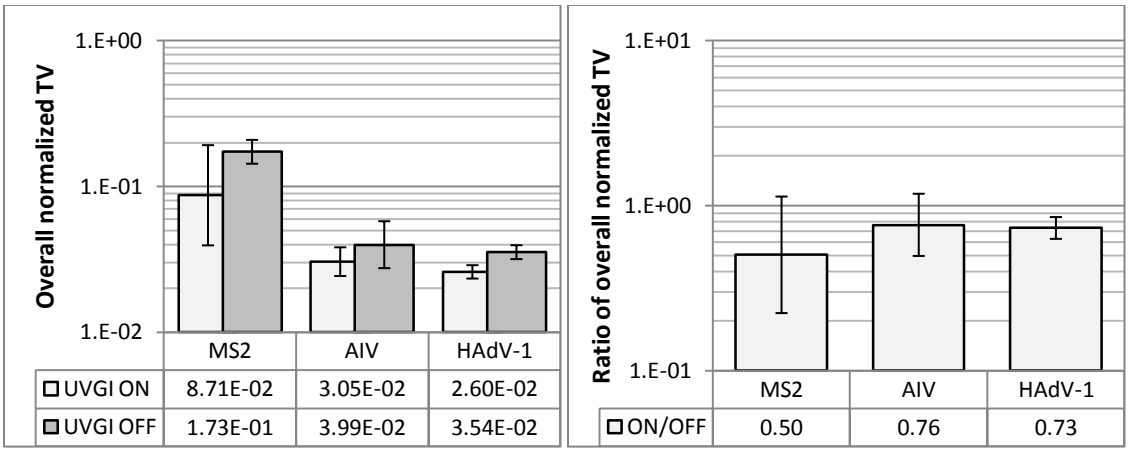

FIGURE 6.3.6 Overall normalized total virus (TV) concentration (dimensionless): left is the direct comparison of UVGI "on" and "off"; right is the ratio of "on" over "off". Error bars are standard errors.

TABLE 6.3.5 P-values for normalized total virus concentration with significant factors in bold.

Factor	Virus	Size	UVGI	V:S	V:U	S:U	V:S:U
P-value	**<0.001**	**<0.001**	**0.007**	0.976	0.518	0.751	0.995

For survival, virus type was significant as it was for relative recovery. UVGI was not significant, meaning that UVGI did not significantly reduce virus survival. This proves that UVGI damages nucleic acid causing similar reductions in live virus titer and total virus concentration. In other words, most viruses inactivated by UVGI were undetectable by PCR as well. From FIGURE 6.3.10, however, ratios of the three viruses were still slightly below unity by mean value, showing some viruses inactivated by UVGI could still be detected by PCR. An explanation is that for these viruses, UVGI damaged a part of DNA/RNA which was not the target sequence used by PCR, making them incapable of multiplying, but still replicable by PCR. Interaction between UVGI and particle size was not significant, meaning that UVGI effect could be considered constant for the particle sizes between 0.4 and 4.7 μm.

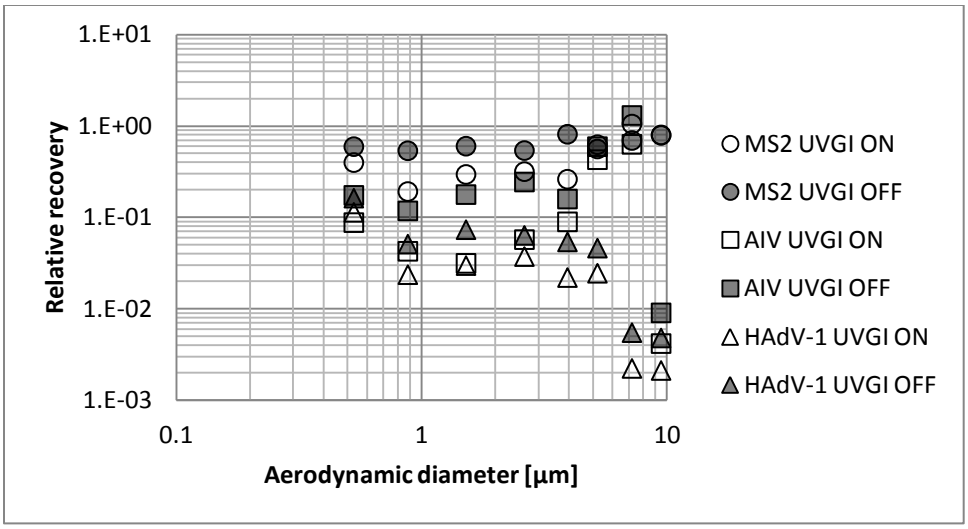

FIGURE 6.3.7 Relative recovery (dimensionless) versus particle aerodynamic diameter [µm] for MS2, AIV, and HAdV-1 with and without UVGI.

TABLE 6.3.6 Pooled relative standard deviation for each virus in FIGURE 6.3.7.

Virus	MS2	AIV	HAdV-1
Relative standard deviation	+160.9%/-61.7%	+311.0%/-75.7%	+167.0%/-62.5%

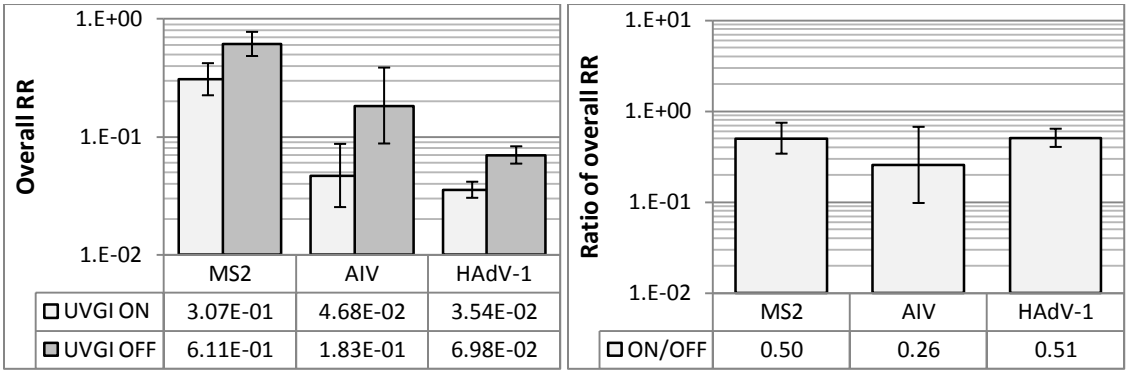

FIGURE 6.3.8 Overall relative recovery (RR) (dimensionless): left is the direct comparison of UVGI "on" and "off"; right is the ratio of "on" over "off". Error bars are standard errors.

TABLE 6.3.7 P-values for relative recovery with significant factors in bold.

Factor	Virus	Size	UVGI	V:S	V:U	S:U	V:S:U
P-value	**<0.001**	0.253	**<0.001**	0.862	0.728	0.923	0.994

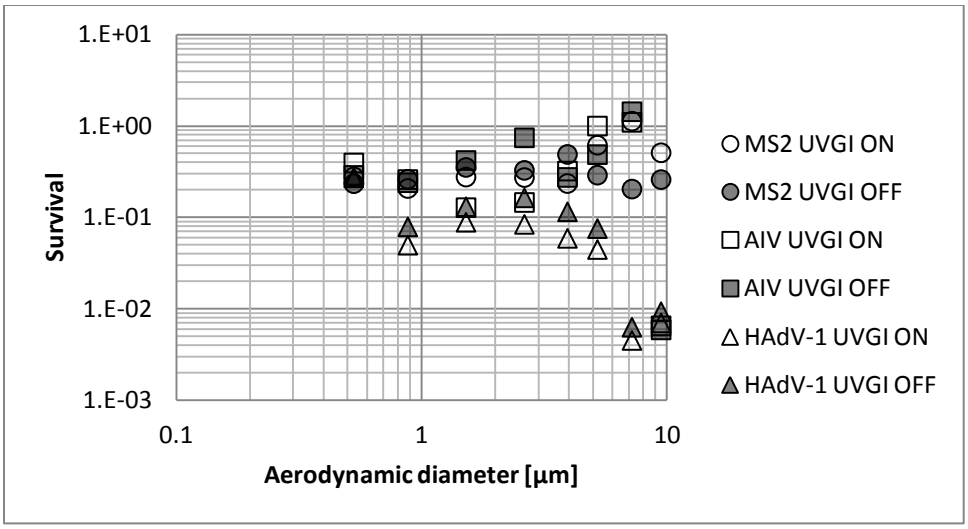

FIGURE 6.3.9 Survival (dimensionless) versus particle aerodynamic diameter [µm] for MS2, AIV, and HAdV-1 with and without UVGI.

TABLE 6.3.8 Pooled relative standard deviation for each virus in FIGURE 6.3.9.

Virus	MS2	AIV	HAdV-1
Relative standard deviation	+176.4%/-63.8%	+398.6%/-79.9%	+250.2%/-71.4%

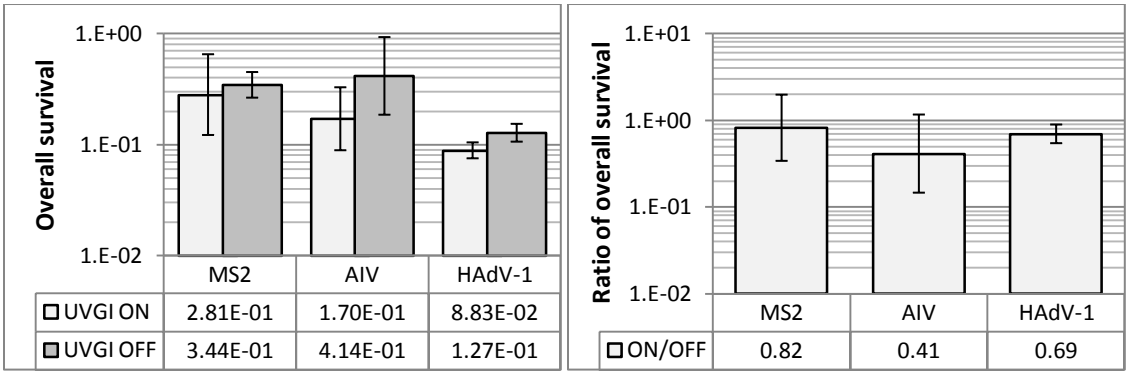

FIGURE 6.3.10 Overall survival (dimensionless): left is the direct comparison of UVGI "on" and "off"; right is the ratio of "on" over "off". Error bars are standard errors.

TABLE 6.3.9 P-values for survival with significant factors in bold.

Factor	Virus	Size	UVGI	V:S	V:U	S:U	V:S:U
P-value	**0.018**	0.771	0.211	0.961	0.950	0.864	0.990

Since UVGI damaged the virus nucleic acid, most of the inactivated virus could not be detected by either cell-culture titration or PCR, resulting in underestimated UVGI effectiveness based on survival. Because fluorescein was not affected by UVGI, relative recovery could be used instead of survival to calculate the UVGI effectiveness. In the previous tests for different sampling durations discussed in Chapter 4, it was shown that even though relative recovery was different from survival, the six-hour to one-hour ratios of the two parameters were similar. This is possibly because any offset due to the use of fluorescein should be similar for six-hour and one-hour tests, and can be cancelled by taking the ratio. The conclusion should still be true for the UVGI tests, and the ratio of UVGI on over off for relative recovery should be close to that for the actual survival (rather than the measured virus survival using PCR analysis). Based on the relative recovery data, the average inactivation rates for the three viruses were: 49.8% for MS2, 74.5% for AIV, and 49.3% for HAdV-1. AIV was more susceptible to UVGI than MS2 or HAdV-1, and the latter two had similar resistances. This agrees well with published data. However, the uncertainty with AIV was also much larger, making it desirable to conduct further tests to verify this conclusion.

6.4 Conclusions

This group of tests showed that UVGI was effective in controlling viral aerosol transmission even for a hardy enteric virus such as HAdV-1. UVGI damaged the virus at the nucleic acid making most inactivated viruses undetectable by PCR as well, resulting in significantly overestimated survival of the irradiated viral aerosol. Since fluorescein did not seem to be affected, relative recovery was used to calculate the disinfection effectiveness of UVGI. The inactivation rates showed that AIV could be more susceptible to UVGI than MS2 or HAdV-1, and the latter two were similar. This result agrees with published data. However, more tests are needed, as the uncertainty with AIV was large, and the inactivation rates for the three viruses were not significantly different in the ANOVA results. For all three viruses, the inactivation rates were smaller than one log, indicating that the UVGI dose received might not be very high. As shown in Appendix II, the average residence time of the collected aerosol was only about 2 minutes, compared to the test duration of one hour. In order to increase inactivation, either more UVGI power or longer residence time is needed. The performance of the UVGI system was further

investigated using a numerical method as shown in the next chapter, where the dose received by the aerosol was calculated based on the irradiance field and particle trajectories in the chamber. It is recommended for future research to test the effects of suspension medium and humidity (especially at extreme levels) on viral aerosol susceptibility to UVGI for different viruses.

7 Numerical simulation of viral aerosol inactivation by UVGI

7.1 Introduction

In the experiment, the three test viruses were significantly inactivated by UVGI. AIV was more susceptible to UVGI than MS2 or HAdV-1, and MS2 had a similar resistance with HAdV-1. This result agrees qualitatively with previous studies. In order to compare quantitatively with published data, and to contribute to the database of UVGI effects on viral aerosols, the susceptibilities of the test viruses need to be quantified based on the experimental results. To accomplish this, a numerical model was developed in ANSYS CFX (13.0, ANSYS, Inc.). The model could serve as a prototype that can be used as a basis for applications to facilitate the test or design of UVGI systems.

The numerical model consisted of three parts: flow field simulation, particle transport simulation, and UVGI field simulation. It directly output the trajectories of the particles that were collected by the sampler, and the irradiance field. The output was then post-processed to calculate the UV dose received by each particle, and eventually the susceptibility of each virus. The model is conceptually similar to those in several past studies on aerosol or water disinfection problems (Blatchley 1998, 2007; Memarzadeh 2000a; Alani 2001; Wright 2001; Beggs 2002b; Noakes 2004a, 2004b, 2006).

In the previous studies, particle transport simulation was conducted in either the Lagrangian or Eulerian framework. For steady state problems, both methods give similar results, but for unsteady state problems, the Lagrangian method is more suitable (Alani 2001; Memarzadeh 2004; Noakes 2004b; Ducoste 2005; Sozzi 2006; Gao 2007; Zhang 2007a; Jeong 2009; Wan 2009). The Eulerian method solves an additional scalar differential transport equation in parallel with the Navier-Stokes equations, and is capable of showing local concentration and inactivation rate in the results (Verstaag 1995; Memarzadeh 2004; Sozzi 2006; Mazumdar 2008; Yan 2009). On the

other hand, the Lagrangian method tracks a large number of particles, thus the particle movement or trajectories are visible, and the dose distribution of the collected particles can be calculated (Sozzi 2006; Zhang 2006, 2007a; Wan 2009). Due to the stochastic nature of particle tracking, a great number of trajectories are needed for the Lagrangian method so that the result reaches statistical stability before any further analysis such as susceptibility calculation can be carried out. In the current model, particle transport was conducted in the Lagrangian framework, calculating trajectories with a particle tracking algorithm.

Some models in previous studies integrated the inactivation kinetics in the simulation (Noakes 2004b; Ducoste 2005; Sozzi 2006), while others did not (Memarzadeh 2000b; Alani 2001; Wright 2001). Those without inactivation kinetics required post-processing to determine inactivation rate from susceptibility or vice versa. With the kinetics included, the inactivation rate could be directly shown in the simulation results. However, the drawback is that the kinetic function is usually fixed; if a change of kinetics is needed, the entire simulation needs to be run again. Another major drawback with integrated kinetics is the accuracy is limited by the availability of reliable susceptibility constants for airborne microorganisms (Noakes 2004b). In this study, since the calculation was performed in reverse, from inactivation rate to susceptibility based on simulated dose distribution, the inactivation kinetic function was not included in the numerical model.

7.2 Flow field simulation

7.2.1 Background of turbulence models

The turbulent flow field simulation is the basis for calculation of particle trajectories, especially for particles smaller than 10 μm (Wan 2009; Gao 2007). With the development of both hardware and software, computational fluid dynamics (CFD) has become one of the primary tools for studying indoor air flow (Nazaroff 1987; Wan 2009). For the incompressible, Newtonian air flow in the chamber, the basic equations used for the flow field simulation in the Eulerian framework are the Reynolds-averaged Navier-Stokes (RANS) equations, which include conservation of mass, conservation of momentum, and conservation of energy:

$$\frac{\partial \rho}{\partial t} + \frac{\partial \rho U_i}{\partial x_i} = 0 \ (C.O.Mass), \tag{7.2.1}$$

$$\frac{\partial \rho U_i}{\partial t} + \frac{\partial \rho U_j U_i}{\partial x_j} = \frac{\partial}{\partial x_j}\left(\mu \frac{\partial U_i}{\partial x_j} - \rho \overline{u_\iota u_j}\right) - \frac{\partial p}{\partial x_i} + S_{Ui}\ (C.O.Momentum), \tag{7.2.2}$$

$$\frac{\partial \rho c_p T}{\partial t} + \frac{\partial \rho c_p U_j T}{\partial x_j} = \frac{\partial}{\partial x_j}\left(k \frac{\partial T}{\partial x_j} - \rho c_p \overline{u_j t}\right) + S_T\ (C.O.Energy), \tag{7.2.3}$$

where ρ is fluid density, t is time, U_i and U_j are the velocities in x_i and x_j directions respectively, $\overline{u_\iota}$ and $\overline{u_j}$ are the average turbulent fluctuations of U_i and U_j respectively, μ is fluid dynamic viscosity, S_{Ui} is the source term for the momentum in x_i direction, c_p is fluid specific heat capacity, T is temperature, k is heat conductivity, and S_T is the source term for thermal energy. EQUATION 7.2.3 is the differential transport equation for the scalar quantity of temperature. With a suitable substitution of parameters, it can also be used for other scalar quantities such as concentration.

To predict the turbulent flow field, a turbulence model must be included in the simulation. The choice of a proper turbulence model can be critical for simulation accuracy. Since the chamber environment simulated a typical indoor environment featuring low Reynolds number, low turbulence intensity, and large recirculation eddies, all flow regimes including laminar, transitional, and turbulent flows might be present at the same time. Therefore, a proper turbulence model should handle this situation well.

The turbulence models most frequently used with the RANS equations for indoor air flow simulations are k-ε and k-ω models. Both models consider turbulence effects as an increase in fluid viscosity, and calculate this by solving two additional differential transport equations. As shown in their names, k-ε models solve for turbulence kinetic energy (TKE) k and the dissipation rate of TKE ε, while k-ω models solve for k and turbulence frequency ω. The increase in fluid viscosity is named turbulent viscosity μ_t, which is calculated differently by the two models:

$$\mu_t = C_{\mu 1} \rho \frac{k^2}{\varepsilon}\ (k - \varepsilon\ models), \tag{7.2.4}$$

$$\mu_t = C_{\mu 2} \rho \frac{k}{\omega}\ (k - \omega\ models), \tag{7.2.5}$$

where $C_{\mu 1}$ and $C_{\mu 2}$ are empirical coefficients for the two models. The final viscosity of the fluid is named effective viscosity μ_{eff}:

$$\mu_{eff} = \mu + \frac{\mu_t}{\sigma}, \tag{7.2.6}$$

where the empirical coefficient σ has different values for momentum, k, ε, and ω equations based on which turbulence model is used. The exact formulation of k-ε and k-ω models can be found in several CFD publications (Nieuwstadt 1992; ANSYS 2010).

The standard k-ε model is robust, economic to run, and has reasonable accuracy for a broad range of turbulent flows, including indoor air flow (Posner 2003). For better accuracy, the turbulent flow has to be fully developed. This is not true for low Reynolds number indoor air flows, for which the model has been reported to overestimate the turbulent diffusivity, and its overall accuracy was also unsatisfactory (Liang 1994). Therefore, several modifications in the equations for k, ε, and μ_t have been made based on the standard model to improve the validity for low Reynolds number flows (Henkes 1990; Xu 1994). Among the modified models, the renormalization group (RNG) k-ε model, which was derived with the renormalization group methods (Yakhot 1986; Choudhury 1993), was often recommended for indoor air flow simulations (Chen 1995, 2001; Yuan 1999; Srebric 2002; Posner 2003; He 2005; Lai 2007; Zhang 2007b; Chao 2008; Qian 2009; Wan 2009). The only difference between RNG and standard k-ε models is in the definition of a coefficient in the transport equation for dissipation rate (ε). The small change improves the accuracy for low Reynolds number flows while remaining accurate for high Reynolds number flows (van Hooff 2012). Compared with the standard k-ε model, the RNG model performs better for natural, forced, and mixed convection flows (Chen 1995). It also performs better for re-circulating flows over an obstruction or after a backward-facing step (Papageorgakis 1999; Posner 2003). However, the RNG model does not perform as well as the standard model for jet flows (free shear flows) in both convergence and accuracy (Papageorgakis 1999).

The shear stress transport (SST) model has also been tested frequently for indoor air flow simulations. The SST model utilizes k-ω model within boundary layers, and k-ε model for the far-field. As a result, it has better accuracy within boundary layers compared to k-ε models, and is accurate with jet flow and prediction of the onset and the amount of flow separation under adverse pressure gradients (Cook 1998; Yang 2007). Since the SST model uses the standard k-ε model for the far-field, it has been reported to perform similarly to the standard k-ε model, and predict indoor air flow fields and thermal plumes less accurately than the RNG model (Cook 1998). However, another study showed better prediction with the SST model than with either the standard k-ε or the RNG model for the temperature distribution in a full-scale displacement ventilation case (Mustakallio 2012). Since the chamber air flow may have flow transition between laminar and turbulent regimes, the accurate prediction of transition onset could be important for

the overall accuracy. In CFX 13.0, several transition models are available for the SST model. The full transitional model, also named the "gamma-theta" model, is based on two additional transport equations for the intermittency (gamma) and the transition onset criteria in terms of momentum thickness (theta) Reynolds number. The full transitional model has been extensively validated together with the SST model for a wide range of transitional flows, and is recommended for general-purpose applications (ANSYS 2010).

In the current simulation, the RNG model, the SST model, and the SST model with the full transitional model were first compared in two benchmark tests, and the best one was chosen for the chamber simulation.

7.2.2 Treatment of near-wall regions

Due to the no-slip condition at the wall boundaries, flow is always laminar close to the wall. Since the standard k-ε model is valid only for fully turbulent flows, the flow near the wall boundaries must be solved with empirical wall functions (Tennekes 1972). Within the wall boundary layers, the velocity profile can be approximately described as a logarithmic function of distance from the wall. The wall function is thus used to describe the flow in this log-law region.

In CFX 13.0, the "scalable wall function" is used for the RNG model, allowing the use of the logarithmic velocity profile approximation near the wall boundaries where mesh was not fine enough. For the SST model, the near wall region is solved using the "automatic wall function", which switches between k-ω formulation and the "scalable wall function" based on the adjacent flow field and mesh size (ANSYS 2010). The "automatic wall function" works based on the dimensionless distance between the first and the second node from the wall, which is denoted as $y+$ (or y-plus). This parameter is also often used as a check for mesh quality, especially when boundary layer flow is important. For simulations looking for information within the boundary layer, low $y+$ is needed, meaning several nodes need to be placed inside the boundary layer. For the current simulation, the information inside the boundary layer is not important, so $y+$ does not need to be very small. However, it still needs to be smaller than 200 for the turbulence models and the wall functions to work correctly (ANSYS 2010).

7.2.3 CFD benchmark tests for turbulence models

Since the selection of a proper turbulence model is critical for overall simulation accuracy, benchmark tests were conducted to compare the RNG k-ε model, the SST model, and the SST with the full transitional model. Similar flow cases were chosen as the benchmark models. A grid independence test was conducted by comparing the result of the original mesh and that of a fine mesh with the number of elements doubled.

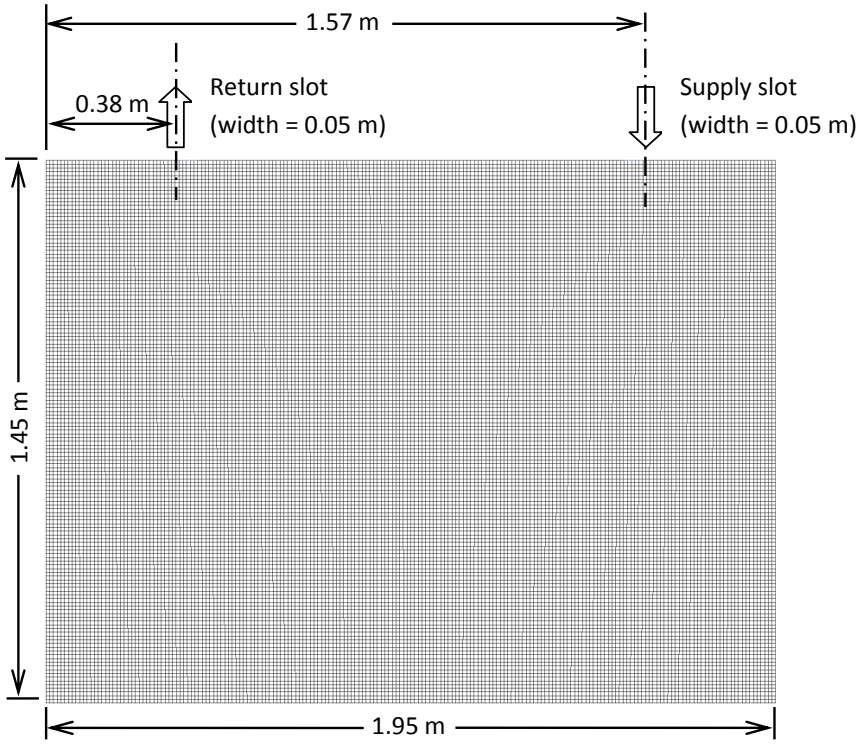

FIGURE 7.2.1 The two-dimensional chamber model showing main dimensions and the original mesh for the first benchmark test.

The first benchmark test used the experimental (Liang 1994) and numerical (Xu 1994) studies in the same chamber as the current study. At the time when the studies were conducted, the chamber was empty with two linear slot openings as supply and return to create a two-dimensional flow field on its center plane. Despite these differences, it is still very similar to the current case, and could serve as a great reference. The two-dimensional simulation area was 1.95 m wide and 1.45 m tall. The width of supply and return slots was 0.05 m. The distance between supply slot

centerline and right wall was the same as that between return slot centerline and left wall, and was 0.38 m. Two meshes were created; the original mesh had 57524 nodes and 28420 hexahedra elements, and the fine mesh had 117458 nodes and 58240 hexahedra elements. The SST model was used to compare the two meshes for grid-independence. The model with the original mesh is shown in FIGURE 7.2.1. The simulation condition was isothermal, and the air flow velocity at inlet was 1.02 m/s, corresponding to a Reynolds number of 3200. The convergence criteria were 1e-5 for the root-mean-square (RMS) residuals in momentum and mass conservation equations.

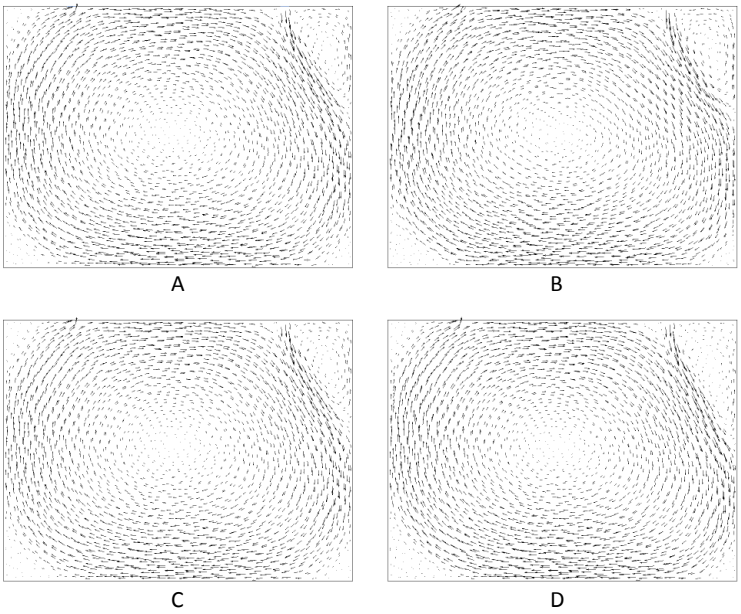

FIGURE 7.2.2 Velocity vectors for the first benchmark test with different turbulence models and mesh sizes: A. SST with original mesh; B. SST with fine mesh; C. SST with transitional model and original mesh; D. RNG with original mesh.

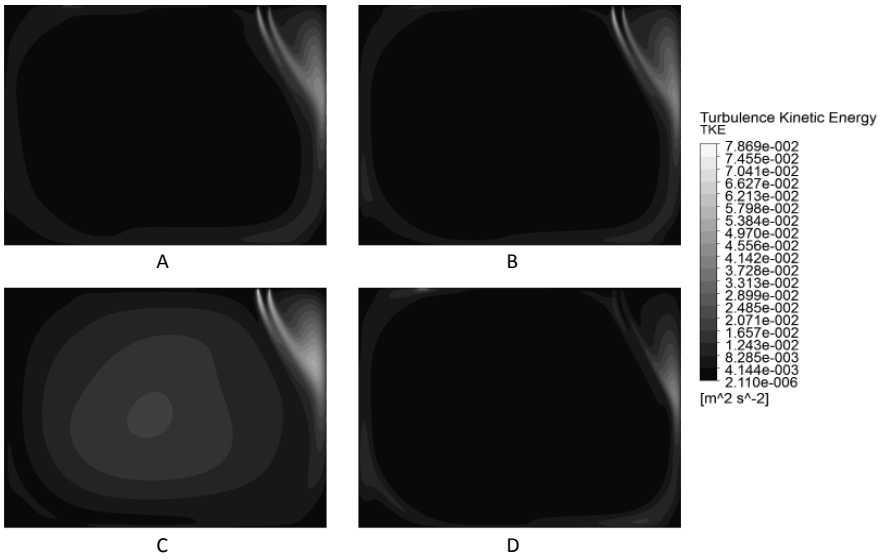

FIGURE 7.2.3 TKE contours for the first benchmark test with different turbulence models and mesh sizes: A. SST with original mesh; B. SST with fine mesh; C. SST with transitional model and original mesh; D. RNG with original mesh.

Velocity vectors and TKE contours are shown in FIGURES 7.2.2 and 7.2.3 respectively to compare the different turbulence models and mesh sizes. The flow field was affected by the Coanda effect; the main jet coming out of the supply slot attached to the right wall and moved around the chamber along the walls and floor before returning to the air handling unit. Low velocity magnitude was found in the center of the chamber, where a large eddy formed. In FIGURE 7.2.2, the SST model over-predicted velocity magnitude in the eddy in the upper right corner compared to the experiment of Liang. Adding the transitional model improved this slightly, but was still not as accurate as the RNG model. Otherwise all the models predicted the velocity field very similarly, and generally agreed well with experiment measurement. The two meshes with the SST model showed similar results. In FIGURE 7.2.3, high TKE was generally associated with the main stream going around the chamber. The SST model predicted higher TKE than the RNG model, especially near the inlet. Elsewhere, the SST model predicted TKE similarly with the RNG model, but the SST with transitional model falsely showed high TKE in the center of chamber. On the other hand, the RNG model generally predicted TKE well, except near the return, where it showed some high TKE values, which was not detected in the experiment. The two meshes with the SST model showed very similar TKE results as well. In summary, the RNG

model was slightly better than the SST model. The full transitional model did not make the prediction of the SST model more accurate.

The second benchmark test was based on a published model in Wang 2009 and Jin 2012. In their studies, both the SST and RNG models agreed well with experiment for velocity profiles. However, the SST over-predicted TKE, while the RNG prediction was accurate. As a summary, the RNG model was more accurate in the recirculation zones.

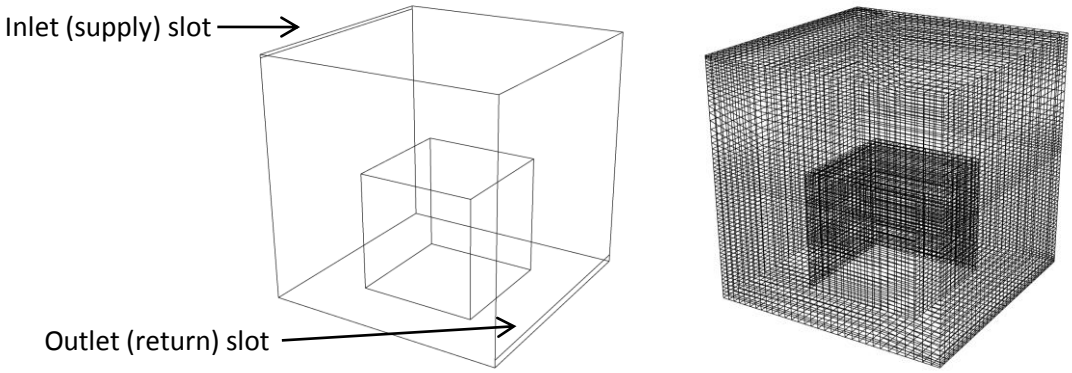

FIGURE 7.2.4 Perspective view of the three-dimensional model (left) and the original mesh (right) for the second benchmark test.

The model for the second benchmark test featured a transitional inlet boundary condition, turbulent flow, and mixed convection in a room with a box. The room was cubic with each side of 244 cm. The box was placed in the center of room, and had each side of 122 cm. The inlet slot was 3 cm wide, and outlet slot was 8 cm wide. The inlet velocity was 45.5 cm/s normal to the inlet face, and the temperature was 22.2 ˚C. The temperatures of box surface, ceiling, surrounding walls, and floor were 36.7 ˚C, 25.8 ˚C, 27.4 ˚C, and 26.9 ˚C, respectively as given in the referenced papers. The original mesh had 54630 nodes and 48960 hexahedra elements, and the fine mesh had 103399 nodes and 94544 hexahedra elements. The RNG model was tested for both meshes this time. The three-dimensional model and original mesh are shown in FIGURE 7.2.4. The convergence criteria were 1e-5 for the RMS residuals in the momentum, mass conservation, and energy transport equations. To compare with the published results, all the physics being studied located along the vertical line at the “position 6” in the original paper. The coordinate of

the line based on the model's top view was (23 cm, 122 cm), and is shown as an "X" in FIGURE 7.2.5.

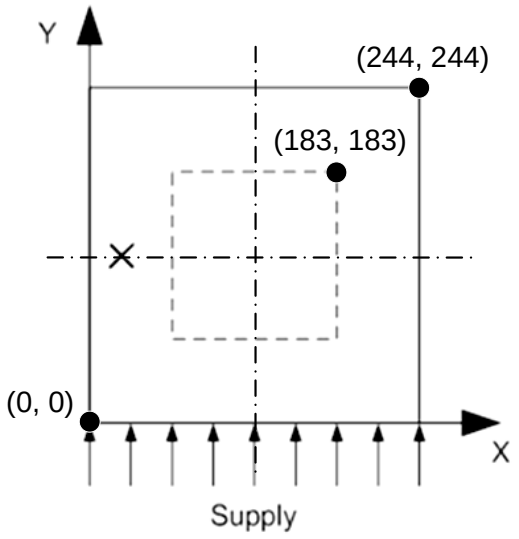

FIGURE 7.2.5 Location of the "Line 6" denoted as an "X" at (23, 122) in the top view of the room model. All coordinates are shown in centimeters.

From the velocity profiles along the Line 6 (FIGURE 7.2.6), the SST model over-predicted the velocity near the floor, and the transitional model improved the accuracy. The RNG model with both mesh sizes agreed well with experiment. In FIGURE 7.2.7, both SST models and the RNG model with either mesh size under-predicted the TKE near the floor and ceiling compared with experiment. In other locations, all the models predicted TKE well. For temperature profiles (FIGURE 7.2.8), all simulation results were greater than the experimental data, but the RNG model with both mesh sizes had better accuracy than the SST models. The full transitional model improved the prediction accuracy of the SST model. In the second benchmark test, adding the full transitional model slightly improved the overall prediction of the SST model, but it was still not as good as the RNG model. Due to the buoyancy flow in this benchmark test, the convergence was much slower than that of the first benchmark test. Based on the two benchmark tests as well as the published studies, the RNG k-ε model was chosen for the current environmental chamber simulation.

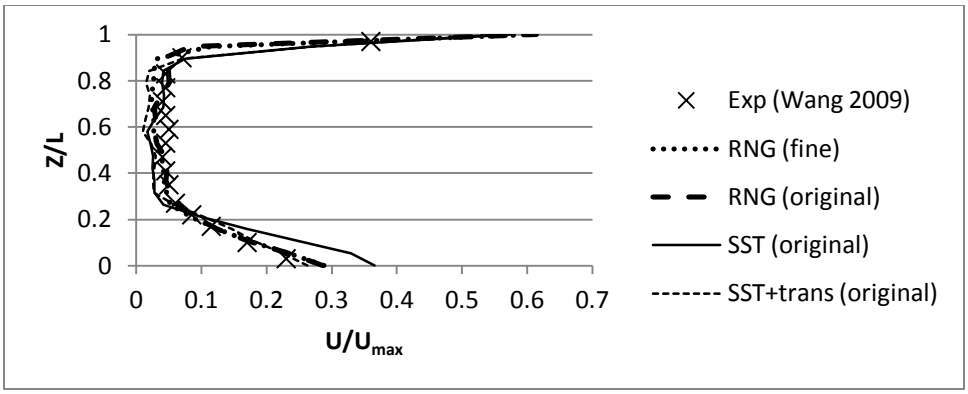

FIGURE 7.2.6 Dimensionless height from floor versus dimensionless velocity (dimensionless velocity profile) along "Line 6" with different turbulence models and mesh sizes.

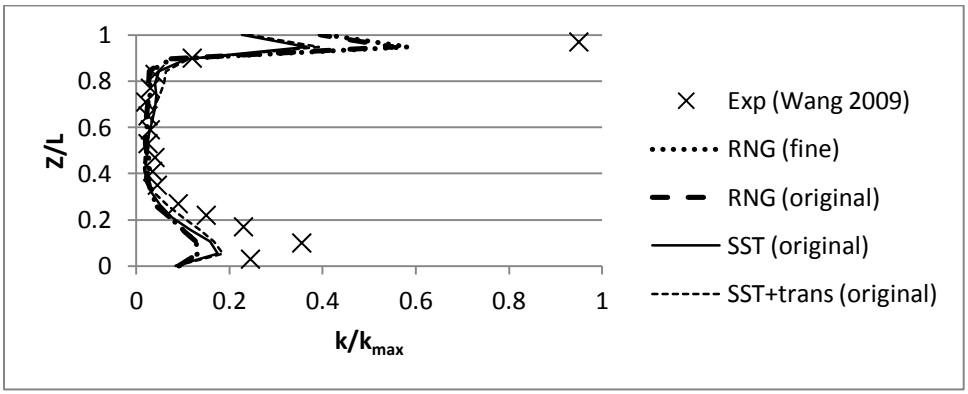

FIGURE 7.2.7 Dimensionless height from floor versus dimensionless TKE (dimensionless TKE profile) along "Line 6" with different turbulence models and mesh sizes.

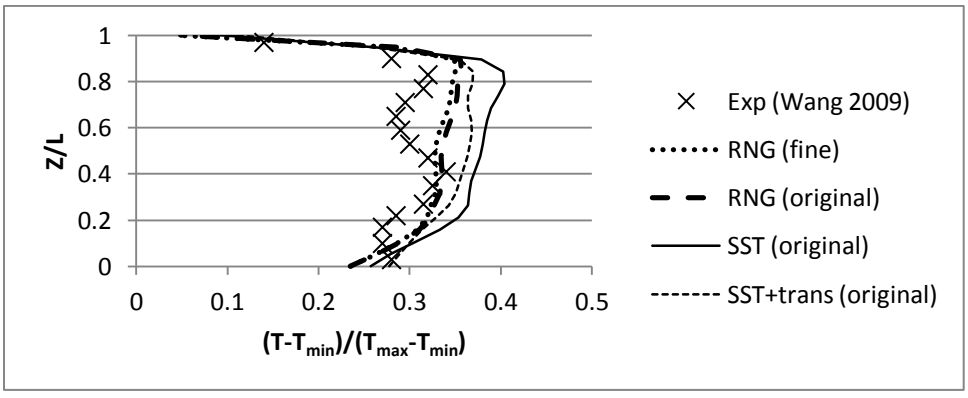

FIGURE 7.2.8 Dimensionless height from floor versus dimensionless temperature (dimensionless temperature profile) along "Line 6" with different turbulence models and mesh sizes.

7.2.4 Modeling the round supply diffuser with the momentum method

Other than the selection of a turbulence model, the modeling of the inlet boundary at the air supply diffuser was also critical for simulation accuracy (Memarzadeh 2000b; Srebric 2001). One solution was to model the supply diffuser with full detail, but the complex geometry would require an impractical amount of computational power to mesh and execute the simulation. This could also make convergence more difficult, while still not guaranteeing better accuracy. One reason was the different length scales required by the diffuser and the rest of the chamber, causing difficulty in mesh transition. Moreover, the turbulence model and other CFD settings suitable for the indoor air flow might not be suitable for the flow pattern between the diffuser vanes (Chen 2001b; Srebric 2001).

Therefore, several simplification methods for the inlet boundary condition have been developed for a fast and accurate simulation. These methods generally include the box method and the momentum method (Heikkinen 1991; Emvin 1996; Chen 2001b; Srebric 2001, 2002; He 2005). In short, the box method requires setting up an imaginary box containing the diffuser, and the assignment of velocity, temperature, and other conditions measured on the box boundaries. For the momentum method, on the other hand, the actual diameter of the diffuser is often used. By measuring volumetric flow rate and discharge velocity, an effective opening area is calculated and assigned to the model to decouple the momentum and mass conservation boundary conditions (Emvin 1996). Studies have been conducted to compare the two methods for different air supplies. For the round diffuser used in the current study, the momentum method is recommended due to its better accuracy in the jet region and fewer measurements that are required (Srebric 2001, 2002; He 2005).

As introduced above, to model both flow rate and jet penetration accurately for the diffuser, the momentum method uses an effective diffuser height instead of the actual one (FIGURE 7.2.9). The effective diffuser height can be calculated from the discharge jet velocity at the diffuser perimeter, diffuser diameter, and volumetric flow rate:

$$H_{eff} = \frac{A_{eff}}{\pi D} = \frac{Q}{U\pi D}, \tag{7.2.7}$$

where H_{eff} is the effective diffuser height, A_{eff} is the effective diffuser opening area, D is the model diameter which is usually the physical diameter of the diffuser, Q is the volumetric flow

rate, and U is the discharge velocity at the perimeter of the diffuser. Note that the effective diffuser height depends on the flow rate, thus it is not a constant; for another flow rate, the measurement and calculation need to be carried out again.

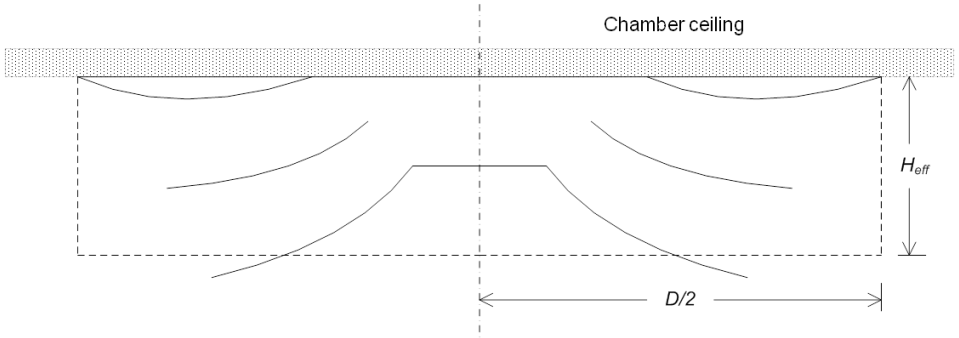

FIGURE 7.2.9 Cross-section of the round supply diffuser (solid lines) and its boundaries (dashed lines) used for the momentum method (EQUATION 7.2.7).

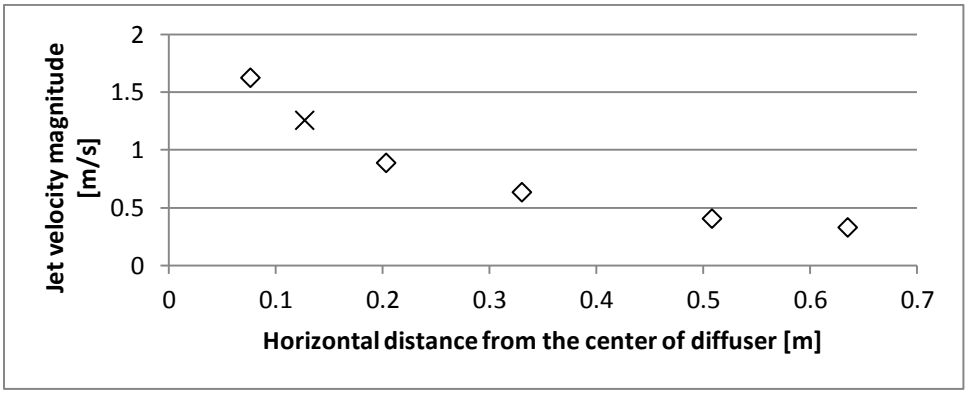

FIGURE 7.2.10 Jet velocity magnitude versus horizontal distance from the center of diffuser measured by the TSI VelociCheck hot wire anemometer, with "X" marking the location of the perimeter of the diffuser for the discharge velocity U in EQUATION 7.2.7.

In the current study, as the product information was not available for the diffuser, jet velocities were measured along the line from the supply diffuser to the return grille at the test ventilation rate of 53 ft^3/min (1500 l/min) (FIGURE 7.2.10). The measurement was taken with a hot wire anemometer (Model 8330 VelociCheck, TSI, Inc., Shoreview, MN) at its fast mode for the average velocity for the last three seconds. The discharge velocity at the perimeter of the 10 in

(25.4 cm) diffuser was thus found to be 248 ft/min (1.26 m/s). Using EQUATION 7.2.7, the effective diffuser height was calculated to be 2.4 cm.

Using the air kinematic viscosity (v) of 15.11e-6 m^2/s, the Reynolds number at the model inlet was estimated. The characteristic length or the hydraulic diameter of the modeled channel geometry was twice of the channel width, and was 4.9 cm. The corresponding Reynolds number was found to be 4003. For flow through the actual diffuser vanes, the characteristic length was twice the vane width, and was 2.5 cm. The average velocity between the vanes was measured to be about 320 ft/min (1.63 m/s). The corresponding Reynolds number was found to be 2740. Both Reynolds numbers suggest a typical low Reynolds number transitional inlet boundary condition. To accurately calculate the turbulence intensity at the inlet was difficult, as the flow in the diffuser was not fully developed. For typical HVAC cases, however, a medium intensity (about 5%) is generally recommended (ANSYS 2010), and the flow pattern was found to be very similar for the intensity set between 4% and 37% (Chen 2001b).

For the round diffuser, the asymmetry of the inlet air flow profile caused by the turning of the flexible duct upstream of the diffuser should be minimized and any offset should be considered in the simulation. The flexible duct upstream of the diffuser in this study was kept straight for greater than 10 times its inside diameter which was 6 in or 15.2 cm. Measurement was done at four orthogonal directions at 3 in (7.6 cm) distance from the center of diffuser. The relative standard deviation with regard to the mean (320 ft/min or 1.63 m/s) was only 1.4%, thus the diffuser velocity profile can be considered symmetric.

7.2.5 Flow field simulation setup

The main dimensions of the three-dimensional chamber model are listed in TABLE 7.2.1. The other components, including two UV lamps, two humidifiers, and a vacuum pump were modeled as simple blocks with dimensions roughly containing their physical bodies to save simulation time and storage space.

As in the benchmark tests, two meshes were created to check grid independence. The original mesh had 80779 nodes and 446062 tetrahedra elements, and the fine mesh had 156184 nodes and

873448 tetrahedra elements. Each mesh was refined at necessary locations where large gradients were expected or small surfaces were created. To ensure good simulation accuracy, mesh quality was strictly controlled according to the CFX mesh quality requirements on skewness, orthogonality, aspect ratio, and expansion factor (ANSYS 2010). The CFD model and the original mesh are shown in FIGURE 7.2.11.

TABLE 7.2.1 Main dimensions of the three-dimensional CFD model.

Item	Dimensions [m]
Chamber	1.950 (width) by 1.950 (depth) by 1.450 (height)
Round supply diffuser	0.254 (diameter) by 0.024 (height)
Square return grille	0.279 (side length)
Ceiling recessed light	0.127 (diameter)
Pump exhaust	0.024 (diameter)
Pump make-up	0.050 (diameter)
Aerosol injection and sampling tubes	0.013 (diameter) by 0.010 (length)

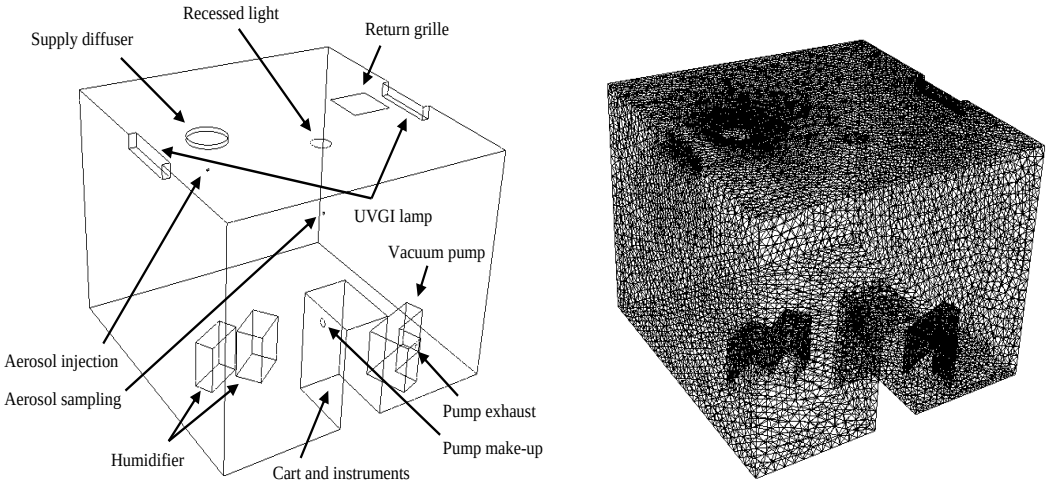

FIGURE 7.2.11 Perspective view of the three-dimensional CFD model (left) and its original mesh (right).

To be more accurate with non-isothermal flow simulation, a table of air properties at standard pressure was imported for interpolation. A simplified version is shown in TABLE 7.2.2. Absorption of radiation energy from the lamps by air was neglected.

TABLE 7.2.2 Air property table used for the non-isothermal simulation (cutted version).

Temperature T [˚C]	-50	0	40	80	120	160	200
Heat capacity c_p [kJ/kg/K]	1.005	1.005	1.005	1.009	1.013	1.017	1.026
Heat conductivity k [W/m/K]	0.020	0.024	0.027	0.030	0.033	0.036	0.039
Density ρ [kg/m^3]	1.534	1.293	1.127	1.000	0.898	0.815	0.746
Dynamic viscosity μ [kg/m/s]	1.46e-5	1.72e-5	1.91e-5	2.09e-5	2.27e-5	2.43e-5	2.58e-5

TABLE 7.2.3 Boundary conditions for flow field simulation.

Boundary location (boundary type)	Conditions
Round supply diffuser (inlet)	Normal speed = 1.26 m/s Turbulence intensity = 5% (medium) Temperature = 21.7 ˚C
Square return grille (outlet)	Average static pressure = -25 Pa
Aerosol injection (inlet)	Normal speed = 1.07 m/s Temperature = 20.2 ˚C
Aerosol sampling (outlet)	Normal speed = 3.55 m/s
Pump exhaust (inlet)	Normal speed = 1.49 m/s Temperature = 73.8 ˚C
Pump make-up (outlet)	Normal speed = 0.10 m/s
Pump surfaces (wall)	Temperature = 73.8 ˚C
Recessed light diffuser (wall)	Temperature = 34.7 ˚C
Supply diffuser side UVGI lamp (wall)	Temperature = 32.0 ˚C
Return grille side UVGI lamp (wall)	Temperature = 41.4 ˚C
Chamber walls and floor (wall)	Temperature = 21.1 ˚C
Other surfaces (wall)	Adiabatic

The boundary conditions in the model were the same as those used in the UVGI viral aerosol tests. Temperatures were measured with thermocouples and a hygrometer, and flow rates were measured with mass flow meters. The measuring equipment has been introduced in Chapter 2. The measurements were either taken by the data logging system during the tests, or conducted separately such as the pump surface temperature and the injection flow rate. The square return grille was not modeled in detail, as its effect on the flow field in the chamber could be neglected. The detailed boundary conditions are listed in TABLE 7.2.3. The no-slip condition was applied to

all wall boundaries. The chamber walls and floor temperatures were set to the same value, because the thermocouples at these locations showed similar readings throughout the tests.

Due to flow fluctuation caused by buoyant flow, difficulty in convergence was expected using steady state simulation as in the second benchmark test. Therefore, a transient simulation was conducted instead to facilitate convergence. For time step control, the whole simulation was defined by two parts. The first part (flow field) used a greater time step size to make the simulation quickly reach steady state, and in the second part, a smaller time step was used to reduce residuals for convergence and for particle tracking. The time step size for the first part was 1 second, and the total simulation time was at least 1000 s (greater than 15 min). The time step size for the second part was 0.5 second. In both parts, 5 coefficient iterations were performed for each time step. The coefficient iterations made the coefficients in the simulation equations more accurate before the flow field marched to the next time step, keeping the residuals low to facilitate convergence.

The turbulence model was the RNG k-ε model, as it was proven to be more suitable for the current study than the standard k-ε or the SST model in both the benchmark tests and some previous studies. High resolution discretization scheme was used to reduce numerical diffusion throughout the simulation (Emvin 1996). In short, the high resolution setting is an automatic blend of first-order and second-order schemes to achieve the balance between performance and accuracy (ANSYS 2010). The high resolution setting was also used for simulating turbulence, but no significant difference was found between this and the first order setting. For convergence criteria, 1e-5 was used for the RMS residuals in momentum, continuity, and energy equations. Additionally, a conservation target of 1% was set for momentum, continuity, and energy equations to ensure global balances in the converged results. In order to further improve simulation accuracy, the CFX double precision solver was used to run the simulation (ANSYS 2010).

7.2.6 Flow field simulation result

The results of the original mesh and the fine mesh were first compared to check grid-independence. Since transient simulation was performed separately using each mesh, and the

results were oscillating even after convergence, the comparison should be made at different time steps, rather than at any specific time point.

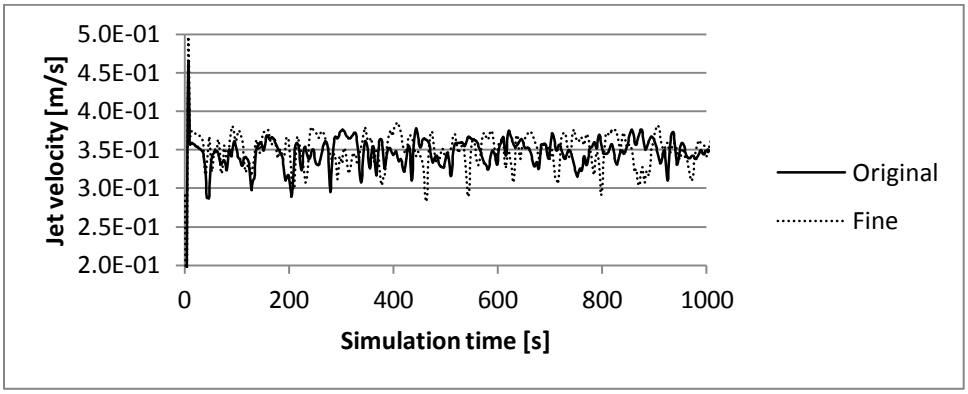

FIGURE 7.2.12 Comparison of the jet velocities at 0.635 m from the center of supply diffuser for the two meshes.

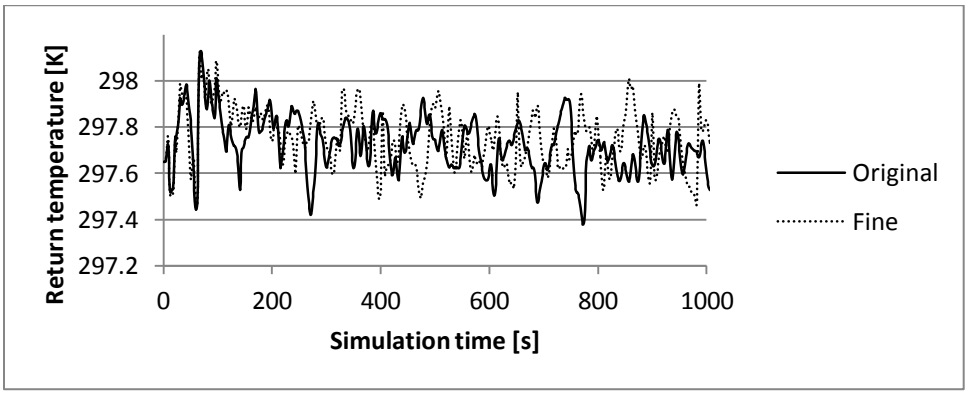

FIGURE 7.2.13 Comparison of the return air temperatures for the two meshes.

The jet velocities at 0.635 m from the center of the supply diffuser toward the return grille were first compared (FIGURE 7.2.12). Both meshes gave similar results, which were about 0.33 m/s, very close to the measurement shown as the last data point in FIGURE 7.2.10. Since the jet velocity primarily depended on the inlet boundary condition, the values were stable from the start of simulation. For the return air temperature (FIGURE 7.2.13), both meshes gave steady state values around 297.7 K (24.5 ˚C), which are very close to the measurement by the return air hygrometer during the tests. An additional transport equation, in a form similar to EQUATION 7.2.3, was also solved for the ratio of aerosol concentration at the sampling location over that at

the injection location. To solve this quantity, a unit concentration was set at the injection boundary, and the kinematic diffusivity of 1.74e-11 m^2/s^2 was set for the transport equation for 1.5 μm particles. In FIGURE 7.2.14, both meshes gave similar steady state values that were about 0.6%, suggesting that about 0.6% of the injected 1.5 μm aerosol was present at the sampling location at steady state. Overall, the original and fine meshes gave similar results that agree with the experiment.

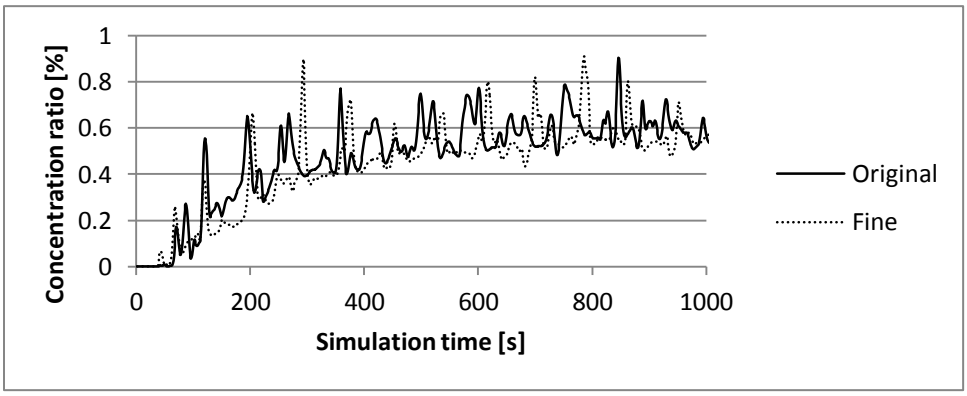

FIGURE 7.2.14 Comparison of the ratios of aerosol concentration at the sampling location over that at the injection location for 1.5 μm particles for the two meshes.

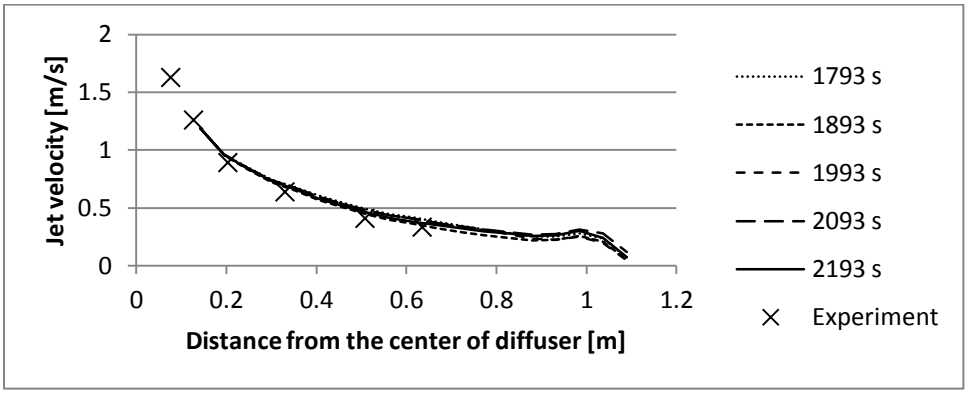

FIGURE 7.2.15 Decay of the diffuser jet by measurement and by simulation at different simulation times with the original mesh.

With the original mesh, the maximum $y+$ was 18.7. Although not small enough to solve flows within boundary layers, the mesh met the requirement for the RNG k-ε turbulence model as $y+$ was much smaller than 200 (He 2005; ANSYS 2010). The flow field calculated using the original mesh was further verified with the diffuser jet decay profile along the jet centerline from the

supply diffuser toward the return grille. Due to small oscillations in the results after convergence, experimental data were compared with simulation results at different time steps (FIGURE 7.2.15). Generally, the measurements were slightly lower than the simulation results. The reason could be errors due to the simulation algorithm, inaccurate input of boundary conditions such as the volumetric flow rate, or the asymmetric velocity profile around the diffuser.

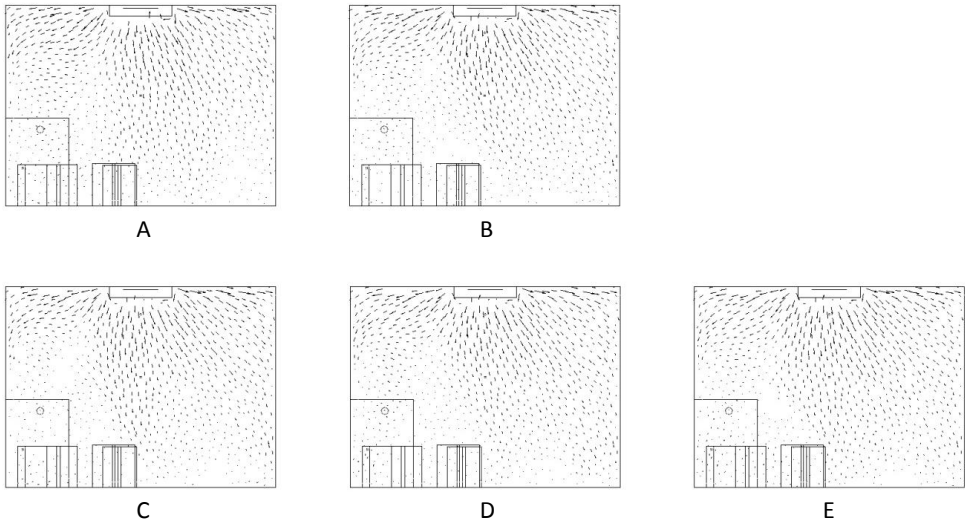

FIGURE 7.2.16 Velocity vectors near the left wall at 1793 s (A), 1893 s (B), 1993 s (C), 2093 s (D), and 2193 s (E) simulation times with the original mesh.

Flow visualization was also conducted using a fogger to verify the flow field near the left wall, the other side of the diffuser with regard to the jet decay measurements. The simulation results at different time steps are shown in FIGURE 7.2.16. Similar to the jet decay profiles, the velocity vectors near the upper part of the left wall did not change significantly over time, as they were very close to the diffuser inlet boundary. For the visualization, the fogger generated fog by injecting steam onto liquid nitrogen. The visualization was focused on the top part of the left wall, where the fog density was the best, and the velocity was relatively high. A group of photos were taken at the rate of 3 frames per second (fps) (FIGURE 7.2.17). The fog could be seen while it was moving downward and being dissipated. Photos were also taken at 5 fps to calculate the velocity more accurately. The visualized flow pattern agreed well with the simulation results, and both velocity magnitudes were about 0.2 m/s in the region just below the UVGI lamp.

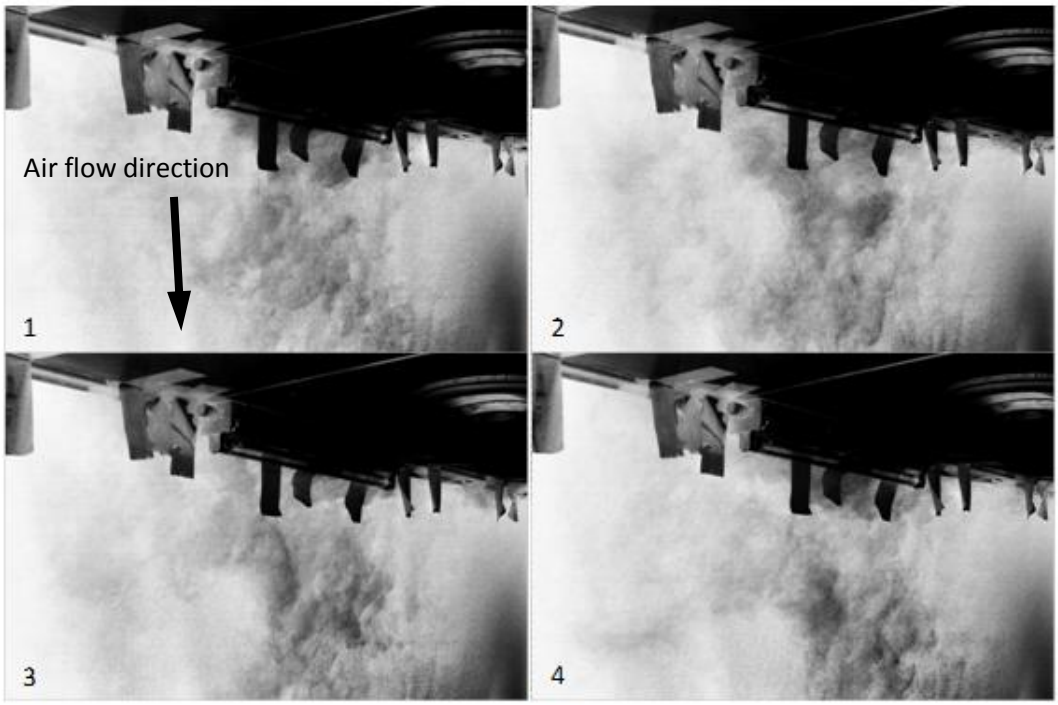

FIGURE 7.2.17 Flow visualization near the left wall and the supply diffuser with the frame sequence from 1 to 4 recorded at 3 frames per second. Photos were converted to negative in grayscale.

The flow field results at the center plane of the chamber which includes the injection and the sampling points are shown in FIGURES 7.2.18-7.2.20. The results were obtained with the original mesh at 2193 s time step. The diffuser jet is obvious along the ceiling in the velocity plots, and the maximum velocity of 3.55 m/s is at the sampling location. For TKE, higher values were generally associated with higher velocities close to the regions of diffuser jet, return air grille, injection outlet, and sampling inlet. From the temperature distribution, the wall temperature was lower than the bulk air temperature, which was generally isothermal. Due to the thermophoresis effect, this temperature difference could enhance aerosol deposition onto the chamber walls, but the effect should not affect the relative recovery or survival of the test viruses as their physical losses were measured.

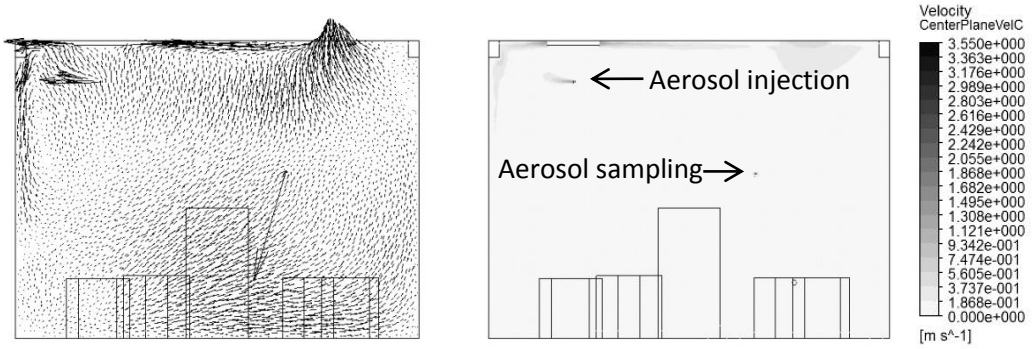

FIGURE 7.2.18 Velocity vectors (left) and velocity contours (right) at the chamber center plane using the original mesh at 2193 s time step.

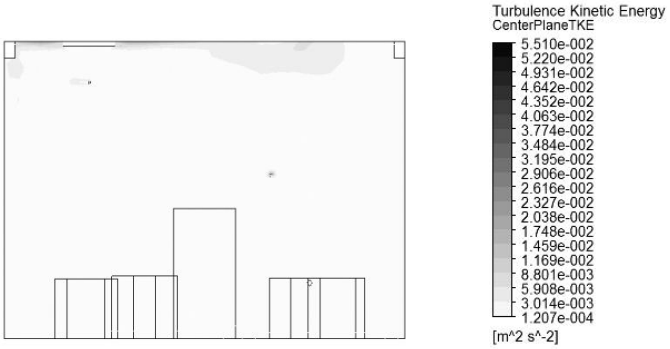

FIGURE 7.2.19 Turbulence kinetic energy contours at the chamber center plane using the original mesh at 2193 s time step.

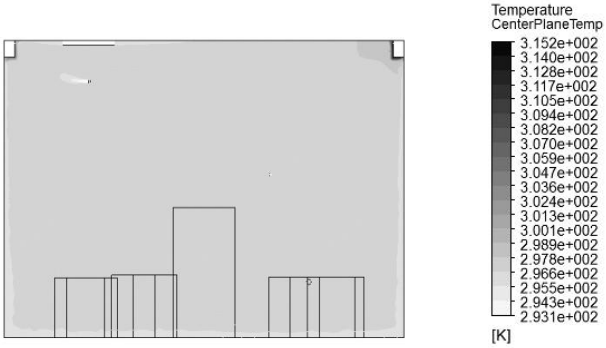

FIGURE 7.2.20 Temperature contours at the chamber center plane using the original mesh at 2193 s time step.

7.3 Particle tracking

7.3.1 Simulation parameters

Particle trajectories were calculated in the Lagrangian framework. Since impactor stage 5 collected the largest amount of particles (more than 40%) by mass, trajectories were calculated for monodispersed particles with an aerodynamic diameter of 1.5 μm, which was the geometric mean diameter of this impactor stage. Both gravitational settling and Brownian motion were neglected for this particle size (Hinds 1999; Gao 2007). By definition, the drag force (F_D) on a spherical particle is:

$$F_D = \frac{1}{2} C_D \rho_f A_p U_{fp}^2, \tag{7.3.1}$$

where C_D is the drag coefficient, ρ_f is the fluid density, A_p is the cross-sectional area of the spherical particle, and U_{fp} is the relative velocity between fluid and particle. In CFX, C_D is calculated using the Schiller-Naumann model:

$$C_D = \frac{24}{Re}(1 + 0.15Re^{0.687}), \tag{7.3.2}$$

which has been reported to be accurate (<10% error) for the particle Reynolds number smaller than 1000 (Hinds 1999). It approaches the Stokes model (C_D=24/Re) as Reynolds number decreases. If particle density is assumed to be the same as water density, the particle Reynolds number for the selected particle size is about $0.1U_{fp}$. According to the simulated velocity field, the maximum particle Reynolds number was about 0.1. Thus the Schiller-Naumman model could give an accurate estimation of the drag coefficient. However, CFX does not include the Cunningham slip correction factor in the particle momentum equation. Since the factor is about 1.10 for 1.5 μm particles, the calculated drag force is about 10% greater than the actual value. This offset is equivalent to simulating particles slightly larger than 1.5 μm, and was assumed not to significantly affect the trajectory results, as the movement of these particles was expected to always follow the instantaneous streamlines due to their short relaxation times (Gao 2007).

Due to the small volumetric fraction of the particles present in the chamber air, their effect on turbulent flow patterns could be neglected. Therefore, a one-way coupling simulation was performed for particle tracking, which made the simulation faster and the convergence easier than the two-way coupling option (Memarzadeh 2000b; Wong 2010). The wall boundaries can be treated as sticky, not sticky, or somewhere in between for the particles contacting them. Previous

studies have shown that whatever selection was used did not affect the final results significantly (Memarzadeh 2000b). Since the particles simulated in this study were very small, the adhesive forces including van der Waals and electrostatic attraction forces exerted on them at the boundaries were considered too large to be overcome, thus the 100% sticky model was applied. For particles small enough (usually smaller than 20 μm), they would instantly (within 1 second) reduce to droplet nuclei which was about half of their original size coming out of the nebulizer (May 1973; Ijaz 1987; Sattar 1987; Weber 2008; Atkinson 2009). Therefore, the particles were assumed to be at equilibrium out of the injection inlet boundary, and thus the evaporation process was not simulated. Instead, a lower temperature was assigned to the nebulizer output in the CFD model to include the evaporation effect. Coagulation of particles was not simulated either, since the particle concentration in the chamber was too low to make its effect significant (Wong 2010).

Since much of the flow field in the chamber was turbulent, aerosol generated from the nebulizer could move nearly anywhere before being collected by the impactor. This resulted in diverse particle trajectories and UVGI doses received. Therefore, a large number of particle trajectories must be calculated to reach statistical stability before further inactivation analysis could be carried out. In the simulation, particle material properties were assumed to be the same as water properties, with a density of 998 kg/m^3 and a heat capacity of 4.18 J/g/K. After the flow field simulation was stabilized and converged, particles were generated uniformly on the injection surface at the rate of 100 particles per second for about 1000 s of simulation time to reach statistical stability.

7.3.2 Particle tracking result

The trajectories of some collected particles are shown in FIGURE 7.3.1. The particles coming out of the injection inlet boundary were firstly entrained in the diffuser jet close to the left UVGI lamp, and then dispersed in the turbulent flow field. Particles may travel to nearly any place in the chamber before being collected. However, a main path seems to exist according to the plotted trajectories and velocity vectors. By this path, particles could travel to the sampling inlet with a shorter residence time than by most other paths.

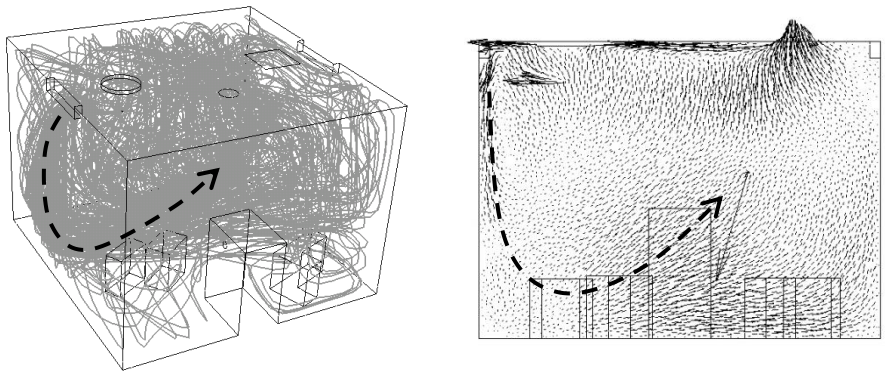

FIGURE 7.3.1 Trajectories of the collected particles (left) and velocity vectors on the chamber center plane (right) with the most likely path marked with dashed lines.

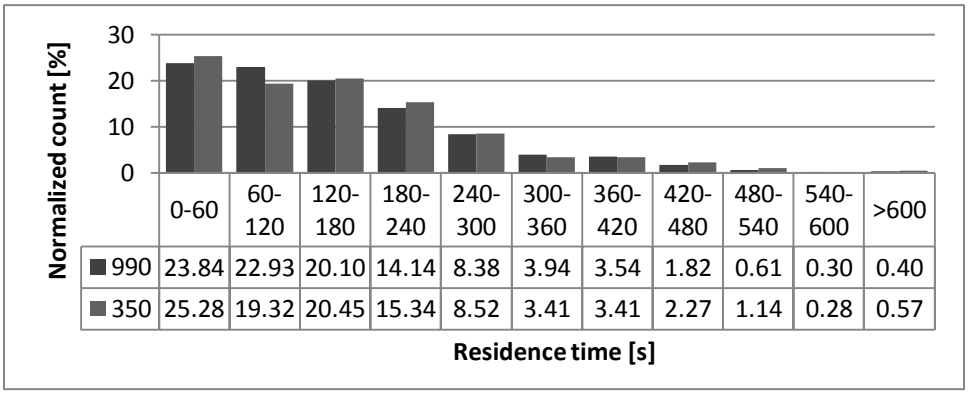

	0-60	60-120	120-180	180-240	240-300	300-360	360-420	420-480	480-540	540-600	>600
990	23.84	22.93	20.10	14.14	8.38	3.94	3.54	1.82	0.61	0.30	0.40
350	25.28	19.32	20.45	15.34	8.52	3.41	3.41	2.27	1.14	0.28	0.57

FIGURE 7.3.2 Histogram of residence time of 350 and 990 sampled particles.

The histogram of residence time from injection to sampling is shown in FIGURE 7.3.2. To test whether statistical stability was reached, simulation was stopped when 350 particles had been collected, and then the simulation was continued until the final 990 particles had been collected. For the first 350 particles, the geometric mean residence time was 115.6 s, and the median was 130.7 s. For the total of 990 particles, the geometric mean residence time was 114.8 s, and the median was 125.8 s. The difference in the geometric mean residence time between the two groups of particles was smaller than 1%. These residence times were also close to the measured residence time which was 126+/-6 s (Appendix II). In the histogram, most particles sampled had the residence times shorter than 60 s, possibly related to the main path shown in FIGURE 7.3.1.

7.4 UVGI simulation

7.4.1 Background

The most frequently used methods for calculating the irradiance from a linear emitter may be the point-source summation (PSS) method and the line-source integration (LSI) method (Blatchley 1997; Noakes2004b; Ducoste 2005; Sozzi 2006). Both methods are based on the inverse square law, by which irradiance is proportional to the inverse of square of the distance away from source. They also assume that irradiance is linearly additive at any point in the field and linearly proportional to the power of the lamp (Summer 1962; Miller 2000). The PSS method treats the light source as many identical points, each of which emits the same amount of energy per unit time. The total irradiance at any location in the field is calculated by summing the contribution of each source point. In order to achieve good accuracy, a large number of points are needed, but as the number grows, the requirement for computational power also grows. To overcome this, its continuous version, the LSI method was developed. However, both methods tend to over predict irradiance in the near field of a source, although this may not be a problem for most HVAC applications (Blatchley 1997; Sozzi 2006).

Another method used to calculate irradiance is the Monte-Carlo method, which tracks a great number of energy bundles (or photon packs) through a series of events in which each bundle may be scattered or reflected until being absorbed or a predefined distance has been reached. The Monte-Carlo method makes the description of a complex problem conceptually simple, thus it is great for the problems which cannot be solved analytically. However, computing time for convergence is known to be a major drawback (Patterson 1991; Rogers 1995). Since the Monte Carlo method relies on random numbers and probability distribution functions, statistical stability must be achieved to get meaningful results. On the other hand, the accuracy of results increases with the number of tests (bundles or trajectories) by the Law of Large Numbers. With the advancement of computer technology, this obstacle has become less formidable, and the Monte Carlo method would become more and more popular for a wider range of applications.

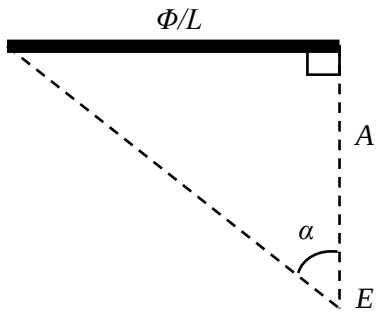

FIGURE 7.4.1 Illustration of the parameters in EQUATION 7.4.1 for calculating the irradiance contributed by the linear light source on one side of the point of interest.

Empirical equations based on the inverse square law have also been used to roughly simulate irradiation from a linear emitter (Beggs 2000; ASHRAE 2008). Because it was easy to be integrated into the CFD program, the current simulation used one of these equations provided in the ASHRAE Handbook (ASHRAE 2008):

$$E = \frac{\Phi}{L} \cdot \frac{2\alpha + sin\,(2\alpha)}{4\pi^2 A}, \tag{7.4.1}$$

where E [W/cm^2] is the UVC irradiance contributed by the part of lamp on one side of the point being calculated, Φ [W] is the emitter's output power, L [cm] is the emitter's effective length, A [cm] is the perpendicular distance from the point to the linear emitter, and α [rad] is the view angle from the point (FIGURE 7.4.1). For the UVGI lamps used in the current study, Φ was 6.9 W, and L was 17 in (43 cm).

Several assumptions were made or tested to apply EQUATION 7.4.1:

1. The UVGI transmission was not affected by air molecules (N_2, O_2, CO_2, and H_2O) for the short transmission distances in the chamber. This can be proven based on the absorption spectra and small polarizabilities of the molecules for Rayleigh scattering (Tarafdar 1969; Huffman 1992; Ultraviolet radiation guide 1992).
2. The irradiation was not weakened by fog or smoke generated by the humidifiers and vacuum pump (Miller 2000). By measurement with a radiometer (Solarmeter Model 8.0, Solartech, Inc., MD), up to 30% reduction of irradiation was found in a very small region close to the humidifier outlets, where most particles would travel through in a very short time if they ever arrived at the region. Additionally, humidifiers were not running for the most part of the UVGI tests.

3. The reflection of 253.7 nm UVC light on the chamber interior surfaces was neglected. It has been reported that the type of paint might be a significant factor (Thurston-Enriquez 2003). The paint used for the chamber interior was a semi-gloss acrylic latex white paint for exterior use (BEHR Premium Plus Ultra). Its main ingredients were acrylic polymer, titanium dioxide, and water. The reflectance of about 5% has been reported for this type of paint (Blatchley 1997; Kowalski 2009; Uemoto 2010). In an experiment, no reflection was detected when pointing a radiometer in a direction away from the UVGI lamp. The UVC light hitting the acrylic door was considered to be 100% absorbed as well (Laube 2004).

Even if the above assumptions are valid, errors could still exist due to the empirical equation itself or the reduced lamp output which might be caused by the actual operation hours, conditions, and fouling of the lamp surfaces. Therefore, a correction factor *C* was added to EQUATION 7.4.1 for this study:

$$E = C(A) \cdot \frac{\Phi}{L} \cdot \frac{2\alpha + sin\,(2\alpha)}{4\pi^2 A}. \tag{7.4.2}$$

The correction factor was determined based on measurements made at different distances from the lamp at the test conditions (FIGURE 7.4.2). The measurements were taken for each lamp individually with a radiometer after a 30 min warm-up period. Both lamps showed similar outputs as expected. The discrete correction factors were first obtained by comparing the irradiances calculated with EQUATION 7.4.1 and those experimentally measured. They were then curve fitted for the continuous function. With R^2 of 0.95, the correction factor function becomes:

$$C(A) = 0.862 - 0.815e^{-\frac{A}{16.55}}. \tag{7.4.3}$$

The irradiance curves based on the original equation (EQUATION 7.4.1), the corrected equation (EQUATION 7.4.2), and the experimental data are compared in FIGURE 7.4.2. From the comparison, it can be seen that the original equation led to overestimation for the near field similar to the PSS and LSI methods. The overestimation might be tolerable for common HVAC applications, as it was only significant within about 20 cm from the UVGI lamp. However, for the current study, as the aerosol could get very close to the UVGI lamps, the accuracy for the near field became important.

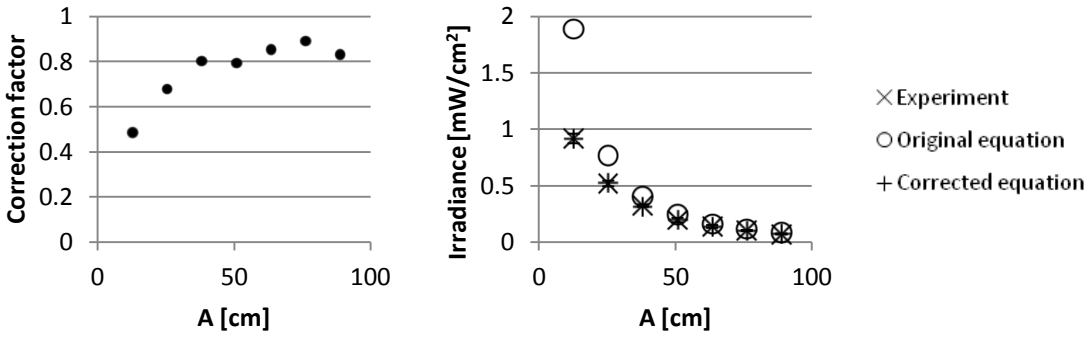

FIGURE 7.4.2 Correction factor *C* (left) and irradiance *E* (right) versus the distance *A* from a UVGI lamp. The original equation (EQUATION 7.4.1), corrected equation (EQUATION 7.4.2), and experimental measurement (error bars for standard deviation) are compared for irradiance.

7.4.2 UVGI field in the chamber

The corrected UVGI equation was integrated into the CFD simulation via additional user defined variables and equations to calculate the UVGI field in the chamber. The UVGI field was calculated as if the chamber were empty without any equipment inside even though they were modeled for the flow field simulations. As a result, irradiance was over predicted in the blind spots where the UVC light was actually blocked by the equipment. This simplification should not affect the final UVGI dose result significantly, since the affected regions were generally close to the floor, where the irradiance was already weak, and the time spent by particles was relatively short as can be seen from the trajectories shown in FIGURE 7.3.1. Contour plots of irradiance in the chamber are shown in FIGURE 7.4.3, from which, the four corners near the ceiling received the lowest irradiance, given that the blind spots on the floor were not considered.

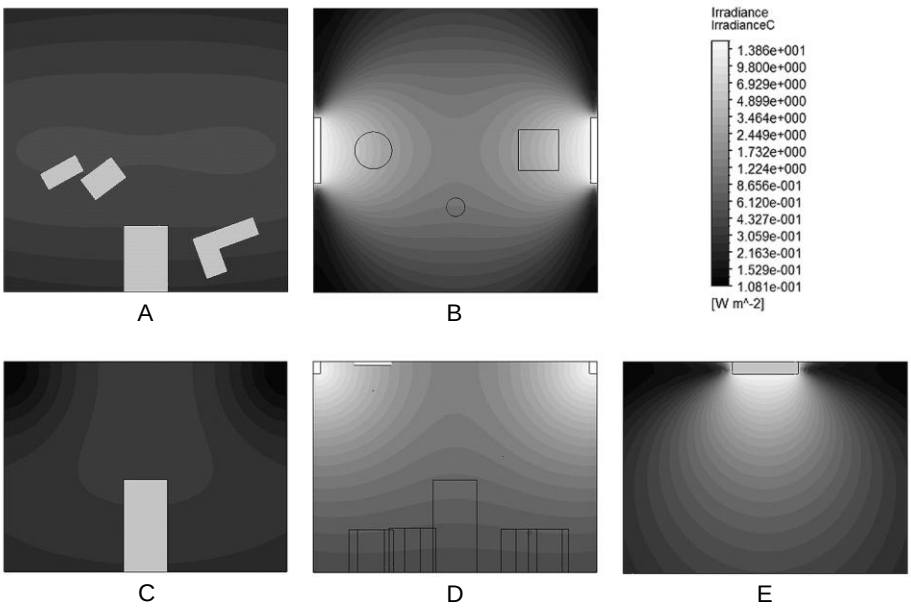

FIGURE 7.4.3 Contour plots of UVGI irradiance on the chamber interior planes at floor (A), ceiling (B), front wall (C), center plane (D), and left wall (E).

7.5 Dose distribution and viral aerosol inactivation

UVGI dose received by each tracked particle was consequently obtained by integrating the UVGI irradiance along the particle's trajectory. FIGURE 7.5.1 shows a histogram of the dose received by the collected particles. For the first 350 particles, the geometric mean was 11.5 mJ/cm^2, and the median was 12.4 mJ/cm^2. For the total of 990 particles, the geometric mean was 11.4 mJ/cm^2, and the median was 11.8 mJ/cm^2. The difference in the geometric mean dose received by the two groups of particles was below 1%.

Virus susceptibility could now be solved with the dose histogram and an inactivation model. Virus inactivation by UVGI can be assumed to be exponential, similar to other microorganism inactivation processes (Hollander 1943; Koch 1966; Shimojo 1971; Riley 1989; Mbithi 1991; Beggs 2002a, 2002b; Whiting 1991; Memarzadeh 2000a, 2004; Nuanualsuwan 2002; Noakes 2004a, 2004b, 2006; Ducoste 2005; Ko 2005; Tseng 2005b; Hijnen 2006; Sozzi 2006; McDevitt 2010; Piercy 2010). The inactivation rate due to UVGI directly depends on the UVGI dose received by the microorganism:

$$Inactivation\ rate\ due\ to\ UVGI = 1 - \frac{C_{UVGI}}{C_0}, \tag{7.5.1}$$

$$C_{UVGI} = C_0 \sum_i (R_i e^{-ZD_i}), \tag{7.5.2}$$

where for the virus that received dose D_i (mJ/cm^2), C_{UVGI} is the live virus titer with UVGI, C_0 is the live virus titer if UVGI were not present, R_i is the proportion of collected virus that received dose D_i, and Z (cm^2/mJ) is the virus susceptibility to UVGI. The Z value in EQUATION 7.5.2 has been discussed in detail in several publications (Riley 1976; Peccia 2001a, 2004; Beggs 2002b; Xu 2003). It depends on several factors including virus type, strain, suspension medium, and humidity. The greater the Z value, the more susceptible the microorganism is. In this study, the live virus titers were substituted with relative recoveries to account for the differences in nebulizer fluid concentration and physical loss between different tests:

$$\frac{RR\ with\ UVGI}{RR\ without\ UVGI} = \sum_i (R_i e^{-ZD_i}). \tag{7.5.3}$$

Because the total virus measurement was affected by UVGI as discussed in Chapter 6, the measured survival could not be used here. The dose (D) that a particle received can be calculated using the following equation:

$$D = \Delta t \sum E, \tag{7.5.4}$$

where Δt is the time step size, and E is the irradiance the particle received at a time step.

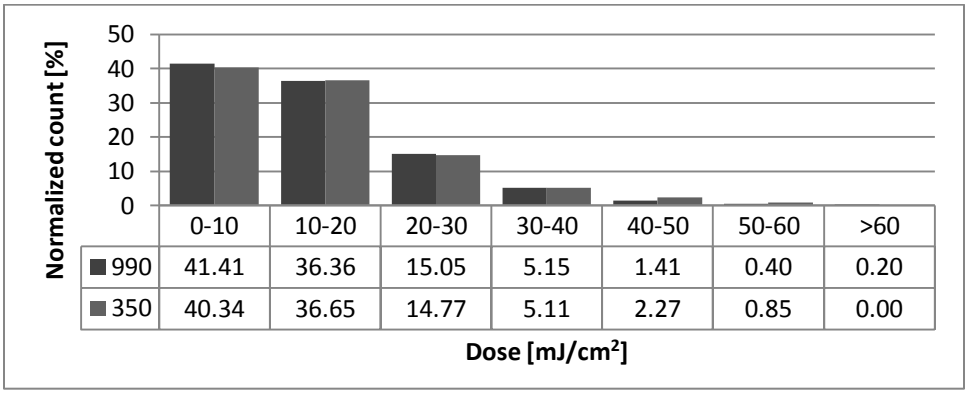

	0-10	10-20	20-30	30-40	40-50	50-60	>60
990	41.41	36.36	15.05	5.15	1.41	0.40	0.20
350	40.34	36.65	14.77	5.11	2.27	0.85	0.00

FIGURE 7.5.1 Histogram of dose received by 350 and 990 sampled particles.

The simple exponential (or log-linear) model has shown inaccuracy in the low and high inactivation regions. A more complete model contains a shoulder before the log-linear region and a tail after it (FIGURE 7.5.2). In most cases the shoulder is not significant, unless the dose received is sub-lethal and a reactivation mechanism exists (Casarett 1968; Cerf 1977; Munakata

1991; Pruitt 1993; Kowalski 2001; Beggs 2002a). When the regression line intercepts the y-axis above unity, it shows strong evidence that the shoulder effect is significant, and it could be due to either low irradiation levels or high resistance of the microorganism (Kowalski 2001; Thurston-Enriquez 2003). For the most resistant virus in this study, no shoulder effect was found for HAdV-1 in previous studies (Nuanualsuwan 2002; Nwachuku 2005; Hijnen 2006).

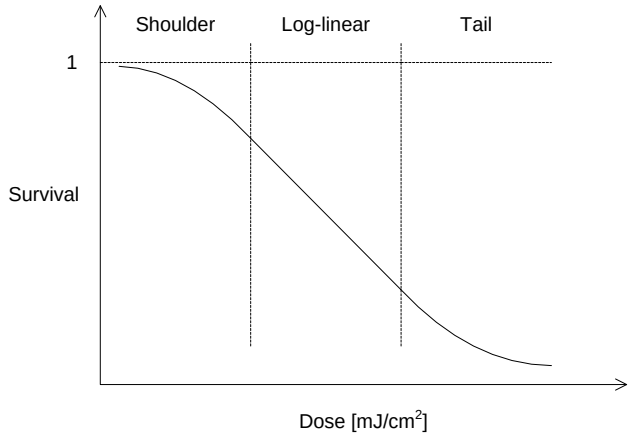

FIGURE 7.5.2 A typical curve for microorganism inactivation by UVGI, including shoulder, log-linear, and tail regions.

After the log-linear region, the inactivation rate decreases, forming the tail region (Xu 2003; Blatchley 2007; Memarzadeh 2010). The tail usually happens above 99% inactivation, and is more obvious for more susceptible microorganisms, and thus is not likely to be observed for resistant species like adenoviruses and MS2 (Qualls 1983; Smerage 1993; Hijnen 2006). It is probably due to the more resistant population of the microorganism or the shielding effect (Moats 1971; Riley 1972; Cerf 1977; Davidovich 1991; Whiting 1991; Fujikawa 1996; Kowalski 2000, 2001; Beggs 2002a; Pennell 2008).

Not many data exist for viral aerosol inactivation by UVGI, but more data are available for inactivation in water (or other liquid suspensions). Virus in the airborne state is usually more vulnerable to UVGI than in the waterborne state, thus the susceptibility based on water tests could be used as conservative estimates for air disinfection purposes (Kowalski 2009). Due to test uncertainties and different test conditions, the differences in obtained virus susceptibilities to UVGI are large between studies. For MS2, the Z-values based on an aerosol test were 0.38-0.48

cm^2/mJ (Walker 2007), but another study showed much greater susceptibilities up to 8.1 cm^2/mJ (Tseng 2005b; Kowalski 2009). In liquid environments, they are generally 0.03-0.17 cm^2/mJ (Meng 1996; Nuanualsuwan 2002; Thurston-Enriquez 2003; Ko 2005; Nwachuku 2005; Hijnen 2006; Kowalski 2009). For HAdV-1, its Z-values were 0.39-0.68 cm^2/mJ in aerosol form and 0.03-0.08 cm^2/mJ in liquid (Nwachuku 2005; Kowalski 2009). For AIV, the Z-values were 1.06-1.19 cm^2/mJ in aerosol and 0.48-1.38 in liquid (Kowalski 2009).

Since only one inactivation rate was obtained for each virus in the experiment, the only inactivation model applicable was the simple log-linear model ignoring the shoulder and tail regions. This model should be appropriate for the viruses in this study, as their inactivation rates were less than 1-log, and the self-repairing or photoreactivation mechanism was not available to them. Using this inactivation model, the Z-value for each of the three viruses was calculated and is shown in TABLE 7.5.1, in which, MS2 is similar to HAdV-1, and is more resistant than AIV by mean value. The susceptibilities obtained in the current study are close to the published data for liquids, showing that as long as UVGI photons could reach the nucleic acid, their germicidal effect may not depend on the outside environment of the virus.

TABLE 7.5.1 Z-values (susceptibilities) of MS2, HAdV-1, and AIV based on experimental inactivation rate, simulated dose histogram, and log-linear kinetics.

Virus	Survival [range of one standard error]	Z-value [range of one standard error] [cm^2/mJ]
MS2	0.502 [0.339, 0.743]	0.057 [0.022, 0.098]
HAdV-1	0.507 [0.403, 0.639]	0.056 [0.035, 0.079]
AIV	0.255 [0.097, 0.669]	0.132 [0.031, 0.278]

Compared with the published viral aerosol data, however, the virus susceptibilities to UVGI in the current study are about one order of magnitude lower. One possible reason could be the difference in test facility between the past and the current studies. All the referenced tests were conducted in tunnel-like single-pass facilities with the exposure times of only a few seconds, much shorter than the 2 min residence time in the current study. Another important difference is that the past studies directly compared live virus titers with and without UVGI, without correcting for different nebulization rates and physical losses of the test viruses between tests. Additionally, as the test data for viral aerosols are very rare, actual susceptibilities of airborne viruses have not been determined, and the effects of factors including RH and suspension medium have not been

fully tested. The difference between the current result and the published viral aerosol data could be due to these factors as well.

For the uncertainties in the current study, one major contributor could be the uncertainty associated with live virus titration. Secondly, the corrected irradiance equation might still be inaccurate for locations very close to the UVGI lamps, since the measurement closest to the lamp was taken at about 13 cm, but the closest point the particles traveled to was only about 4 cm from the lamp. Finally, the simplification made in the UVGI field calculation by ignoring all the instruments in the chamber could also lead to slightly overestimated doses received by some of the tracked particles.

For future work, tests at different UVGI dose levels are recommended to study different inactivation models and the effects of shoulder and tail. It would also help reduce the uncertainty of the calculated virus susceptibility. Tseng 2005b tested inactivation of viral aerosol by UVGI for the irradiance range of 0.06-0.24 mW/cm^2, and found that irradiance did not significantly affect virus inactivation rate as long as the UVGI dose was constant. In this study, the range of irradiance in the chamber spanned two orders of magnitude from about 0.01 to 1.30 mW/cm^2, which was much broader than the range tested by Tseng 2005b. This raises the question again whether irradiance could be a significant factor for virus inactivation by UVGI. If irradiance plays a significant role, the current inactivation kinetics relying only on UVGI dose received would be inaccurate. In order to better study all the above aspects, viral aerosol tests should be carried out in a specially designed facility with strictly controlled irradiance for lower uncertainty and higher accuracy, such as the one that has been used in Tseng 2005b.

7.6 Conclusions

In this chapter, the transient flow field in the chamber was simulated using CFX. After steady state and convergence were reached, particle tracking in the Lagrangian frame was conducted. To reach statistical stability, 990 particles were collected by the impactor in the simulation. The UVGI field in the chamber was calculated using an empirical equation corrected according to experimental data. The dose received by each particle was then calculated by integrating

irradiance along its trajectory. Finally, virus susceptibility was obtained by assuming a log-linear inactivation model.

The average susceptibility of MS2 was 0.057 cm^2/mJ with the range for one standard error of [0.022, 0.098] cm^2/mJ. For HAdV-1, the susceptibility was 0.056 [0.035, 0.079] cm^2/mJ, and for AIV, it was 0.132 [0.031, 0.278] cm^2/mJ. The results are close to the published data for liquids, and about one order of magnitude more resistant than aerosol data. This suggests that as long as UVGI photons reach the nucleic acid, their germicidal effect may not depend on the outside environment of virus. The difference from the published aerosol data was most likely caused by the differences in test facility and procedure. However, measurement uncertainties and the simplifications made for simulation may also have affected the accuracy of the current results.

Until now, virus inactivation by UVGI was mostly studied as a function of UVGI dose, but whether irradiance could significantly affect inactivation for the same dose is not clear yet. If virus inactivation is affected when irradiance is very low or very high, like what might have happened in the current tests, virus susceptibility to UVGI may not be determined accurately with dose alone. However, tests of viral aerosol inactivation by UVGI at different dose levels are also recommended to study the inactivation kinetics including the shoulder and tail regions. Overall, data for viral aerosol inactivation by UVGI are still very rare, and more tests in specially designed facilities with improved uncertainty and accuracy are recommended to test all the aspects mentioned above, and for further development of the numerical model.

8 Filtration of viral aerosols by HVAC filters

8.1 Introduction

HVAC filters are commonly used in hospitals, airplanes, animal barns, and other buildings to keep the internal air clean, and reduce infection (Hopkins 1971; Moser 1979; Olsen 2003; Dee 2006; Yang 2011). HVAC filters especially with the minimum efficiency reporting value (MERV) smaller than 14 are significantly less efficient than the high-efficiency particulate air (HEPA) filters or the ultra-low penetration air (ULPA) filters, but are more economical due to lower pressure drops (Dee 2006; Farnsworth 2006). Their filtration efficiencies can be improved with ionization (Huang 2008). Germicidal capability can also be gained from chemical coatings.

Particles going through fibrous filter elements may be caught by one of five mechanisms: interception, impaction, diffusion, gravitational settling, and electrostatic attraction. The relative importance of these mechanisms depends on particle size and filter face velocity. Generally, diffusion is important for particles smaller than 0.1 μm, while impaction and interception are important for particles greater than 0.5 μm. Between the two sizes, no mechanism is dominant, and the overall filtration efficiency tends to be lower (Hinds 1999; Verreault 2008). A filter's filtration efficiency (η_i) can be calculated as:

$$\eta_i = (1 - P_i) \times 100\% = \left(1 - \frac{C_{di}}{C_{ui}}\right) \times 100\%, \tag{8.1.1}$$

where the subscript *i* stands for a specific size range, *P* is the penetration, *C* is the concentration of the live virus, total virus, or fluorescein, and its subscript *di* or *ui* stands for downstream or upstream location of the filter.

Air filtration has been well studied for HVAC filters using solid particles. Standards are also available for tests and applications. However, the filtration behavior of airborne microorganisms has not been thoroughly studied. Past studies have suggested that it is the physical properties (shape, size, density), rather than the biological properties (viability, chemical composition) that influence the behavior of particles in filtration process. Therefore, filtration efficiencies for

biological particles could be predicted with non-biological particles of similar physical properties (McCullough 1997). If this is true, the currently available test standards and data can be used for microorganisms, and the more time consuming biological aerosol tests would become unnecessary. It is thus the primary goal of the current tests to check whether the filtration efficiency for viruses can be predicted equally well with fluorescein or particle counters.

8.2 Test method

MS2, HAdV-1, and AIV were tested with two square chemical-free pleated HVAC filters (Accumulair brand) of MERV 8 and 13, which are commonly used in HVAC systems. The dimensions of the test filters were 9.50 in (24.1 cm) for side length and 1.75 in (4.4 cm) for thickness. To test the HVAC filters in the chamber, a test duct was attached upstream of the return air grille (FIGURE 8.2.1). Identical flexible Tygon tubing of 50 in (127 cm) length was used to connected two identical Andersen impactors with the upstream and downstream sampling probes (0.69 in or 1.8 cm ID, and 0.75 in or 1.9 cm OD) which were mounted horizontally, or perpendicular to air flow. The anisokinetic sampling efficiency of each sampling probe was estimated to be greater than 80% for impactor stages 3-7 (0.4-4.7 μm), greater than 90% for impactor stages 4-7 (0.4-3.3 μm), and greater than 95% for impactor stage 5 (1.1-2.1 μm) which collected the largest amount of aerosol by mass (Appendix I). Since the sampling efficiency depended on particle size, the anisokinetic sampling shifted the particle size distribution curve toward smaller sizes. However, if the upstream and downstream sampling efficiencies are identical, the anisokinetic sampling should not affect the filtration efficiency results.

As shown in FIGURE 8.2.2, the filter duct had two sections. Each section was 6 in (15.2 cm) long, and was of square cross-section of 7.75 in (19.7 cm). The test filter was mounted between the two sections, secured with eight C-clamps. The connections between the filter and the duct were caulked to prevent air leaking. The upstream and downstream sampling locations were in the center of each section, or 3 in (7.6 cm) upstream and downstream of the test filter. The percentage scale shown in FIGURE 8.2.2 was used for traverse sampling locations. For viral aerosol tests, the sampling locations were always at 50%, or the center of the duct cross-section. For preliminary tests, other locations were also used.

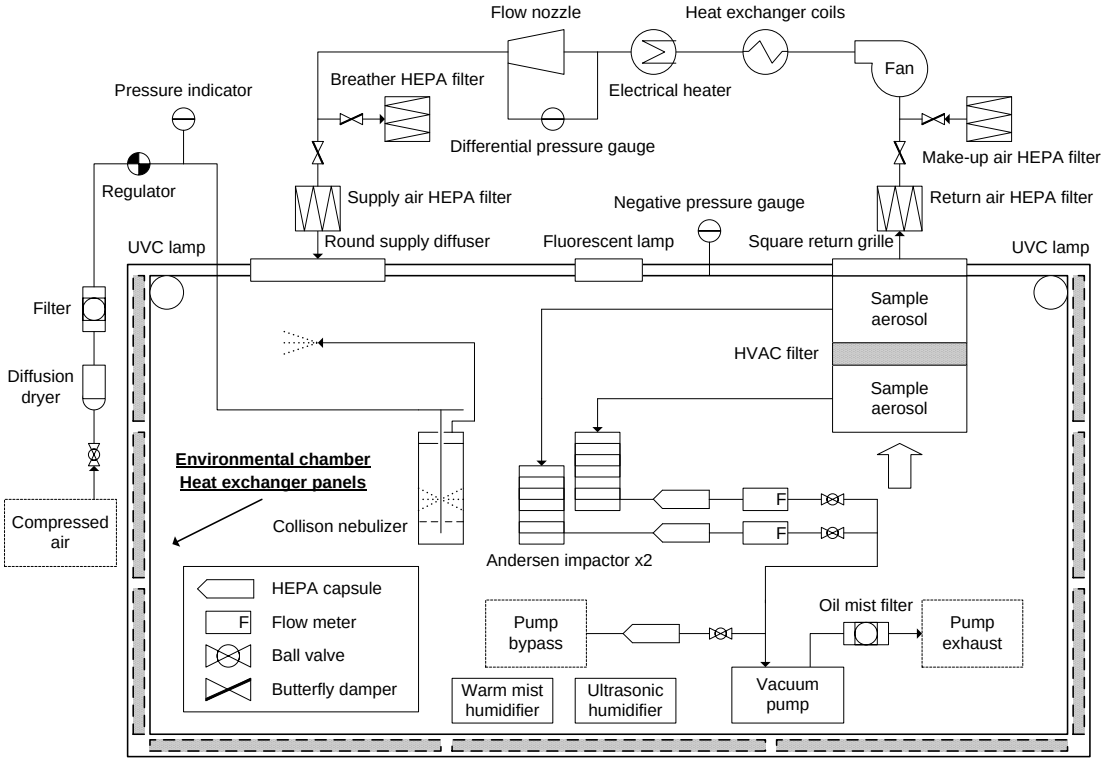

FIGURE 8.2.1 Schematic drawing of the test setup for the HVAC filter tests.

Because of the similarity of upstream and downstream sampling setups, their sampling differences were reduced. However, due to the unavoidable differences between upstream and downstream probes, tubing, impactors, and other components, the measured filtration efficiencies could still drift from their true values. Therefore, correlation tests were conducted following ANSI/ASHRAE 2007 without a filter installed:

$$R = \frac{Downstream\ concentration - Downstream\ background\ concentration}{Upstream\ concentration - Upstream\ background\ concentration}, \tag{8.2.1}$$

where R is the correlation ratio used to correct penetrations:

$$Corrected\ penetration = \frac{Measured\ penetration}{R}. \tag{8.2.2}$$

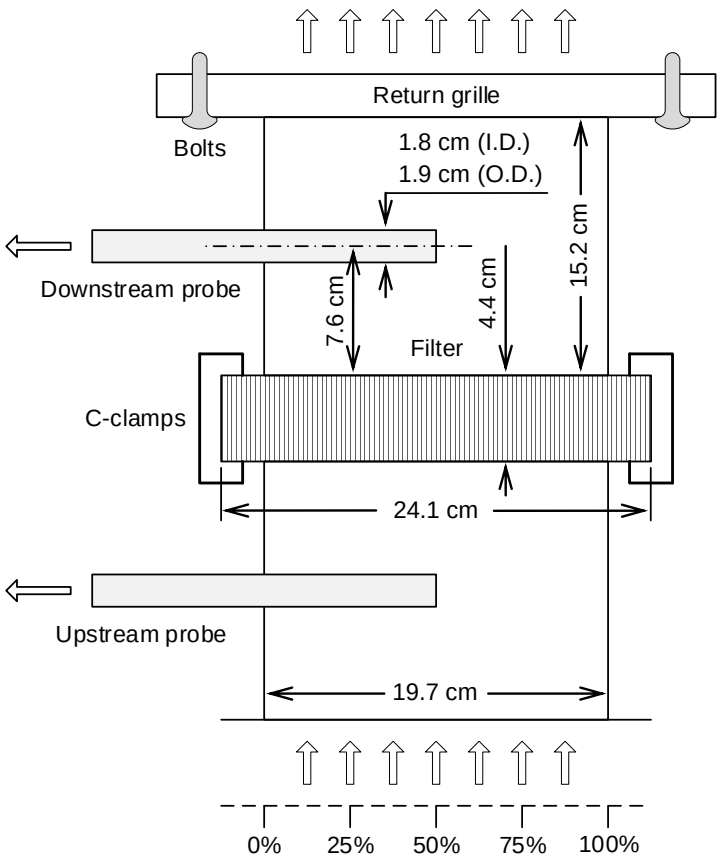

FIGURE 8.2.2 Filter duct schematic with main dimensions showing two identical duct sections and a percentage scale denoting traverse sampling locations.

The HVAC filter tests were conducted at 25 ˚C, 50% RH, and about 140 ft^3/min (3964 l/min) volumetric flow rate. The negative pressure in the chamber at the ventilation rate was about 0.36" water (90 Pa). Unlike viral aerosol survival, filtration efficiency is unlikely to be affected by humidity in the common range (30%-70% RH) (McCullough 1997; Hwang 2012). The nebulizer setup for aerosol generation was the same as the previous tests, and the nebulizer fluid ingredients for each virus were not changed. Each test was conducted for 60 min with aerosol generation at 20 psi (138 kPa) compressed air pressure to ensure high concentrations in the downstream samples. Viral aerosol samples were taken from the upstream and downstream locations simultaneously. Tests were carried out in triplicate and in randomized order for each virus. Statistical analysis and ANOVA were carried out for penetration for impactor stages 3-7 as before.

8.3 Preliminary tests without virus

Several preliminary tests without virus were carried out to characterize and validate the test duct setup before the viral aerosol tests. The preliminary tests include a pressure drop test, a velocity profile test, and a penetration uniformity test. The flow rate for the preliminary tests was the same as in the viral aerosol tests, and was about 140 ft^3/min (3964 l/min). At this flow rate, the average face velocity was about 336 ft/min (1.71 m/s), lower than the filter's designed velocity of 500 ft/min (2.54 m/s). Operating at a lower face velocity would increase the effects of diffusion and electrostatic attraction, while weakening that of inertial impaction. Due to this limitation of the test setup, the actual performance of the test filters may not agree with those from standard test method. However, the filtration efficiencies for viruses, fluorescein and physical particles could still be compared for the primary goal of this group of tests.

The pressure drop of each filter was measured with a differential pressure gauge (Magnehelic, 0-2 cm water range, 0.05 cm water resolution) using the two aerosol sampling openings on the duct. The measured pressure drops were compared with the filter test reports (Blue Heaven Technologies, Louisville, KY) provided by the seller (www.filters-now.com). Since the filters in the test reports were 2 ft (61.0 cm) by 2 ft (61.0 cm), the corresponding flow rate for the same face velocity (336 ft/min or 1.71 m/s) was 1344 ft^3/min (38057 l/min). For the new MERV 8 test filter, the reported pressure drop was about 0.25 cm water, and the measured pressure drop was 0.30 cm water. For the new MERV 13 test filter, both of the reported pressure drop and the measurement were about 0.51 cm water. The agreement shows that the filters were properly installed.

Velocity profiles were measured at both upstream and downstream locations with a hot wire anemometer (Model 8330 VelociCheck, TSI, Inc., Shoreview, MN) at its "fast mode", for which the average velocity of the last three seconds was displayed. The measurements were taken through the aerosol sampling openings on the duct wall as well. Velocities were measured at the following traverse locations: 10%, 30%, 50%, 70%, and 90% (FIGURE 8.2.2). All measurements were taken with five repeats. The mean values of the measured velocities are shown in FIGURE 8.3.1 with the standard error for each data point listed in TABLE 8.3.1.

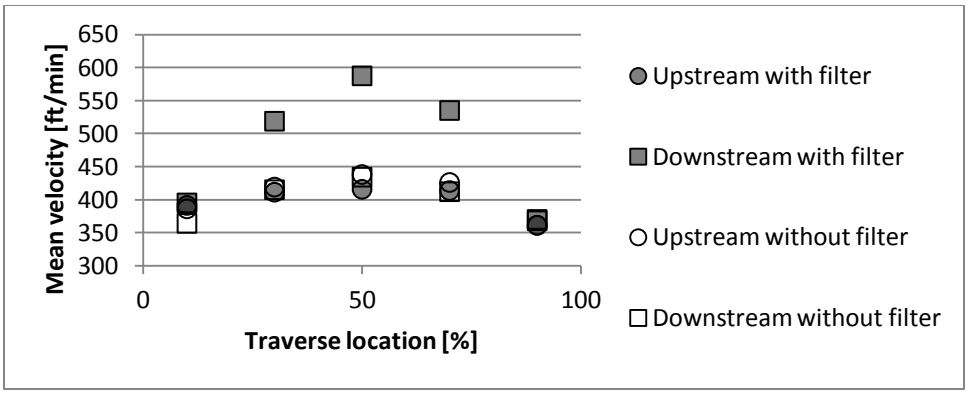

FIGURE 8.3.1 Velocity profiles at upstream and downstream locations with and without filter.

TABLE 8.3.1 The standard error [ft/min] for each data point in FIGURE 8.3.1.

Location (%)	10	30	50	70	90
Upstream with filter	3.2	3.1	3.1	2.8	8.3
Downstream with filter	2.9	62.4	65.6	53.3	11.5
Upstream without filter	3.7	11.8	14.0	9.4	8.1
Downstream without filter	13.6	4.7	11.9	5.4	8.0

Relative standard deviation or coefficient of variation (CV or COV) was calculated for each traversing measurement. With either filter installed, the upstream CV was 6.1%, and the downstream CV was 25.0%; without a filter, the upstream CV was 8.7%, and the downstream CV was 8.6%. Therefore, installing a filter did not significantly affect the upstream velocity profile. For the downstream velocity profile, when no filter was installed, it was similar to the upstream profile. When a filter was installed, however, both the maximum velocity magnitude and measurement fluctuation became greater. This could be due to the disturbed flow by filter pleats or the structural ribs on the filter frame, as the measurements were taken only 3 in (7.6 cm) downstream of the filter. From the velocity profiles in FIGURE 8.3.1, it appears that mass conservation was violated when a filter was installed. One reason could be the reduction of effective passage area in the filter due to pleats and ribs, causing a jet-like flow pattern. Another reason could be that the measured velocities were not in the main flow direction due to turbulence. The complex flow pattern downstream of a filter might affect the sampling efficiency, causing errors in filtration efficiency measurements, which could not be corrected with the correlation test, as it only appeared when a filter was mounted.

For the penetration uniformity test, aerosols were generated in the same way as the viral aerosol tests, except for the nebulizer fluid which used MEM instead of virus stock. Concentration was measured alternately between upstream and downstream locations by an optical particle counter (OPC) (Lasair 1002, Particle Measuring Systems, Inc., Boulder, CO) at four traverse locations of 25%, 50%, 75%, and 87.5 % with each filter and without a filter. Each OPC measurement was an average of one minute sampling. At least three repeated measurements were taken at each location and for each filter. The OPC size channels used for this test are shown in TABLE 8.3.2. The 0.3-0.4 μm channel was not used as that size range for virus particles was not studied here. The channel for particles greater than 2 μm was not used as well, because the particle counts were too low.

TABLE 8.3.2 The four size channels of the OPC used for the concentration uniformity test with geometric mean of upper and lower limits shown for each channel.

Channel (μm)	0.4-0.5	0.5-0.7	0.7-1.0	1.0-2.0
Geometric mean (μm)	0.447	0.592	0.837	1.414

Similar to the viral aerosol tests, a correlation test was carried out without a filter mounted (FIGURE 8.3.2). The correlation ratios did not significantly depend on particle size ($p=0.263$) or traverse location ($p=0.467$) by ANOVA. Therefore, a single correlation ratio of 0.98 with a standard error of 0.04 was used for all particle sizes and traverse locations. The corrected penetrations for MERV 8 and 13 are shown in FIGURE 8.3.2. The MERV 8 filter showed higher penetration than the MERV 13 filter for all particle sizes. The penetration for the first two particle sizes for the MERV 8 filter was greater than unity, meaning that their concentrations downstream were higher than those upstream. This could be partly due to the error in the correlation ratio, and partly due to the change in downstream flow pattern when the filter was mounted. ANOVA was carried out for penetration to study the factors of particle size and traverse location. For the MERV 8 filter, particle size was significant ($p<0.001$), and traverse location was not ($p=0.941$). For the MERV 13 filter, particle size was significant ($p<0.001$), and traverse location was not ($p=0.948$) as well. In summary, filtration efficiency depended on particle size, but the same filtration efficiency could be obtained at different traverse locations across the duct. This result also suggests that the downstream turbulent flow might not significantly affect the measurement of the filters' filtration efficiencies.

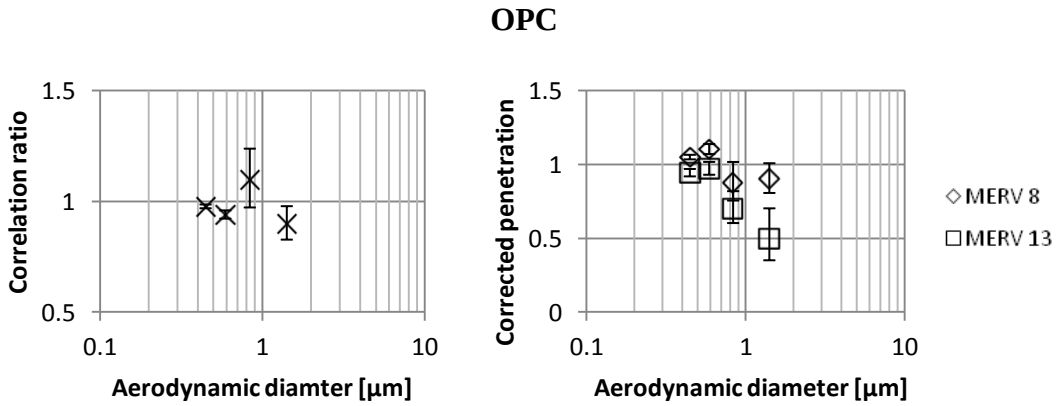

FIGURE 8.3.2 Correlation ratio (left) and Corrected penetration for each filter (right) versus particle aerodynamic diameter based on particle counting by OPC with error bars showing standard errors.

8.4 Results and discussion

8.4.1 Penetrations of live virus, total virus, and fluorescein

Penetrations of live virus, total virus, and fluorescein were calculated for each filter with correlation ratios applied. For live virus titer, AIV and HAdV-1 had very low resolution with only three data points in the range of each log. For example, only 1.48, 3.16, and 6.76 were used to express the titers between 1 and 10, with the ratio between any two adjacent values of about 2.15. This resolution was much lower than that of MS2, and may cause large errors in penetration. Therefore, the MS2 data were processed separately from AIV and HAdV-1. For MS2 penetration (FIGURE 8.4.1), both filter ($p<0.001$) and particle size ($p=0.006$) were significant, but their interaction was not ($p=0.491$). For AIV and HAdV-1 (FIGURE 8.4.2), virus type was not significant ($p=0.630$). The interaction between virus type and particle size ($p=0.573$), and that between virus type and filter ($p=0.588$) were not significant as well. The filter was significant ($p=0.020$), but the particle size ($p=0.339$), and the interaction between filter and particle size ($p=0.928$) were not significant. FIGURE 8.4.2 only shows impactor stages 2-7, because most live virus titers for impactor stages 0 and 1 downstream of a filter were too low to be detected. For all three viruses, filter was significant, and penetrations were greater for the MERV 8 filter. Particle

size was not significant for AIV and HAdV-1 by ANOVA, possibly because of the low resolution problem with their live virus titers.

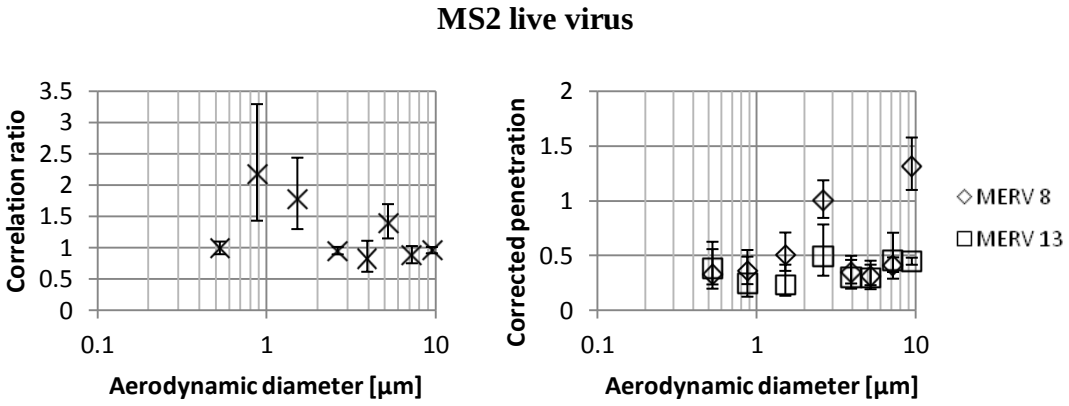

FIGURE 8.4.1 Correlation ratio (left) and corrected penetration for each filter (right) versus particle aerodynamic diameter based on MS2 live virus with error bars showing standard errors.

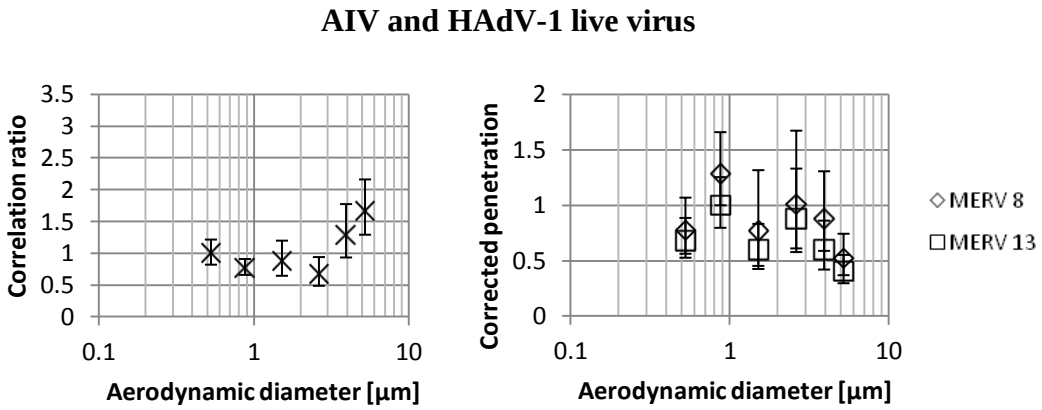

FIGURE 8.4.2 Correlation ratio (left) and corrected penetration for each filter (right) versus particle aerodynamic diameter based on AIV and HAdV-1 live virus with error bars showing standard errors.

For fluorescein penetration (FIGURE 8.4.3), virus type was not significant ($p=0.161$). The interaction between virus type and particle size was not significant ($p=0.118$), as well as that between virus type and filter ($p=0.749$). Both filter ($p<0.001$) and particle size ($p<0.001$) were significant, as well as the interaction between them ($p<0.001$). This significant interaction

suggests that the curves of filtration efficiency as a function of particle size for the two filters were significantly different.

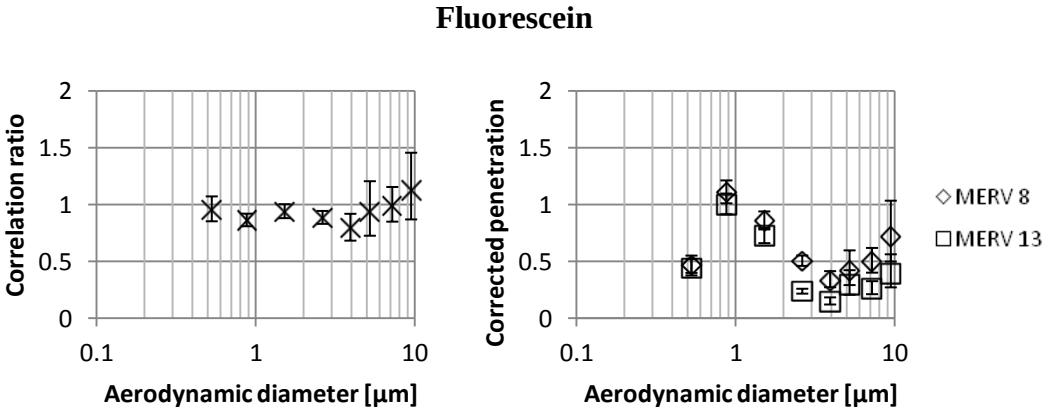

FIGURE 8.4.3 Correlation ratio (left) and corrected penetration for each filter (right) versus particle aerodynamic diameter based on fluorescein with error bars showing standard errors.

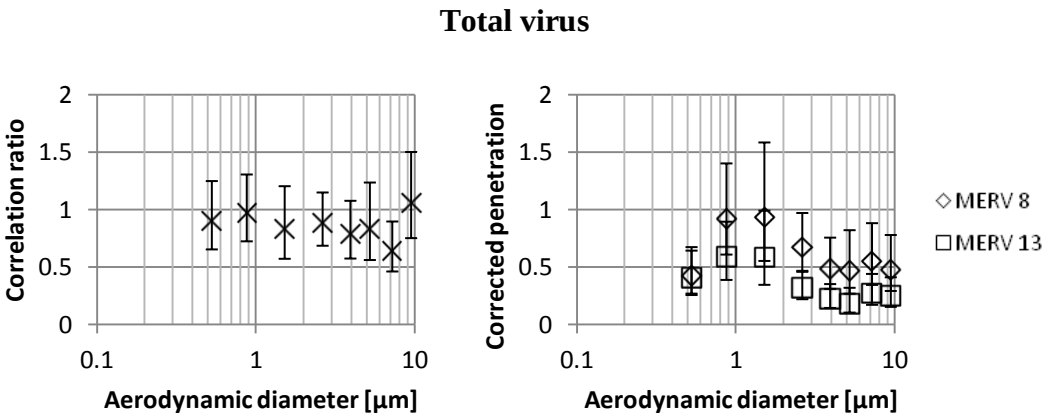

FIGURE 8.4.4 Correlation ratio (left) and corrected penetration for each filter (right) versus particle aerodynamic diameter based on total virus with error bars showing standard errors.

For total virus penetration (FIGURE 8.4.4), virus type was not significant ($p=0.238$). The interaction between virus type and particle size was not significant ($p=0.108$), as well as that between virus type and filter ($p=0.231$). Particle size and filter were both significant ($p<0.001$), as well as their interaction ($p<0.001$), which is the same as the fluorescein results. Both penetrations

for total virus and fluorescein did not significantly depend on virus type or suspension medium (TSB or MEM) showing that the filtration efficiencies for both media were similar, although the particle size distributions for the two suspensions were different as found in the previous tests in Chapters 4 and 5.

The penetrations calculated based on live virus titer, total virus concentration, and fluorescence intensity were converted to filtration efficiencies and compared with the OPC measurements, the MERV requirements (ANSI/ASHRAE 2007), and the filter test reports (Blue Heaven Technologies, Louisville, KY). The filter test reports provided by the seller were based on ANSI/ASHRAE 2007. A comparison was made for each test filter in FIGURE 8.4.5 without error bars shown.

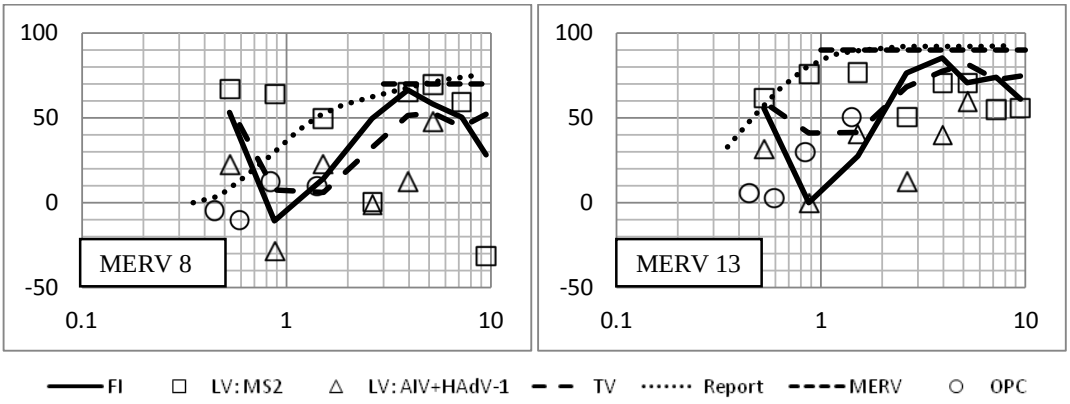

FIGURE 8.4.5 Comparison of filtration efficiencies [%] (vertical axes) as a function of particle aerodynamic diameter [μm] (horizontal axes) for each filter based on fluorescence intensity (FI), live virus (LV) titer, total virus (TV) concentration, the filter's standard test report, MERV requirement, and the particle concentration measured by OPC.

Compared with the references, the filtration efficiencies calculated in the current tests were generally lower. The main reason could be the lower face velocity. The secondary reason could be the disturbed flow downstream of the filter, which caused the difference between upstream and downstream sampling efficiencies, and this difference was not corrected by the correlation tests. The filtration efficiencies for MS2 live virus were higher than those for fluorescein, total virus, and AIV plus HAdV-1 live virus by mean value, especially at the impactor stages 5-6 (0.7-2.1

μm). This difference should be due to the corresponding high correlation ratios for MS2 live virus as shown in FIGURE 8.4.1.

Compared with the filters' standard test reports, two main differences in the measured filtration efficiency curves can be found. The first difference is that the filtration efficiency for impactor stage 7 (0.4-0.7 μm) was much higher than that of impactor stage 6 (0.7-1.1 μm). This trend is not present in the OPC test results, thus the reason might be associated with the impactor or the measurement of impactor samples. Except for this, the OPC data points are generally close to the fluorescein and total virus curves. The second difference is the decrease in filtration efficiency for particles greater than 4.7 μm (ACI stages 0-2). One reason could be the greater uncertainties and lower concentrations for these impactor stages. Another reason could be the flow recirculation downstream of the filter which actually increased the sampling efficiency for larger particles. Finally, the lower face velocity might have significantly reduced the impaction effect for larger particles, leading to the lower filtration efficiency for them.

TABLE 8.4.1 P-values for comparison of penetrations with significant factors in bold.

ANOVA model	Indicator	Size	Filter	I:S	I:F	S:F
MS2 LV and TV	0.284	**<0.001**	**<0.001**	0.915	0.687	0.176
MS2 LV and FI	0.056	**<0.001**	**<0.001**	0.154	0.368	0.051
AIV&HAdV-1 LV and TV	**<0.001**	0.330	**<0.001**	**0.048**	**0.029**	0.770
AIV&HAdV-1 LV and FI	**<0.001**	**<0.001**	**<0.001**	**<0.001**	**0.003**	**0.010**
All-virus TV and FI	0.753	**<0.001**	**<0.001**	**0.007**	0.563	**<0.001**

In order to compare the penetrations of different indicators, ANOVA models were built with the factors of indicator, particle size, and filter. The indicators include live virus (LV), total virus (TV), and fluorescein (FI). The p-values are listed in Table 8.4.1. For MS2, overall live virus penetration was not significantly different from overall fluorescein penetration, but the p-value for the indicator was very close to the threshold of significance. The interaction between indicator and particle size was not significant either, showing that both indicators had similar penetration curves, and the relative recoveries of the upstream samples were similar to those of the downstream samples. However, for AIV and HAdV-1, live virus was significantly different from fluorescein in both overall penetration and the penetration curve, which should be caused by the low resolution problem with the live virus titers of the two viruses.

Comparing total virus and live virus penetrations, both indicators were not significantly different for MS2 in either overall penetration or the size distribution of penetration. This means that the upstream survival was similar to the downstream survival, or MS2 was not significantly inactivated in the filtration process. This was expected as the test filters did not have any germicidal coating. However, for AIV and HAdV-1, the two processes were significantly different, and it should still be caused by the low resolution problem.

Comparison of total virus and fluorescein penetrations shows that the overall penetration levels for fluorescein and for total virus were similar, but their size distributions were significantly different. From FIGURE 8.4.5, their difference at the impactor stage 6 (0.7-1.1 μm) was much larger than those at other stages. The reason could simply be the large test uncertainty due to lack of test repeats. However, it also indicates the probability that fluorescein may not accurately predict the filtration behavior of virus for very small particles. For any specified particle size, fluorescence intensity should be proportional to particle concentration, thus the filtration efficiencies measured with a particle counter should be equal to those measured with fluorescein, and could also be different from those for total virus. Further research is therefore desirable to test filtration behavior of viral aerosols smaller than 2 μm with a higher resolution and a lower level of uncertainty.

8.4.2 Inactivation and concentrating in the nebulizer fluid

Fluid evaporation and virus inactivation were studied again for the one-hour nebulization with 20 psi (138 kPa) compressed air. The “post” fluorescence intensity was divided by the “pre” to calculate the concentration ratio due to water evaporation from the nebulizer during use. The concentration ratio significantly depended on virus type (p=0.038). By further analysis, MS2 was significantly different from HAdV-1 (0=0.023), while AIV was not (p=0.913). This indicates the suspension medium might be the significant factor. The concentration ratio for MS2 was 1.20 with a standard error of 0.03. For AIV and HAdV-1, it was 1.38+/-0.04. In Chapter 4, the one-hour ratio was about 1.11, and the six-hour ratio was about 1.21. It indicates that increasing the compressed air pressure from 10 psi (69 kPa) to 20 psi (138 kPa) significantly enhanced evaporation.

The parameter γ was calculated using EQUATION 4.4.3 to study virus inactivation during nebulization. Using fluorescein as the reference, γ did not significantly depend on virus type ($p=0.289$), and its mean value was calculated to be 1.34 with a 95% confidence interval of [1.06, 1.69]. This is surprising as γ should never become greater than unity. This result literally indicates that fluorescein concentration was increasing at a lower rate than virus concentration during nebulization, or virus was generated at a lower rate than fluorescein. This was possibly because the smallest particles produced by the nebulizer contained fluorescein, but no virus.

A similar analysis was done using total virus instead of fluorescein. For concentration ratio, virus type was not significant ($p=0.492$). The ratio of post over pre was 1.53 with a standard error of 0.14, which was greater than that for fluorescein. This result shows the concentrating effect was more significant for virus than for fluorescein, supporting the conclusion in the above paragraph. For γ, virus was not significant either ($p=0.172$). Its average was 1.16 with a 95% confidence interval of [0.86, 1.56], showing that the viruses were not significantly inactivated during nebulization. It also suggests that using total virus may be more suitable than using fluorescein to study virus inactivation in a nebulizer, given that the damage to virus did not significantly affect PCR measurements.

8.5 Conclusions

MS2, HAdV-1, and AIV were tested with two HVAC filters of MERV 8 and 13. The overall filtration efficiencies for fluorescein and for total virus were similar, but the filtration efficiencies at the impactor stage 6 (0.7-1.1 μm) were significantly different by ANOVA. This result suggests that using fluorescein might not accurately predict the filtration behavior of viruses on the small particles of about 1 μm in diameter.

The penetration of MS2 live virus was not significantly different from that of total virus, indicating negligible inactivation in the filtration process in the chemical-free filters. For AIV and HAdV-1, the live virus titers only used three data points per 1-log range, making the penetration

calculation inaccurate. It would be necessary to improve the analysis method before the animal viruses could be accurately tested.

The filtration efficiencies calculated for the two filters could not be compared directly to their standard performance due to two major limitations. Firstly, the face velocity was lower than the standard operating value. Secondly, the downstream sampling location was close to the filter, where the flow pattern was greatly disturbed. The complex flow field might have affected the aerosol sampling efficiency of the downstream probe, which was not corrected with the correlation test, as the problem only existed when a filter was mounted on the test duct.

At 20 psi (138 kPa) compressed air pressure, the evaporation effect of nebulizer fluid was more significant than that at 10 psi (69 kPa). Virus inactivation was not significant at 20 psi (138 kPa) for one hour nebulization based on survival. In the analysis for nebulizer fluid evaporation and inactivation, fluorescein and total virus gave different results. Further analysis revealed that the generation of fluorescein was faster than that of virus.

9 Key findings, recommendations, and limitations

9.1 Key findings and recommendations

In this study, viral aerosol survivability, transmission, and sampling were studied in an environmental chamber. Tests were first conducted to study the performance of the ACI for long-term sampling. The six-hour sampling did not collect much more live viruses than the one-hour sampling, indicating significant virus inactivation on the dry impaction plates. However, the increase in total virus collected in the six-hour tests suggests that using a PCR technique could benefit from longer sampling durations usually used for field sampling. Overloading of impaction plates with collected particles caused a decrease in the sampling efficiencies of some impactor stages, which should be noted when conducting long-term sampling. For the test viruses, MS2, HAdV-1, and AIV had greater relative recovery and survival than SIV, TGEV and aMPV. For MS2, the relative recovery and survival were constant for all sampled particle sizes, but for the other five viruses, a decrease in relative recovery and survival was found for larger particle sizes.

Based on the above results, MS2, AIV, and HAdV-1 were tested in the rest of the study. In the tests for different temperatures and humidities, all three viruses showed lower inactivation at lower temperature, but the inactivation of HAdV-1 at 30 ˚C was not significantly faster than that at 25 ˚C. The three viruses reacted differently to humidity changes. AH was found to be a better predictor of virus survival than RH. When modeling with AH, the interaction between temperature and humidity disappears. Therefore, documenting AH in future viral aerosol studies is recommended. For the three viruses used here, MS2 and HAdV-1 had the lowest inactivation rates at low AH, while AIV had the lowest inactivation rate at high AH for the tested AH range from 8.8 to 15.2 g/m^3. Note that the virus was inactivated both in the air and in the impactor. The current chamber tests simulated common indoor environments. For future research, it is desirable to test viral aerosols under more extreme temperatures and humidities.

In the UVGI tests, MS2, AIV, and HAdV-1 were all significantly inactivated by UVGI, showing the good potential of UVGI for disinfecting indoor air. The inactivation was caused by photochemical reaction in nucleic acid, thus the physical loss measured by PCR was exaggerated. Based on relative recovery, AIV was more susceptible to UVGI than MS2 or HAdV-1, which is consistent with past studies. To quantify virus susceptibilities, transient numerical simulations were conducted in CFX using Lagrangian particle tracking and log-linear inactivation kinetics. By analyzing a statistically converged group of particles, the susceptibility of each virus to UV irradiation was calculated. The mean susceptibility of MS2 was 0.057 cm^2/mJ with the range for one standard error to be [0.022, 0.098] cm^2/mJ. For HAdV-1, the susceptibility was 0.056 [0.035, 0.079] cm^2/mJ, and for AIV, it was 0.132 [0.031, 0.278] cm^2/mJ. These susceptibilities are about one order of magnitude lower than published viral aerosol data, but close to the water data. This result suggests that virus susceptibility to UVGI may not depend on the phase of the carrier fluid. UVGI effectiveness has been studied as a function of UVGI dose received, but whether irradiance may affect inactivation for the same dose is still unknown, especially when it is very low (<0.01 mW/cm^2) or very high (>1 mW/cm^2). It would also be desirable to test the UVGI effect at different RH levels, especially those above 80% or below 20% as there is still no conclusive result at these conditions. Further tests are strongly recommended to be conducted in a specially designed facility with strictly controlled irradiance and high repeatability.

In the HVAC filter tests, the overall filtration efficiencies for fluorescein and total virus were similar, but the filtration efficiencies at the impactor stage 6 (0.7-1.1 μm) were significantly different by ANOVA. This result suggests that using fluorescein may not accurately predict the filtration behavior of viruses on small particles. To be conclusive, however, more tests focusing on this size range are necessary. For MS2, no significant inactivation was found during the filtration process in the chemical-free filters. Since the method for the current filter tests did not strictly follow the existing test standard, the measured filtration efficiency curves were different from those provided in the standard test reports, and the results should not be used to indicate the performance of the test filters during normal operation. Due to the low resolution in live virus titer for HAdV-1 and AIV, the corresponding analysis was not useful. This issue needs to be resolved before these viruses should be tested again.

More than 95% of the collected particles by mass were smaller than 4.7 μm, and more than 40% were between 1.1 and 2.1 μm. Most of the particles were in the region of droplet nuclei, which would be the most important mode for natural viral aerosol transmission. Virus type did not significantly affect the particle size distribution in the samples, but the suspension medium was found to be a significant factor.

In the nebulizer fluid, the evaporation effect was more significant for longer test duration or higher compressed air pressure. Virus was not significantly inactivated in the one-hour tests with 20 psi (138 kPa) compressed air or in the six-hour tests with 10 psi (69 kPa) compressed air. Nebulization of fluorescein was found to be faster than that of virus. This result suggests that despite high repeatability, using fluorescein may not measure virus physical loss accurately for the whole process and may lead to different conclusions. Therefore, if virus nucleic acid was not significantly damaged, such as by UVGI, using total virus for physical loss would be a better choice. For future research, it is recommended to further compare the physical losses measured by both methods to determine whether the difference is only caused by different nebulization rates or also happens during viral aerosol transmission. For example, tests can be done by sampling the same aerosol at different time points during its transmission.

9.2 Limitations

Three major limitations of the current test method are summarized here for future reference. Firstly, despite their similarities, extrapolation of the current results based on MS2 and the five animal viruses to human viruses should be made carefully. Secondly, viral aerosol infectivity was not investigated in this study, in other words, high recovery of live viruses does not mean effective disease transmission. Thirdly, viral aerosols were generated from virus stocks with high titers in this study. On the other hand, natural viral aerosols were most likely generated from saliva or other bodily fluids which may have different effects on virus survivability depending on virus type. Studies with artificial or natural saliva, or even relying on patients or animals to generate viral aerosols could provide more realistic results, but also may be more difficult to achieve.

Bibliography

AIA, 2001, "Guidelines for design and construction of hospital and health care facilities," Washington, DC.

Agranovski I. E., Safatov A. S., Pyankov O. V., Sergeev A. A., Sergeev A. N., and Grinshpun S. A., 2005, "Long-term sampling of viable airborne viruses," Aerosol Science and Technology, 39(9), pp. 912–918.

Akers T. G., 1969, "Survival of airborne virus, phage and other minute microbes," In: An Introduction to Experimental Aerobiology, edited by Dimmick R. L., and Akers A. B., Wiley Interscience, New York, pp. 296–339.

Akers T. G., 1973, "Some aspects of the airborne inactivation of viruses," In: Airborne Transmission and Airborne Infection, edited by Hers J. F. P., and Winkler K. C., Oosthoek Publishing Company, Utrecht, the Netherlands, pp. 73–81.

Alani A., Barton I. E., Seymour M. J., and Wrobel L. C., 2001, "Application of Lagrangian particle transport model to tuberculosis (TB) bacteria UV dosing in a ventilated isolation room," International Journal of Environmental Health Research, 11, pp. 219–228.

Andersen A. A., 1958, "New sampler for the collection, sizing, and enumeration of viable airborne particles," Journal of Bacteriology, 76, pp. 471–484.

Andrews C. H., and Glover R. E., 1941, "Spread of infection from the respiratory tract of the ferret I. Transmission of influenza A virus," British Journal of Experimental Pathology, 22, pp. 91–97.

ANSI/ASHRAE, 2007, "Method of testing general ventilation air-cleaning devices for removal efficiency by particle size," ANSI/ASHRAE Standard 52.2-2007.

ANSYS, 2010, "ANSYS CFX-Solver Theory Guide," Release 13.0.

Appert J., Raynor P. C., Abin M., Chander Y., Guarino H., Goyal S. M., Zuo Z., Ge S., and Kuehn T. H., 2012, "Influence of suspending liquid, impactor type, and substrate on size-selective sampling of MS2 and adenoviral aerosols," Aerosol Science and Technology, 46, pp. 249–257.

ASHRAE, 2008, "ASHRAE Handbook."

ASHRAE, 2009, "ASHRAE Handbook – Fundamentals."

Assar S. K., and Block S. S., 2000, "Survival of microorganisms in the Environment," In: Disinfection, Sterilization, and Preservation, edited by Block S. S., Lippinkott-Williams.

Atkinson J., Chartier Y., Pessoa-Silva C. L., Jensen P., Li Y., and Seto W. H., 2009, "Natural ventilation for infection control in health-care settings," World Health Organization Publication/Guidelines.

Becker M. M., and Wang Z., 1989, "Origin of ultraviolet damage in DNA," Journal of Molecular Biology, 210, pp. 429–438.

Beggs C. B., Kerr K. G., Donnelly J. K., Sleigh P. A., Mara D. D., and Cairns G., 2000, "An engineering approach to the control of Mycobacterium tuberculosis and other airborne pathogens: A UK hospital based pilot study," Transaction of the Royal Society of Tropical Medicine and Hygiene, 94, pp. 141–146.

Beggs C. B., 2002a, "A quantitative method for evaluating the photoreactivation of ultraviolet damaged microorganisms," Photochemical & Photobiological Sciences, 1(6), pp. 431–437.

Beggs C. B., and Sleigh P. A., 2002b, "A quantitative method for evaluating the germicidal effect of upper room UV fields," Journal of Aerosol Science, 33, pp. 1681–1699.

Benbough J. E., 1969, "The effect of relative humidity on the survival of airborne Semliki Forest virus," Journal of General Virology, 4, pp. 473–477.

Benbough J. E., 1971, "Some factors affecting the survival of airborne viruses," Journal of General Virology, 10, pp. 209–220.

Bishop J. M., Quintrell N., and Koch G., 1967, "Poliovirus double-stranded RNA: Inactivation by ultraviolet light," Journal of Molecular Biology, 24, pp. 125–128.

Blachere F. M., Lindsley W. G., Pearce T. A, Anderson S. E., Fisher M., Khakoo R., Meade B. J., Lander O., Davis S., Thewlis R. E., Celik I., Chen B. T., and Beezhold D. H., 2009, "Measurement of airborne influenza virus in a hospital emergency department," Clinical Infectious Diseases, 48(4), pp. 438–440.

Blachere F. M., Cao G., Lindsley W. G., Noti J. D., and Beezhold D. H., 2011, "Enhanced detection of infectious airborne influenza virus," Journal of Virological Methods, 176(1-2), pp. 120–124.

Blatchley E. R., 1997, "Numerical modeling of UV intensity: Application to collimated-beam reactors and continuous-flow systems," Water Research, 31(9), pp. 2205–2218.

Blatchley E. R., Do-Quang Z., Janex M. L., and Laine J. M., 1998, "Process modelling of ultraviolet disinfection," Water Science Technology, 38, pp. 63–69.

Blatchley E. R., and Heber A. J., 2007, "A report on two water recycle and air revitalization projects," Advanced Life Support-NASA Specialized Center of Research and Training (ALS-NSCORT), Annual and Monthly Reports.

Booth T. F., Kournikakis B., Bastien N., Ho J., Kobasa D., Stadnyk L., Li Y., Spence M., Paton S., Henry B., Mederski B., White D., Low D. E., McGeer A., Simor A., Vearncombe M., Downey J., Jamieson F. B., Tang P., and Plummer F., 2005, "Detection of airborne severe acute

respiratory syndrome (SARS) coronavirus and environmental contamination in SARS outbreak units," Journal of Infectious Diseases, 191(9), pp. 1472–1477.

Brickner P. W., Vincent R. L., First M., Nardell E., Murray M., and Kaufman W., 2003, "The application of ultraviolet germicidal irradiation to control transmission of airborne disease: Bioterrorism countermeasure," Public Health Reports, 118, pp. 99–114.

Bridges C. B, Kuehnert M. J., Hall C. B., 2003, "Transmission of influenza: implications for control in health care settings," Clinical Infectious Diseases, 37, pp. 1094–1101.

Broor S., and Bharaj P., 2007, "Avian and human metapneumovirus," Annals of the New York Academy of Sciences, 1102, pp. 66–85.

Buckland F. E., and D. A. Tyrrell D. A., 1962, "Loss of infectivity on drying various viruses," Nature, 195, pp. 1063–1064.

Burton N. C., Grinshpun S. A., and Reponen T., 2007, "Physical collection efficiency of filter materials for bacteria and viruses," the Annals of Occupational Hygiene, 51(2), pp. 143–151.

Casanova L. M., Jeon S., Rutala W. A., Weber D. J., and Sobsey M. D., 2010, "Effects of air temperature and relative humidity on coronavirus survival on surfaces," Applied and Environmental Microbiology, 76(9), pp. 2712–2717.

Casarett A. P., 1968, "Radiation Biology," Prentice-Hall, Englewood.

Cavanagh D., and the Coronaviridae Study Group of the International Committee on Taxonomy of Viruses, 1994, "Revision of the taxonomy of the coronavirus, torovirus, and arterivirus genera," Archives of Virology, 135, pp. 226–237.

CDC, 1994, "Guidelines for preventing the transmission of Mycobacterium tuberculosis in health-care facilities," Morbidity and Mortality Weekly Report, 43(R-13), pp. 1–132.

CDC, 2003, "Cluster of severe acute respiratory syndrome cases among protected health-care workers – Toronto, Canada, April 2003," Morbidity and Mortality Weekly Report, 52(19), pp. 433–436.

CDC, 2005, "Guidelines for preventing the transmission of Mycobacterium tuberculosis in health-care settings," Morbidity and Mortality Weekly Report, 54 (RR-17), pp. 1–140.

Cerf O., 1977, "A review: Tailing of survival curves of bacterial spores," Journal of Applied Bacteriology, 42, pp. 1–19.

Chandrasekhar D., and van Houten B., 2000, "In vivo formation and repair of cyclobutane pyrimidine dimers and 6–4 photoproducts measured at the gene and nucleotide level in Escherichia coli," Mutation Research, 450, pp. 19–40.

Chao C. Y. H., Wan M. P., and Sze To G. N., 2008, "Transport and removal of expiratory droplets in hospital ward environment," Aerosol Science and Technology, 42, pp. 377–394.

Chen Q., 1995, "Comparison of different k-ε models for indoor air flow computations," Numerical Heat Transfer, Part B: Fundamentals, 28, pp. 353–369.

Chen B. T., and John W., 2001a, "Instrument calibration," In: Aerosol Measurement: Principles, Techniques and Applications, edited by Baron P. A., and Willeke K., Wiley-Interscience, New York, pp. 627–666.

Chen Q., and Srebric J., 2001b, "Simplified diffuser boundary conditions for numerical room airflow models," Final Report, ASHRAE RP-1009.

Cho M., Chung H., Choi W., and Yoon J., 2005, "Different inactivation behaviors of MS-2 phage and Escherichia coli in TiO2 photocatalytic disinfection," Applied and Environmental Microbiology, 71(1), pp. 270–275.

Choudhury D., 1993, "Introduction to the renormalization group method and turbulence modeling," Fluent, Inc. Technical Memorandum TM-107, Canonsburg.

Christian M. D., Loutfy M., McDonald L. C., Martinez K. F., Ofner M., Wong T., Wallington T., Gold W. L., Mederski B., Green K., Low D. E., and the SARS Investigation Team, 2004, "Possible SARS coronavirus transmission during cardiopulmonary resuscitation," Emerging Infectious Diseases, 10, pp. 287–293.

Chu C., Cheng V., Hung I., Chan K., Tang B., Tsang T., Chan K., and Yuen K., 2005, "Viral load distribution in SARS outbreak," Emerging Infectious Diseases, 11, pp. 1882–1886.

Collins F. M., 1971, "Relative susceptibility of acid-fast and non-acid-fast bacteria to ultraviolet light," Applied Microbiology, 21, pp. 411–413.

Collison W. E., 1935, "Inhalation therapy technique," Heinemann, London.

Comelis J. J., Su Z. Z., Rommelaere J., 1982, "Direct and indirect effects of ultraviolet light on the mutagenesis of parvovirus H-1 in human cells," EMBO Journal, 1(6), pp. 693–699.

Cook M. J., and Lomas K. J., 1998, "Buoyancy driven displacement ventilation flows: Evaluation of two eddy viscosity turbulence models for prediction," Building Services Engineering Research and Technology, 19(1), pp. 15–21.

Couch R. B., Cate T. R., Douglas R. G., Gerone P. J. J., and Knight V., 1966, "Effect of route of inoculation on experimental respiratory viral disease in volunteers and evidence for airborne transmission," Bacteriological Reviews, 30(3), pp. 517–529.

Cox C. S., and Wathes C. M., 1995, "Bioaerosols Handbook," First Edition, CRC Press, ISBN: 9780873716154.

Dani M. A., Durigon E. L., and Arns C. W., 1999, "Molecular characterization of Brazilian avian pneumovirus isolates: comparison between immunochemiluminescent Southern blot and nested PCR," Journal of Virological Methods, 79(2), pp. 237–241.

David H. L., 1973, “Response of Mycobacteria to ultraviolet light radiation,” American Review of Respiratory Diseases, 180, pp. 1175 –1185.

Davidovich I. A., and Kishchenko G. P., 1991, “The shape of the survival curves in the inactivation of viruses,” Molecular Genetics, Microbiology and Virology, 6, pp. 13–16.

Davis W. G., Griesemer A. R., Shadduck A. J., and Farrelle L. R., 1971, “Effect of relative humidity on dynamic aerosols of adenovirus 12,” Applied Microbiology, 21, pp. 676–679.

de Jong J. G., and Winkler K. C., 1964, “Survival of measles virus in air,” Nature, 201, pp. 1054–1055.

de Jong J. C., Trouwborst T., and Winkler K. C., 1973, “The mechanism of virus decay in aerosols,” In: Airborne Transmission and Airborne Infection, edited by Hers J. F. P., and Winkler K. C., Oosthoek Publishing Company, Utrecht, the Netherlands, pp. 124–130.

Dee S. A., Deen J., Cano J. P., Batista L., and Pijoan C., 2006, “Further evaluation of alternative air-filtration systems for reducing the transmission of Porcine reproductive and respiratory syndrome virus by aerosol,” Canadian Journal of Veterinary Research (Revue canadienne de recherche v é é rinaire), 70(3), pp. 168–175.

Deshmukh D. R., and Pomeroy B. S., 1969, “Ultraviolet inactivation and photoreactivation of avian viruses,” Avian Diseases, 13(3), pp. 596–602.

Dewulf J., Laevens H., Koenen F., Mintiens K., and Kruif A. de, 2000, “Airborne transmission of classical swine fever virus under experimental conditions,” Veterinary Record, 147, pp. 735–738.

Donaldson A. I., and Ferris N. P., 1975, “The survival of foot-and-mouth disease virus in open air conditions,” Journal of Hygiene, 74(3), pp. 409–416.

Dong H., Zhang Y., Xiong H., Yan A., Ding G., Chen Y., Xie L., Chen J., Zhang G., Hao P., Cong L., Lu Y., Che X., Wang X., Li Y., Yuen K. Y., Zhao G., and Jin W., 2010, “Detection of human novel influenza A (H1N1) viruses using multi-fluorescent real-time RT-PCR,” Virus Research, 147, pp. 85–90.

Downes A. and Blount T. P., 1877, “Research on the effect of light upon bacteria and other organisms,” Proceedings of the Royal Society of London, 26, pp. 488–500.

Dubovi E. J., and Akers T. G., 1970, “Airborne stability of tailless bacterial viruses S-13 and MS-2,” Applied Microbiology, 19(4), pp. 624–628.

Ducoste J. J., Liu D., and Linden K., 2005, “Alternative approaches to modeling fluence distribution and microbial inactivation in ultraviolet reactors: Lagrangian versus Eulerian,” Journal of Environmental Engineering, 131(10), pp. 1393–1404.

Emvin P., and Davidson L., 1996, “A numerical comparison of three inlet approximations of the diffuser in case E1 Annex20,” 5th International Conference on Air Distributions in Rooms, ROOMVENT ’96, 1, pp. 219–226.

Eninger R. M., Honda T., Adhikari A., Heinonen-Tanski H., Reponen T., and Grinshpun S. A., 2008, "Filter performance of N99 and N95 facepiece respirators against viruses and ultrafine particles," Annals of Occupational Hygiene, 52, pp. 385–396.

Escors D., Ortego J., Laude H., and Enjuanes L., 2001, "The membrane M protein carboxy terminus binds to transmissible gastroenteritis coronavirus core and contributes to core stability," Journal of Virology, 75, pp. 1312–1324.

Fabian P., McDevitt J. J., Houseman E. A., and Milton D. K., 2009, "Airborne influenza virus detection with four aerosol samplers using molecular and infectivity assays: considerations for a new infectious viral aerosol sampler," Indoor Air, 19, pp. 433–441.

Farnsworth J. E., Goyal S. M., Kim S. W., Kuehn T. H., Raynor P. C., Ramakrishnan M. A., Anantharaman S., and Tang W., 2006, "Development of a method for bacteria and virus recovery from heating, ventilation, and air conditioning (HVAC) filters," Journal of Environmental Monitoring, 8(10), p. 1006.

Finley W. H., 2001, "The mechanics of inhaled pharmaceutical aerosols," Academic Press, San Diego.

First M. W., Macher J., Gussman R., Stuart D., and Webb T., 1998, "Nebulizer characteristics for certification tests of biosafety cabinets with bacteria and simulants," Journal of the American Biological Safety Association, 3(1), pp. 26–29.

Fujikawa H., and Itoh T., 1996, "Tailing of thermal inactivation curve of Aspergillus niger spores," Applied Microbiology, 62(10), pp. 3745–3749.

Gao N. P., and Niu J. L., 2007, "Modeling particle dispersion and deposition in indoor environments," Atmospheric Environment, 41(18), pp. 3862–3876.

Garner J. S., and the Hospital Infection Control Practices Advisory Committee, 1996, "Guidelines for isolation precautions in hospitals," American Journal of Infection Control, 24, pp. 24–52.

Gerba C. P., Gramos D. M., and Nwachuku N., 2002, "Comparative inactivation of enteroviruses and adenovirus 2 by UV light," Applied and Environmental Microbiology, 68(10), pp. 5167–5169.

Ginsberg H. S., 1956, "Characteristics of the new respiratory viruses (adenoviruses). II. Stability to temperature and pH alterations," Experimental Biology and Medicine, 93(1), pp. 48–52.

Goldner J. L., Moggio M., Beissinger S. F., and McCollum D. E., 1980, "Ultraviolet light for the control of airborne bacteria in the operating room," In: Airborne Contagion, edited by Kundsin R. B., New York Academy of Sciences, New York, pp. 271–284.

Goyal S. M., Anantharaman S., Ramakrishnan M. A., Sajja S., Kim S. W., Stanley N. J., Farnsworth J. E., Kuehn T. H., and Raynor P. C., 2011, "Detection of viruses in used ventilation filters from two large public buildings," American Journal of Infection Control, 39(7), pp. e30–38.

Grinshpun S. A., Willeke K., Ulevicius V., Juozaitis A., Terzieva S., Donnelly J., Stelma G. N., and Brenner K. P., 1997, "Effect of impaction, bounce and reaerosolization on the collection efficiency of impingers," Aerosol Science and Technology, 26(4), pp. 326–342.

Harm W., 1980, "Biological effects of ultraviolet radiation," Cambridge University Press, Cambridge, United Kingdom.

Harper G. J., Hood A. M., and Morton J. D., 1958, "Airborne micro-organisms: a technique for studying their survival," Journal of Hygiene, 56(3), pp. 362–370.

Harper G. J., 1961, "Airborne microorganisms: Survival tests with four viruses," Journal of Hygiene (Cambridge), 59, pp. 479–486.

Harper G. J., 1963, "The influence of environment on the survival of airborne virus particles in the laboratory," Arch. ges. Virusforsch., 13, pp. 64–71.

Harstad J. B., 1965, "Sampling submicron T1 bacteriophage aerosols," Applied Microbiology, 13, pp. 899–908.

Hart D., 1937, "Operating room infections: Preliminary report," Archives of Surgery, 34, pp. 874–896.

Hatch T. R., and Gross P., 1964, "Pulmonary deposition and retention of inhaled aerosols," Academic Press, Inc., New York.

Hatch M. T., and Warren J. C., 1969, "Enhanced recovery of airborne T3 coliphage and Pasteurella pestis bacteriophage by means of a presampling humidification technique," Applied Microbiology, 17, pp. 685–689.

He G., Yang X., and Srebric J., 2005, "Removal of contaminants released from room surfaces by displacement and mixing ventilation: modeling and validation," Indoor Air, 15(5), pp. 367–380.

Heikkinen J., 1991, "Modelling of a supply air terminal for room air flow simulation," Proceedings of 12th AIVC Conference, Ottawa, Canada.

Hemmes J. H., Winkler K. C., Kool S. M., 1960, "Virus survival as a seasonal factor in influenza and poliomyelitis," Nature, 188, pp. 430–438.

Henkes R. A. W. M., 1990, "Natural convection boundary layers," Thesis, Delft University of Technology, Delft, The Netherlands.

Henri V., 1914, "Etude de l'action m etabolique des rayons ultraviolets," C. R. Acad. Sci. (Paris) 159, pp. 340–343.

Hijnen W. A. M., Beerendonk E. F., and Medema G. J., 2006, "Inactivation credit of UV radiation for viruses, bacteria and protozoan (oo)cysts in water: A review," Water Research, 40(1), pp. 3–22.

Hinds W. C., 1999, “Aerosol technology,” Second Edition, Wiley-Interscience, New York, NY, ISBN: 9780471194101.

Hocking M. B., 2000, “Passenger aircraft cabin air quality: trends, effects, societal costs, proposals,” Chemosphere, 41, pp. 603–615.

Hogan C. J., Kettleson E. M., Lee M. H., Ramaswami B., Angenent L. T., and Biswas P., 2005, “Sampling methodologies and dosage assessment techniques for submicrometre and ultrafine viral aerosol particles,” Journal of Applied Microbiology, 99(6), pp. 1422–1434.

Hollander A., 1942, “Abiotic and sublethal effects of ultraviolet radiation in the microorganisms,” In: Aerobiology, edited by Moulton F. R., American Association for the Advancement of Science, The Science Press Printing Co., Lancaster, PA.

Hollander A., 1943, “Effect of long ultraviolet and short visible radiation (3500 to 4900) on Escherichia coli,” Journal of Bacteriology, 46, pp. 531–541.

Hood A. M., 1963, “Infectivity of influenza viral aerosols,” Journal of Hygiene (Cambridge), 61, pp. 331–335.

Hopkins S. R., and Drury L. N., 1971, “Efficacy of air filters in preventing transmission of Newcastle disease,” Avian Diseases, 15, pp. 596–603.

Huang R., Agranovski I., Pyankov O., and Grinshpun S., 2008, “Removal of viable bioaerosol particles with a low-efficiency HVAC filter enhanced by continuous emission of unipolar air ions,” Indoor Air, 18(2), pp. 106–112.

Huffman R. E., 1992, “Atmospheric ultraviolet remote sensing,” Academic Press, San Diego, USA.

Hwang G. B., Lee J. E., Nho C. W., Lee B. U., Lee S. J., Jung J. H., and Bae G. N., 2012, “Short-term effect of humid airflow on antimicrobial air filters using Sophora flavescens nanoparticles,” Science of the Total Environment, 421-422, pp. 273–279.

Hyland R. W., and Wexler J., 1983, “Formulations for the thermodynamic properties of the saturated phases of H2O from 173.15 K to 473.15 K,” ASHRAE Transactions, 89(2A), pp. 500–519.

IESNA, 2000, “Lighting Handbook: Reference & Application,” Illumination Engineering Society of North America, New York.

Ijaz M. K., Brunner A. H., Sattar S. A., Nair R. C., and Johnson-Lussenburg C. M., 1985, “Survival characteristics of airborne human coronavirus 229E,” Journal of General Virology, 66, pp. 2743–2748.

Ijaz M. K., Karim Y. G., Sattar S. A., and Johnson-Lussenburg C. M., 1987, “Development of methods to study the survival of airborne viruses,” Journal of Virological Methods, 18(2-3), pp. 87–106.

Jackwood M. W., 2006, “The relationship of severe acute respiratory syndrome coronavirus with avian and other coronaviruses,” Avian Diseases, 50, pp. 315–320.

Jacobs G. H., 1992, “Ultraviolet vision in vertebrates,” American Zoologist, 32: pp. 544–554.

Jagger J., and Stafford R. S., 1965, “Evidence for two mechanisms of photoreactivation in Escherichia Coli B,” Biophysical Journal, 5(1), pp. 75–88.

Jensen M. M., 1964, “Inactivation of airborne viruses by ultraviolet irradiation,” Applied Microbiology, 12(5), pp. 418–420.

Jeong J., Bem J., Bahnfleth W. P., Freihaut J. D., and Thran B., 2009, “Critical review of aerosol particle transport models for building HVAC ducts,” Journal of Architectural Engineering, 2009(September), pp. 74–84.

Jin M., Zuo W., and Chen Q., 2012, “Improvements of fast fluid dynamics for simulating air flow in buildings,” Numerical Heat Transfer, Part B: Fundamentals, 62(6), pp. 419–438.

Jones R. C., 2000, “Avian pneumoviruses – an update,” International Hatchery Practice, 21(2), pp. 13–15.

Juhasz K., and Easton A. J., 1994, “Extensive sequence variation in the attachment (G) protein gene of avian pneumovirus: evidence for two distinct subgroups,” Journal of General Virology, 75, pp. 2873–2880.

Kallenbach N. R., Cornelius P. A., Negus D., Montgomerie D., and Englander S., 1989, “Inactivation of viruses by ultraviolet light,” In: Virus Inactivation in Plasma Products, edited by Morgenthaler J. J., Karger, Basel, Switzerland.

Karber G., 1931, “Fifty percent endpoint calculation,” Archives of Experimental Pathology and Pharmacology, 162, pp. 480–487.

Kelner A., 1949, “Effect of visible light on the recovery of Streptomyces griseus conidia from ultra-violet irradiation injury,” Proceedings of the National Academy of Sciences, 35(2), pp. 73–79.

Kennedy M. A., and Parks R. J., 2009, “Adenovirus virion stability and the viral genome: size matters,” Molecular Therapy, 17(10), pp. 1664–1666.

Kida H., Ito T., Yasuda J., Shimizu Y., Itakura C., Shortridge K. F., Kawaoka Y., and Webster R. G., 1994, “Potential for transmission of avian influenza viruses to pigs,” Journal of General Virology, 75, pp. 2183–2188.

Ko G., First M. W., and Burge H. A., 2002, “The characterization of upper-room ultraviolet germicidal irradiation in inactivating airborne microorganisms,” Environmental Health Perspectives, 110, pp. 95–101.

Ko G., Cromeans T. L., and Sobsey M. D., 2005, “UV inactivation of adenovirus type 41 measured by cell culture mRNA RT-PCR,” Water Research, 39(15), pp. 3643–3649.

Koch A. L., 1966, “The logarithm in biology: Mechanisms generating the lognormal distribution exactly,” Journal of Theoretical Biology, 12, pp. 276–290.

Kowalski W. J., Bahnfleth W. P., Witham D. L., Severin B. F., and Whittam T. S., 2000, “Mathematical modelling ofultraviolet germicidal irradiation for air disinfection,” Quantitative Microbiology, 2, pp. 249–270.

Kowalski W. J., 2001, “Design and optimization of UVGI air disinfection systems,” Doctor’s Thesis in Architectural Engineering, Pennsylvania State University.

Kowalski W. J., 2009, “Ultraviolet Germicidal Irradiation Handbook: UVGI for Air and Surface Disinfection,” Springer Berlin Heidelberg, ISBN: 9783642019982.

Kristensen C. S., Bøtner A., Takai H., Nielsen J. P., and Jorsal S. E., 2004, “Experimental airborne transmission of PRRS virus,” Veterinary Microbiology, 99(3-4), pp. 197–202.

Kujundzic E., Hernandez M., and Miller S. L., 2007, “Ultraviolet germicidal irradiation inactivation of airborne fungal spores and bacteria in upper-room air and in-duct configurations,” Journal of Environmental Engineering and Science, 6, pp. 1–9.

Kundsin R. B., 1984, “Hygienic significance of micro-organisms in the hospital environment,” Proceedings of Seventh Life Sciences Symposium, Knoxville, TN., pp. 171–181.

Lai A. C. K., and Cheng Y. C., 2007, “Study of expiratory droplet dispersion and transport using a new Eulerian modeling approach,” Atmospheric Environment, 41, pp. 7473–7484.

Lamb R. A., and Choppin P. W., 1983, “The gene structure and replication of influenza virus,” Annual Review of Biochemistry, 52, pp. 467–506.

Laube T., Apel H., and Koch H. R., 2004, “Ultraviolet radiation absorption of intraocular lenses,” Ophthalmology, 111(5), pp. 880–885.

Lee J. H., 2009, “Assessment of the performance of iodine-treated biocidal filters and characterization of viral aerosols,” PhD Thesis, University of Florida-Gainesville.

Lennox E. S., Luria S. E., and Benzer S., 1954, “On the mechanism of photoreactivation of ultraviolet-inactivated bacteriophage,” Biochimica et Biophysica Acta, 15, pp. 471–474.

Li X., Liu Q., Bi X., Sheng G., Fu J., Ran P., and Li B., 2008, “An in vitro model to evaluate viral aerosol characteristics using a GFP-expressing adenovirus,” Journal of Medical Microbiology, 57(Pt 11), pp. 1335–1339.

Liang H., 1994, “Room air movement and contaminant transport,” ProQuest Dissertations and Thesis.

Liao M., Cheng K., Yang J., Zhao Y., and Shi Z., 2010, “Assessment of UV-B damage in cyanophage PP,” Aquatic Microbial Ecology, 58, pp. 323–328.

Liu B. Y. H., and Pui D. Y. H., 1986, “Instrumentation for aerosol measurement,” In: Handbook of Contamination Control in Microelectronics, edited by Tolliver D. L., Noyes Publications, Park Ridge, New Jersey, pp. 68–109.

Lodge J. P., and Chan T. L., 1986, “Cascade impactor,” American Industrial Hygiene Association, Akron, Ohio.

Loosli C. G., Lemon H. M., Robertson O. H., and Appel E., 1943, “Experimental airborne influenza infection. I. Influence of humidity on the survival of virus in air,” Proceedings of the Society for Experimental Biology and Medicine, 53, pp. 205–206.

Lowen A. C., Mubareka S., Steel J., and Palese P., 2007, “Influenza virus transmission is dependent on relative humidity and temperature,” PLoS Pathogens, 3(10), pp. 1470–1476.

Luckiesh M., 1946, “Applications of germicidal, erythemal and infrared energy,” Van Nostrand Co., Inc., New York, pp. 107–108.

Marks P. J., Vipond I. B., Carlisle D., Deakin D., Fey R. E., and Caul E. O., 2000, “Evidence for airborne transmission of Norwalk-like virus (NLV) in a hotel restaurant,” Epidemiology and Infection, 124(3), pp. 481–487.

Masschelein W. J., 2002, “Ultraviolet light in water and wastewater sanitation,” Lewis Publishers, Boca Raton.

May K. R., 1973, “The Collison nebulizer: description, performance, and application,” Aerosol Science, 4, pp. 235–243.

Mazumdar S., and Chen Q., 2008, “Influence of cabin conditions on placement and response of contaminant detection sensors in a commercial aircraft,” Journal of Environmental Monitoring, 10, pp. 71–81.

Mbithi J. N., Springthorpe V. S., and Sattar S. A., 1991, “Effect of relative humidity and air temperature on survival of Hepatitis A virus on environmental surfaces,” Applied and Environmental Microbiology, 57(5), pp. 1394–1399.

McCullough N. V., Brosseau L. M., and Vesley D., 1997, “Collection of three bacterial aerosols by respirator and surgical mask filters under varying conditions of flow and relative humidity,” Annals of Occupational Hygiene, 41(6), pp. 677–690.

McDevitt J., Rudnick S., First M., and Spengler J., 2010, “Role of absolute humidity in the inactivation of influenza viruses on stainless steel surfaces at elevated temperatures,” Applied and Environmental Microbiology, 76(12), pp. 3943–3947.

McLean R. L., 1961, “The effect of ultraviolet radiation upon the transmission of epidemic influenza in long-term hospital patients,” American Review of Respiratory Disease, 83(2 Part 2), pp. 36–38.

Memarzadeh F., 2000a, "Assessing the efficacy of ultraviolet germicidal irradiation and ventilation in removing Mycobacterium tuberculosis," NIH, Division of Engineering Services, Bethesda, MD.

Memarzadeh F., and Jiang J., 2000b, "Methodology for minimizing risk from airborne organisms in hospital isolation rooms," ASHRAE Transactions, 106(2), pp. 731–747.

Memarzadeh F., Jiang Z., and Xu W., 2004, "Analysis of efficacy of UVGI inactivation of airborne organisms using Eulerian and Lagrangian approaches," Indoor Air Quality.

Memarzadeh F., Olmsted R. N., and Bartley J. M., 2010, "Applications of ultraviolet germicidal irradiation disinfection in health care facilities: effective adjunct, but not stand-alone technology," American Journal of Infection Control, 38(5 Supplement 1), pp. S13–24.

Memarzadeh F., 2012, "Literature review of the effect of temperature and humidity on viruses," ASHRAE Winter Conference.

Meng Q. S., and Gerba C. P., 1996, "Comparative inactivation of enteric adenoviruses, poliovirus and coliphages by ultraviolet irradiation," Water Research, 30, pp. 2665–2668.

Miller W. S., and Artenstein M. S., 1967, "Aerosol stability of three acute respiratory disease viruses," Proceedings of the Society for Experimental Biology and Medicine, 125, pp. 222–227.

Miller S. L., and MacHer J. M., 2000, "Evaluation of a methodology for quantifying the effect of room air ultraviolet germicidal irradiation on airborne bacteria," Aerosol Science and Technology, 33(3), pp. 274–295.

Mitchell C. A., Guerin L. F., and Robillard J., 1968, "Decay of influenza A viruses of human and avian origin," Canadian Journal of Comparative Medicine, 32(4), pp. 544–546.

Mitchell C. A., and Guerin L. F., 1972, "Influenza A of human, swine, equine and avian origin: comparison of survival in aerosol form," Canadian Journal of Comparative Medicine, 36(1), pp. 9–11.

Moats W. A., Dabbah R., and Edwards V. M., 1971, "Interpretation of nonlogarithmic survivor curves of heated bacteria," Journal of Food of Science, 36, pp. 523–526.

Mohr A. J., 1991, "Development of models to explain the survival of viruses and bacteria in aerosols," In: Modeling the Environmental Fate of Microorganisms, edited by Hurst C. J., American Society Microbiology (ASM) Press, Washington, DC, pp. 160–190.

Moser M. R., Bender T. R., Margolis H. S., Noble G. R., Kendal A. P., and Ritter D. G., 1979, "An outbreak of influenza aboard a commercial airliner," American Journal of Epidemiology, 110, pp. 1–6.

Mubareka S., Lowen A. C., Steel J., Coates A. L., Garc á-Sastre A., and Palese P., 2009, "Transmission of influenza virus via aerosols and fomites in the guinea pig model," Journal of Infectious Diseases, 199(6), pp. 858–865.

Munakata N., Saito M., and Hieda K., 1991, "Inactivation action spectra of Bacillus subtilis spores in extended ultraviolet wavelengths (50-300 nm) obtained with synchrotron radiation," Photochemstry and Photobiology, 54(5), pp. 761–768.

Munster V. J., de Wit E., van den Brand J. M. A., Herfst S., Schrauwen E. J. A., Bestebroer T. M., van de Vijver D., Boucher C. A., Koopmans M., Rimmelzwaan G. F., Kuiken T., Osterhaus A. D. M. E., and Fouchier R. A. M., 2009, "Pathogenesis and transmission of swine–origin 2009 A (H1N1) influenza virus in ferrets.," Science, 325(5939), pp. 481–483.

Mustakallio P., Rosenqvist M., Sinai Y., and Kosonen R., 2012, "Full-scale test and CFD-simulation of indoor climate consitions in displacement ventilation case with different room heights and CFD models," Ventilation.

Navy Environmental Health Center, 1992, "Ultraviolet radiation guide," Norfolk, Virginia.

Nazaroff W. W., and Cass G. R., 1987, "Particle deposition from a natural convection flow onto a vertical isothermal flat plate," Journal of Aerosol Science, 18(4), pp. 445–455.

Nieuwstadt F.T.M., 1992, "Turbulentie," Utrecht: Epsilon Uitgaven, The Netherlands.

NIOSH, 1972, "Occupational exposure to ultraviolet radiation; Criteria for a recommended standard," DHEW Publication no. (HSM) 73-11009, U. S. Department of Health, Education, and Welfare, Public Health Service, Rockville, MD.

Noakes C. J., Beggs C. B., and Sleigh P. A., 2004a, "Modelling the performance of upper room ultraviolet germicidal irradiation devices in ventilated rooms: Comparison of analytical and CFD methods," Indoor and Built Environment, 13(6), pp. 477–488.

Noakes C. J., Fletcher L. A., Beggs C. B., Sleigh P. A., and Kerr K. G., 2004b, "Development of a numerical model to simulate the biological inactivation of airborne microorganisms in the presence of ultraviolet light," Journal of Aerosol Science, 35(4), pp. 489–507.

Noakes C. J., Sleigh P. A., Fletcher L. A., and Beggs C. B., 2006, "Use of CFD modelling to optimise the design of upper-room UVGI disinfection systems for ventilated rooms," 15(4), pp. 347–356.

Nuanualsuwan S., Mariam T., Himathongkham S., and Cliver D. O., 2002, "Ultraviolet inactivation of feline calicivirus, human enteric viruses and coliphages," Photochemistry and Photobiology, 76(4), pp. 406–410.

Nuanualsuwan S., and Cliver D. O., 2003, "Capsid functions of inactivated human picornaviruses and feline calicivirus," Applied and Environmental Microbiology, 69(1), pp. 350–357.

Nwachuku N., Gerba C. P., Oswald A., and Mashadi F. D., 2005, "Comparative inactivation of adenovirus serotypes by UV light disinfection," Applied and Environmental Microbiology, 71(9), pp. 5633–5636.

O'Connell P. K., Bucher R. J., Anderson E. P., Cao J. C., Khan S. A., Gostomski V. M., and Valdes J. J., 2006, "Real-time fluorogenic reverse transcription-PCR assays for detection of bacteriophage MS2," Applied and Environmental Microbiology, 72, pp. 478–483.

Olsen S. J., Chang H. L., Cheung T. Y. Y., Tang A. F. Y., Fisk T. L., Ooi S. P. L., Kuo H. W., Jiang D. D. S., Chen K. T., Lando J., Hsu K. H., Chen T. J., and Dowell S. F., 2003, "Transmission of the severe acute respiratory syndrome on aircraft," New England Journal of Medicine, 349, pp. 2416–2422.

Papageorgakis G. C., and Assanis D. N., 1999, "Comparison of linear and nonlinear RNG-based *k*-epsilon models for incompressible turbulent flows," Numerical Heat Transfer, Part B: Fundamentals, 35(1), pp. 1–22.

Patterson M. S., Wilson B. C., and Wyman D. R., 1991, "The propagation of optical radiation in tissue. I. Models of radiation transport and their application," Lasers in Medical Science, 6, pp. 155–168.

Peccia J., Werth H. M., Miller S., and Hernandez M., 2001a, "Effects of relative humidity on the ultraviolet induced inactivation of airborne bacteria," Aerosol Science and Technology, 35, pp. 728–740.

Peccia J., and Hernandez M., 2001b, "Photoreactivation in airborne mycobacterium parafortuitum," Applied and Environmental Microbiology, 67(9), pp. 4225–4232.

Peccia J., and Hernandez M., 2004, "UV-induced inactivation rates for airborne Mycobacterium bovis BCG," Journal of Occupational and Environmental Hygiene, 1(7), pp. 430–435.

Peirson S. N., Butler J. N., and Foster R. G., 2003, "Experimental validation of novel and conventional approaches to quantitative real-time PCR data analysis," Nucleic Acids Research, 31, pp. 73e–73.

Pennell K. G., Aronson A. I., and Blatchley E. R., 2008, "Phenotypic persistence and external shielding ultraviolet radiation inactivation kinetic model," Journal of Applied Microbiology, 104(4), pp. 1192–1202.

Phipps P. R., and Gonda I., 1990, "Droplets produced by medical nebulizers: some factors affecting their size and solute concentration," Chest, 97, pp. 1327–1332.

Piercy T. J., Smither S. J., Steward J. A., Eastaugh L., and Lever M. S., 2010, "The survival of filoviruses in liquids, on solid substrates and in a dynamic aerosol," Journal of Applied Microbiology, 109, pp. 1531–1539.

Placke M. E., Ding J., and William J. Z., 1990 "Inhalation: liquids," Encyclopedia of Pharmaceutical Technology, 2, pp. 1545–1572.

Posner J. D., Buchanan C. R., and Dunn-Rankin D., 2003, "Measurement and prediction of indoor air flow in a model room," Energy and Buildings, 35, pp. 515–526.

Prat S., 1936, "Strahlung und antagonistische wirkungen," Protoplasma, 26, pp. 113–149.

Pruitt K. M., and Kamau D. N., 1993, "Mathematical models of bacterial growth, inhibition and death under combined stress conditions," Journal of Industrical Microbiology and Biotechnology, 12, pp. 221–231.

Public Health Agency of Canada, 2003, "SARS among Ontario health care workers," SARS Epidemiologic Summaries.

Qian H., Li Y., Nielsen P. V., and Huang X., 2009, "Spatial distribution of infection risk of SARS transmission in a hospital ward," Building and Environment, 44, pp. 1651–1658.

Qualls R. G., and Johnson J. D., 1983, "Bioassay and dose measurement in UV disinfection," Applied Microbiology, 45(3), pp. 872–877.

Rahn R. O., Xu P., and Miller S. L., 1999, "Dosimetry of room-air germicidal (254 nm) radiation using spherical actinometry," Photochemistry and Photobiology, 70(3), pp. 314–318.

Rentschler H. C., Nagy R., and Mouromseff G., 1941, "Bactericidal effect of ultraviolet radiation," Journal of Bacteriology, 42, pp. 745–774.

Rechsteiner J., Winkler K. C., 1969, "Inactivation of respiratory suncytial virus in aerosol," Journal of General Virology, 5, pp. 405–410.

Richt J. A., Lager K. M., Clouser D. F., Spackman E., Suarez D. L., and Yoon K. J., 2004, "Real-time reverse transcription-polymerase chain reaction assays for the detection and differentiation of North American swine influenza viruses," Journal of Veterinary Diagnostic Investigation, 16(5), pp. 367–373.

Riley R. L., Wells W. F., Mills C. C., Nyka W., and McLean R. L., 1957, "Air hygiene in tuberculosis: Quantitative studies of infectivity and control in a pilot ward," American Review of Tuberculosis Pulmonary Diseases, 75, pp. 420–431.

Riley R. L., Mills C. C., O'Grady F., Sultan L. U., Wittestadt F., Shivpuri D. N., 1962, "Infectiousness of air from a tuberculosis ward – ultraviolet irradiation of infected air: comparative infectiousness of different patients," American Review of Respiratory Diseases, 85, pp. 511–525.

Riley R. L., and Permutt S., 1971, "Room air disinfection by ultraviolet irradiation of upper air: Air mixing and germicidal effectiveness," Archives of Environmental Health, 22, pp. 208–219.

Riley R. L., and Kaufman J. E., 1972, "Effect of relative humidity on the inactivation of airborne Serratia marcescens by ultraviolet radiation," Applied Microbiology, 23, pp. 1113–1120.

Riley R. L., Knight M., and Middlebrook G., 1976, "Ultraviolet susceptibility of BCG and virulent tubercle bacilli," American Review of Respirotory Disease, 113(4), pp. 413–418.

Riley R. L., and Nardell E. A., 1989, "Clearing the air: The theory and application of ultraviolet disinfection," Review of Respirotory Disease, 139, pp. 1286–1294.

Risco C., Antón I. M., Enjuanes L., and Carrascosa J. L., 1996, "The transmissible gastroenteritis coronavirus contains a spherical core shell consisting of M and N proteins," Journal of Virology, 70(7), pp. 4773–4777.

Rivers T., Gates F., 1928, "Ultra-violet light and vaccine virus. II. The effect of monochromatic ultra-violet light upon vaccine virus," Journal of Experimental Medicine, 47, pp. 45–49.

Rogers D. W. O., Faddegon B. A., Ding G. X., Ma C. M., We J., and Mackie T. R., 1995, "BEAM: A Monte Carlo code to simulate radiotherapy treatment units," Medical Physics, 22(5), pp. 503–524.

Rudnick S., First M., Vincent R., and Brickner P., 2009, "In-place testing of in-duct ultraviolet germicidal irradiation," HVAC&R Research, 15(3), pp. 525–535.

Sagripanti J. L., and Lytle C. D., 2011, "Sensitivity to ultraviolet radiation of Lassa, vaccinia, and Ebola viruses dried on surfaces," Archives of Virology, 156(3), pp. 489–94.

Samad S. A., Bhattacharya S. C., Chatterjee S. N., 1987, "Ultraviolet inactivation and photoreactivation of the cholera phage 'Kappa'," Radiation and Environmental Biophysics, 26, pp. 295–300.

Sattar S. A., Ijaz M. K., and Gerba C. P., 1987, "Spread of viral infections by aerosols," Critical Reviews in Environmental Control, 17(2), pp. 89–131.

Schaffer F. L., Soergel M. E., and Straube D. C., 1976, "Survival of airborne influenza virus: effects of propagating host, relative humidity, and composition of spray fluids," Archives of Virology, 51, pp. 263–273.

Schalk S., Adam V., Arnold E., Brieden K., Voronov A., Witzke H. D., 2006, "UV-lamps for disinfection and advanced oxidation – Lamp types, technologies and applications," IUVA News, 8(1), pp. 32–37.

Scholtissek C., 1994, "Source for influenza pandemics," European Journal of Epidemiology, 10, pp. 455–458.

Scholtissek C., Hinshaw V. S., and Olsen C. W., 1998, "Influenza in pigs and their role as the intermediate host," In: Textbook of Influenza, edited by Nickolson K. G., Webster R. G., and Hay A. J., Blackwell Science, Oxford, UK, pp. 137–145.

Shaman J., and Kohn M., 2009, "Absolute humidity modulates influenza survival, transmission, and seasonality," Proceedings of the National Academy of Sciences of the United States of America, 106(9), pp. 3243–3248.

Shaman J., Pitzer V. E., Viboud C., Grenfell B. T., and Lipsitch M., 2010, "Absolute humidity and the seasonal onset of influenza in the continental United States," PLoS Biology, 8(2), p. e1000316.

Shechmeister I. L., 1950, “Studies on the experimental epidemiology of respiratory infections III. Certain aspects of the behavior of type A influenza virus as an airborne cloud,” Journal of Infectious Diseases, 87, pp. 128–132.

Shen S. C., Wang Y. J., and Chen Y. Y., 2008, “Design and fabrication of medical micro-nebulizer,” Sensors and Actuators A: Physical, 144(1), pp. 135–143.

Shimojo H., 1971, “Multiplicity reactivation of human adenovirus type 12 and simian virus 40 irradiated by ultraviolet light,” Virology, 45, pp. 529–531.

Smerage G. H., and Teixeira A. A., 1993, “Dynamics of heat destruction of spores: a new view,” Journal of Industrical Microbiology and Biotechnology, 12, pp. 211–220.

Sobsey M. D., and Meschke J. S., 2003, “Virus survival in the environment with special attention to survival in sewage droplets and other environmental media of fecal or respiratory origin,” International SARS Symposium, Rome, Italy.

Songer J. R., 1967, “Influence of relative humidity on the survival of some airborne viruses,” Applied Microbiology, 15(1), pp. 35–42.

Sozzi D. A., and Taghipour F., 2006, “UV reactor performance modeling by Eulerian and Lagrangian methods,” Environmental Science and Technology, 40(5), pp. 1609–1615.

Spaan W., Cavanagh D., and Horzinek H. C., 1988, “Coronaviruses: structure and genome expression,” Journal of General Virology, 69, pp. 2939–2952.

Spackman E., Senne A. D., Myers J. T., Bulaga L. L., Garber P. L., Perdue L. M., Lohman K, Daum T. L., and Suarez L. D., 2002, “Development of a real-time reverse transcriptase PCR assay for type A influenza virus and the avian H5 and H7 hemagglutinin subtypes,” Journal of Clinical Microbiology, 40, pp. 3256–3260.

Srebric J., and Chen Q., 2001, “A method of test to obtain diffuser data for CFD modeling of room airflow,” ASHRAE Transactions, 107(2), pp. 108–116.

Srebric J., and Chen Q., 2002, “Simplified numerical models for complex air supply diffusers,” HVAC&R Research, 8(3), pp. 277–294.

Stetzenbach L. D., Buttner M. P., and Cruz P., 2004, “Detection and enumeration of airborne biocontaminants,” Current Opinion in Biotechnology, 15(3), pp. 170–174.

Stuart B. O., 1973, “Deposition of inhaled aerosols,” Aechives of Internal Medicine, 131, pp. 60–73.

Sturm E., Gates F. L., Murphy J. B., 1932, “Properties of the causative agent of a chicken tumor. II. The inactivation of the tumor-producing agent by monochromatic ultra-violet light,” Journal of Experimental Medicine, 55, pp. 441–444.

Summer W., 1962, “Ultraviolet and Infrared Engineering,” Interscience Publishers, Inc., New York.

Sze To G. N., Wan M. P., Chao C. Y. H., Fang L., and Melikov A., 2009, "Experimental study of dispersion and deposition of expiratory aerosols in aircraft cabins and impact on infectious disease transmission," Aerosol Science and Technology, 43(5), pp. 466–485.

Tajima M., 1970, "Morphology of transmissible gastroenteritis virus of pigs," Archives of Virology, 29, pp. 105–108.

Tang J. W., Li Y., Eames I., Chan P. K. S., and Ridgway G. L., 2006, "Factors involved in the aerosol transmission of infection and control of ventilation in healthcare premises," Journal of Hospital Infection, 64(2), pp. 100–114.

Tang J. W., 2009, "The effect of environmental parameters on the survival of airborne infectious agents," Journal of the Royal Society, 6, pp. S737–746.

Tang J. W., Lai, F. Y., Wong F., and Hon K. L., 2010, "Incidence of common respiratory viral infections related to climate factors in hospitalized children in Hong Kong," Epidemiology and Infection, 27, pp. 226–235.

Tarafdar S. P., and Vardya M. S., 1969, "The Rayleigh scattering cross-sections of He, C, N and O", Monthly Notices of the Royal Astronomical Society, 145, pp. 171–180.

Tellier R., 2006, "Review of aerosol transmission of influenza A virus," Emerging Infectious Diseases, 12(11), pp. 1657–1662.

Tennekes H., and Lumley J. L., 1972, "A first course in turbulence," MIT Press, Cambridge, Massachusetts.

Thorne P. S., Kiekhaefer M. S., Whitten P., and Donham K., 1992, "Comparison of bioaerosol sampling methods in barns housing swine," Applied and Environmental Microbiology, 58, pp. 2543–2551.

Thurston-Enriquez J. A., Haas C. N., Jacangelo J., Riley K., and Gerba C. P., 2003, "Inactivation of feline calicivirus and adenovirus type 40 by UV radiation," Applied and Environmental Microbiology, 69(1), pp. 577–582.

Trouwborst T., and de Jong J. C., 1972, "Mechanism of the inactivation of the bacteriophage T1 in aerosols," Applied Microbiology, 23, pp. 938–941.

Trouwborst T., and de Jong J. C., 1973, "Interaction of some factors in the mechanism of inactivation of bacteriophage MS2 in aerosols," Applied Microbiology, 26(3), pp. 252–257.

Tseng C. C., and Li C. S., 2005a, "Collection efficiencies of aerosol samplers for virus-containing aerosols," Aerosol Science, 36, pp. 593–607.

Tseng C. C., and Li C. S., 2005b, "Inactivation of virus-containing aerosols by ultraviolet germicidal irradiation," Aerosol Science and Technology, 39(12), pp. 1136–1142.

Tyrrell D. A. J., 1967, "The spread of viruses of the respiratory tract by the airborne route," Symposia of the Society for General Microbiology, 17, pp. 286–306.

Uemoto K. L., Sato N. M. N., and John V. M., 2010, “Estimating thermal performance of cool colored paints,” Energy and Buildings, 42(1), pp. 17–22.

Ultraviolet radiation guide, 1992, Navy Environmental Health Center, Norfolk, Virginia.

van Elden L. J., Nijhuis M., Schipper P., Schuurman R., and van Loon A. M., 2001 “Simultaneous detection of influenza viruses A and B using real-time quantitative PCR,” Journal of Clinical Microbiology, 39, pp. 196–200.

van Hoeven N., Pappas C., Belser J. A., Maines T. R., Zeng H., Garc á-Sastre A., Sasisekharan R., Katz J. M., and Tumpey T. M., 2009, “Human HA and polymerase subunit PB2 proteins confer transmission of an avian influenza virus through the air,” Proceedings of the National Academy of Sciences of the United States of America, 106(9), pp. 3366–3371.

van Hooff T., Blocken B., van Heijst G. J. F., 2012, “On the suitability of steady RANS CFD for forced mixing ventilation at transitional slot Reynolds numbers,” Indoor Air.

van Osdell D. and Foarde K., 2002, “Defining the effectiveness of UV lamps installed in circulating air ductwork,” Final Report, Air-Conditioning and Refrigeration Technology Institute, Arlington, Virginia.

van Voorthuizen E. M., Ashbolt N. J., and Schäfer A., 2001, “Role of hydrophobic and electrostatic interactions for initial enteric virus retention by MF membranes,” Journal of Membrane Science, 194, pp. 69–79.

Verreault D., Moineau S., and Duchaine C., 2008, “Methods for sampling of airborne viruses,” Microbiology and Molecular Biology Reviews, 72(3), pp. 413–444.

Verstaag H. K., and Malalasekera W., 1995, “An introduction to computational fluid dynamics, the finite volume method,” Prentice-Hall, England.

von Recklinghausen M., 1914, “The ultra-violet rays and their application for the sterilization of water,” Journal of Franklin Institute, 1057–1062, pp. 681–704.

Walker C. M., and Ko G., 2007, “Effect of ultraviolet germicidal irradiation on viral aerosols,” Environmental Science and Technology, 41(15), pp. 5460–5465.

Wan M. P., Sze To G. N., Chao C. Y. H., Fang L., and Melikov A., 2009, “Modeling the fate of expiratory aerosols and the associated infection risk in an aircraft cabin environment,” Aerosol Science and Technology, 43(4), pp. 322–343.

Wang M., and Chen Q., 2009, “Assessment of various turbulence models for transitional flows in enclosed environment,” HVAC&R Research, 15:1099–1119.

Ward M., 1892, “Experiments of the action of light on Bacillus anthracis,” Proceedings of the Royal Society (London), 52, pp. 393–403.

Webb S. J., Bather R., Hodges R. W. 1963, “The effect of relative humidity and inositol on airborne viruses,” Canadian Journal of Microbiology, 9, pp. 87–92.

Weber T. P., and Stilianakis N. I., 2008, "Inactivation of influenza A virus in the environment and modes of transmission: A critical review," Journal of Infection, 57, pp. 361–373.

Weesendorp E., Landman W. J. M., Stegeman A., and Loeffen W. L. A., 2008, "Detection and quantification of classical swine fever virus in air samples originating from infected pigs and experimentally produced aerosols," Veterinary Microbiology, 127, pp. 50–62.

Wehrle P. F., Posch J., Richter K. H., and Henderson D. A., 1970, "An airborne outbreak of smallpox in a German hospital and its significance with respect to other recent outbreaks in Europe," Bulletin of the World Health Organization, 43, pp. 669.

Wells W. F., 1938, "Air-borne infections," Modern Hospital, 51, pp. 66–69.

Wells W. F., 1942a, "Radiant disinfection of air," Archives of Physical Therapy, 23, pp. 143–148.

Wells W. F., Wells M. W., and Wilder T. S., 1942b, "The environmental control of epidemic contagion. I. An epidemiologic study of radiant disinfection of air in day schools," Journal of American Industrial Hygiene Association, 35, pp. 97–121.

Wells W. F., 1955, "Airborne contagion and air hygiene," Harvard University Press, Cambridge, MA.

Whiley D. M., Syrmis M. W., Mackay I. M., and Sloots T. P., 2003, "Detection of influenza type A virus by LightCycler RT-PCR," Austrilian Journal of Medical Science, 24, pp. 136–139.

Whiting R. C., 1991, "Predictive modeling," In: Food Microbiology, edited by Doyle M. P., ASM Press, Washington, pp. 728–739.

Widmark E., 1889, "Uber den e influss des lichtes auf die haut," Hygiea, 3, pp. 1–23.

Wong K. C., and Leung K. S., 2004, "Transmission and prevention of occupational infections in orthopaedic surgeons," Journal of Bone and Joint Surgery America, 86-A(5), pp. 1065–1076.

Wong L. T., Chan W. Y., Mui K. W., and Lai A. C. K., 2010, "An experimental and numerical study on deposition of bioaerosols in a scaled chamber," Aerosol Science and Technology, 44(2), pp. 117–128.

Woo M. H., Hsu Y. M., Wu C. Y., Heimbuch B., and Wander J., 2010, "Method for contamination of filtering facepiece respirators by deposition of MS2 viral aerosols," Journal of Aerosol Science, 41, pp. 944–952.

Wright N. G., and Hargreaves D. M., 2001, "The use of CFD in the evaluation of UV treatment systems," Journal of Hydroinformatics, 3, pp. 59–70.

Xie X., Li Y., Chwang A. T., Ho P. L., and Seto W. H., 2007, "How far droplets can move in indoor environments – revisiting the Wells evaporation-falling curve," Indoor Air, 17(3), pp. 211–225.

Xu J., Liang H., and Kuehn T. H., 1994, "Comparison of numerical predictions and experimental measurements of ventilation in a room," Proceedings Roomvent, Krakow, Poland, 2, pp. 213–227.

Xu P., Peccia J., Fabian P., Martyny J. W., Fennelly K. P., Hernandez M., and Miller S. L., 2003, "Efficacy of ultraviolet germicidal irradiation of upper-room air in inactivating airborne bacterial spores and mycobacteria in full-scale studies," Atmospheric Environment, 37, pp. 405–419.

Xu P., Kujundzic E., Peccia J., Schafer M. P., Moss G., Hernandez M., and Miller S. L., 2005, "Impact of environmental factors on efficacy of upper-room air ultraviolet germicidal irradiation for inactivating airborne Mycobacteria," Environmental Science & Technology, 39, pp. 9656–9664.

Yahya M. T, Cluff C. B., and Gerba C. P., 1993, "Virus removal by slow sand filtration and nanofiltration," International Association on Water Quality, 27(3-4), pp. 445–448.

Yakhot V., and Orszag S. A., 1986, "Renormalization group analysis of turbulence. I. Basic theory," Journal of Scientific Computing, 1(1), pp. 3–51.

Yan W., Zhang Y., Sun Y., and Li D., 2009, "Experimental and CFD study of unsteady airborne pollutant transport within an aircraft cabin mock-up," Building and Environment, 44(1), pp. 34–43.

Yang T., Cropper P. C., Cook M. J., Yousaf R., and Fiala D., 2007, "A new simulation system to predict human-environment thermal interactions in naturally ventilated buildings," Proceedings of the 10th International Conference on Building Simulation (Building Simulation 2007), Tsinghua University, Beijing, China, 3rd-6th September, Paper ID-424, pp. 751–756.

Yang W., Elankumaran S., and Marr L. C., 2011, "Concentrations and size distributions of airborne influenza A viruses measured indoors at a health centre, a day-care centre and on aeroplanes," Journal of the Royal Society, 8(61), pp. 1176–1184.

Yang W., Elankumaran S., and Marr L. C., 2012, "Relationship between humidity and influenza A viability in droplets and implications for influenza's seasonality," PLOS ONE, 7(10), e46789.

Yao M., Zhu T., Li K., Dong S., Wu Y., Qiu X., Jiang B., Chen L., and Zhen S., 2009, "Onsite infectious agents and toxins monitoring in 12 May Sichuan earthquake affected areas," Journal of Environmental Monitoring, 11(11), pp. 1993–2001.

Yee K. S., Carpenter T. E., Farver T. B., and Cardona C. J., 2009, "An evaluation of transmission routes for low pathogenicity avian influenza virus among chickens sold in live bird markets," Virology, 394(1), pp. 19–27.

Yu I. T. S., Li Y., Wong T. W., Phil W. T. M., Chan A. T., Lee J. H. W., Leung D. Y. C., and Ho T., 2004, "Evidence of airborne transmission of the severe acute respiratory syndrome virus," New England Journal of Medicine, 350, pp. 1731–1739.

Yuan X., Chen Q., Glicksman L. R., Hu Y. and Yang X., 1999, "Measurements and computations of room airflow with displacement ventilation," ASHRAE Transactions, 105, pp. 340–352.

Zhang Z., and Chen Q., 2006, "Experimental measurements and numerical simulations of particle transport and distribution in ventilated rooms," Atmospheric Environment, 40(18), pp. 3396–3408.

Zhang Z., and Chen Q., 2007a, "Comparison of the Eulerian and Lagrangian methods for predicting particle transport in enclosed spaces," Atmospheric Environment, 41(25), pp. 5236–5248.

Zhang Z., Zhai Z. Q., Zhang W., and Chen Q., 2007b, "Evaluation of various turbulence models in predicting airflow and turbulence in enclosed environments by CFD: Part 2 – Comparison with experimental data from literature," HVAC&R Research, 13: pp. 871–886.

Żuk T., Rakowski F., and Radomski J. P., 2009, "A model of influenza virus spread as a function of temperature and humidity," Computational Biology and Chemistry, 33(2), pp. 176–180.

Zuo Z., Kuehn T. H., Verma H., Kumar S., Goyal S. M., Appert J., Raynor P. C., Ge S., and Pui D. Y. H., 2013, "Association of airborne virus infectivity and survivability with its carrier particle size," Aerosol Science and Technology, 47(4), pp. 373–382.

Appendix A. Sampling efficiency

Two sampling setups were used in this study. For the filter tests, two sampling probes were installed in the test duct, and air was sampled perpendicular to the main flow direction. For the remaining tests, one sampling probe was installed facing upward when sampling the almost still chamber air. For the filter tests, velocity magnitudes upstream and downstream of the filter were also different. Overall, all sampling was performed anisokinetically, and should be evaluated separately for particle sampling efficiency.

Impaction, turbulent deposition, and sedimentation on internal surfaces are the major mechanisms for particle loss in sampling inlets and tubing (Liu 1981; McFarland 1997; Kumar 2008). To determine their effects, velocity ratio and Stokes number are the most important parameters (Durham 1980; Liu 1981; Okazaki 1987a). Velocity ratio is defined as ambient velocity divided by sampling velocity. Stokes number (*Stk*) is defined as:

$$Stk = \tau \frac{U_0}{D_s} = \frac{C_c \rho_p d_p^2}{18\mu} \cdot \frac{U_0}{D_s}, \quad \text{(A1)}$$

where τ is the relaxation time of a particle, U_0 is the ambient velocity, D_s is the inside diameter of the sampling probe, C_c is the Cunningham correction factor, ρ_p is the particle density, d_p is the particle diameter, and μ is the fluid viscosity. Sampling losses will be discussed in three parts. Each part corresponds to one of the three components of the total sampling efficiency: aspiration efficiency ($E_{aspiration}$), entry efficiency (E_{entry}), and transport efficiency ($E_{transport}$) (Liu 1981; Okazaki 1987a, 1987b; Hangal 1990a):

$$E_{total} = E_{aspiration} E_{entry} E_{transport}. \quad \text{(A2)}$$

Aspiration efficiency

Aspiration loss is mainly due to particles in the sampled flow that do not enter the sampling inlet, caused by curved streamlines near the sampling inlet for anisokinetic sampling. For misaligned sampling, the higher the ambient velocity or the larger the particles, the lower the aspiration efficiency becomes (Durham 1980; Okazaki 1987a). If the sampling-from-still-air criterion is met,

the aspiration loss can be neglected. The criterion is met when the ambient velocity is below the threshold value for a specified particle size (Hinds 1999). Assuming a particle density of 1000 kg/m^3 and air properties at normal conditions, the maximum allowable ambient velocities for the particle sizes representing the impactor stages are listed in TABLE A1.

TABLE A1 Maximum ambient air velocity according to the sampling-from-still-air requirement.

Impactor stage	0	1	2	3	4	5	6	7
Geomean stage size [μm]	9.49	7.22	5.22	3.94	2.63	1.52	0.88	0.53
Stokes number	0.058	0.034	0.018	0.010	0.005	0.002	<0.001	<0.001
Max velocity ratio	0.85	1.22	1.87	2.70	4.57	9.25	18.32	33.82

For the filter tests, the velocity measured at the upstream sampling location or at the downstream location when no filter was installed was about 425 ft/min (2.2 m/s). The average velocity measured downstream of a filter was about 575 ft/min (2.9 m/s). The sampling velocity through the sampling probe (ID=0.694 in=1.763 cm) was about 1.9 m/s. Thus the corresponding velocity ratios were 1.16 and 1.53, respectively. According to TABLE A1, impactor stage 0 did not meet the criterion for both locations, and impactor stage 1 did not meet the criterion for sampling downstream of a filter.

TABLE A2 Aspiration efficiency [%] for each impactor stage for filter tests.

Impactor stage	0	1	2	3	4	5	6	7
Geomean stage size [μm]	9.49	7.22	5.22	3.94	2.63	1.52	0.88	0.53
Filter upstream and correlation	87.8	92.7	96.0	97.6	98.9	99.6	99.8	99.9
Filter downstream	74.1	83.1	89.9	93.5	96.5	98.5	99.3	99.7

Calculation of the aspiration efficiency for each impactor stage was based on the published equation in Hangal 1990a and 1990b, and the result is shown in TABLE A2. The results agree with the sampling-from-still-air criterion in that the aspiration efficiency was generally greater than 90% for impactor stages 2-7 when downstream of a filter, and for impactor stages 1-7 in the other cases of the filter tests. Other than the filter tests, sampling velocity was 3.6 m/s, and the air velocity was lower than 0.5 m/s by CFD simulation (Chapter 7). The velocity ratio was therefore

smaller than 0.14. From TABLE A1, the sampling-from-still-air criterion was met for all impactor stages. No equation for calculating the aspiration efficiency in this case was found, thus the aspiration efficiency was assumed to be 100% for all impactor stages.

Entry efficiency

Less than 100% E_{entry} is due to particle impaction on the front wall of the sampling inlet. The loss can be neglected if the sharp-edged-inlet criterion is met (Hangal 1990a, 1990b). The criterion is met when the outside diameter (OD) divided by the inside diameter (ID) of the sampling probe is smaller than 1.1, or if the probe wall thickness divided by inside diameter is smaller than 0.5, and the wall taper is smaller than 15 degrees.

For the filter tests, each sampling probe's ID was 0.694 in (1.76 cm), and OD was 0.75 in (1.91 cm), thus the ratio was 1.08, satisfying the criterion. For the other tests, the sampling probe's ID was 0.5 in (1.27 cm), and OD was 0.75 in (1.91 cm), so the criterion was not met. However, as the ambient air velocity was very low near the sampling location, particle impaction onto the front wall of sampling inlet due to inertia could be neglected. Therefore, 100% entry efficiency was assumed for all sampling setups.

Transport efficiency

In the chamber tests, 0.5 in (1.27 cm) ID Tygon tubing was used to connect the impactor with its corresponding sampling probe. The Reynolds number in the Tygon tubing was about 3000 at 28.3 l/min sampling flow rate, indicating a transitional flow regime. Particle loss equations for turbulent flow were therefore used for conservative estimation. Major mechanisms of transport loss are discussed below separately. Unless pointed out, all the equations are from Hinds 1999, Chapter 10, Section 3: Transport losses.

Bend loss

Particle loss may happen at bends in the sampling line. Curvature ratio, Reynolds number, particle size, and tube flattening are important factors. Curvature ratio and Reynolds number can be combined as the Dean number (*D*), which was defined as:

$$D = \frac{Re}{\sqrt{R}}, \tag{A3}$$

where *R* is curvature ratio, which is defined as bend radius divided by tubing radius. Its effect is negligible when greater than 5. At large curvature ratio, the Reynolds number does not have significant effect either (Cheng 1975; Cheng 1981; Pui 1987; McFarland 1997; Peters 2004). For the chamber test setup, all curvature ratios were much larger than 5, and tube flattening due to bending was negligible. All sampling setups had roughly two 90 degree bends. The bend loss for particles collected by each impactor stage was calculated assuming turbulent flow, and is shown in TABLE A3. Particles collected on impactor stages 4-7 had bend losses less than 10%, with stage 3 slightly larger than 10%.

TABLE A3 Penetration through two 90 degree bends.

Impactor stage	0	1	2	3	4	5	6	7
Geomean stage size [μm]	9.49	7.22	5.22	3.94	2.63	1.52	0.88	0.53
For turbulent flow	0.701	0.813	0.897	0.939	0.972	0.990	0.996	0.999
For two bends	0.491	0.662	0.804	0.882	0.945	0.980	0.993	0.997

Contraction loss

One contraction fitting was used for each sampling line in the filter tests. It was from the 0.694 in (1.76 cm) ID sampling probe to 0.5 in (1.27 cm) ID Tygon tubing. No contraction fitting was used for the other tests. No expansion fitting was used in any of the setups. Particle loss in a contraction fitting is due to flow separation, and is a function of inlet and outlet areas, contraction half angle, Stokes number, and Re (Muyshondt 1996). The penetration through the contraction fitting used in the chamber tests was estimated to be greater than 99.5% for particles collected on all impactor stages, thus the contraction loss was neglected.

Loss due to gravitational settling

Particles moving in sampling lines may deposit on tubing walls due to gravitational settling. This effect depends on particle size, tube length, and tube inclination angle (Hinds 1999). In the filter tests, the tubing was 50 in (1.27 m) long and on a 0.611 rad inclination. In the other tests, the tubing was 53 in (1.35 m) long and was roughly horizontal. The results are shown in TABLE A4.

TABLE A4 Penetration due to gravitational settling.

Impactor stage	0	1	2	3	4	5	6	7
Geomean stage size [μm]	9.49	7.22	5.22	3.94	2.63	1.52	0.88	0.53
Filter tests	0.929	0.958	0.978	0.987	0.994	0.998	0.999	1.000
Other tests	0.914	0.949	0.973	0.984	0.993	0.998	0.999	1.000

Losses due to diffusion, interception, turbulence, thermophoresis, and electrostatic attraction

Diffusion loss is greater for smaller particles, and is affected by flow regime. Calculations were thus based on 0.4 μm diameter particles, which was the lower limit of the impactor collection size. Calculations were conducted for both laminar and turbulent flows. The diffusion loss was always less than 0.1%.

Interception loss occurs when the particle path is too close to the tubing wall. Generally, this may happen near the sampling inlet. Since the particles in this study were extremely small (<10 μm) compared to tubing ID (>1.2 cm), this effect was neglected.

Turbulence may enhance particle loss in sampling lines, since larger particles with greater inertia may penetrate the laminar boundary layer and impact on the tubing wall (Hinds 1999). In this study, since the turbulence was not strong for a Reynolds number of about 3000, and the particle inertia was small, this effect was neglected.

Particle deposition can be affected due to temperature difference, which is called thermophoresis. Generally, deposition is enhanced when the wall is cooler than ambient, and is reduced when the wall is warmer. In this study, the tubing wall temperature should be the same as the inside air

flow temperature due to the steady state isothermal test conditions. Therefore, thermophoretic losses were ignored.

Particles may also deposit on tubing walls due to electrostatic attraction. This effect depends on tubing material. Teflon or Polyfio tubing can be easily charged by bending, but the surface electrical field is almost zero for Tygon or conductive metal tubing (Liu 1985). As the particles usually carry charge, they can also be attracted to neutral surfaces by image forces, but this effect is very weak, and the particles need to be very close to the tubing wall (Hinds 1999). In this study, the sampling tubing was mainly Tygon or metal, thus this effect was neglected.

Overall sampling efficiency

From the above discussion, the most important losses were due to aspiration, bending of the sampling tubing, and gravitational settling. The individual effects of the above mechanisms can be multiplied to calculate total penetration or sampling efficiency. The total efficiencies are shown in TABLE A5 for each of the three cases.

TABLE A5 Total sampling efficiencies [%] for all sampling situations.

Impactor stage	0	1	2	3	4	5	6	7
Geomean stage size [µm]	9.49	7.22	5.22	3.94	2.63	1.52	0.88	0.53
Stokes number	0.058	0.034	0.018	0.010	0.005	0.002	<0.001	<0.001
Filter downstream	33.8	52.7	70.7	81.4	90.6	96.3	98.5	99.4
Other filter tests	40.0	58.8	75.5	85.0	92.9	97.4	99.0	99.6
Other tests	44.9	62.8	78.2	86.8	93.8	97.8	99.2	99.7

In summary, for the filter tests, particles collected on impactor stages 3-7 (0.4-4.7 µm) had sampling efficiencies greater than 80%, and those collected on impactor stages 4-7 (0.4-3.3 µm) had efficiencies greater than 90%. For the other tests without the filter duct installed, particles collected on impactor stages 3-7 had sampling efficiencies greater than 85%, and those collected on impactor stages 4-7 had efficiencies greater than 90%. The sampling efficiencies were acceptable for this study, even though the test results may not represent the true particle size

distribution in the chamber. The sampling efficiency downstream of a filter was calculated based on the average of the measured velocities. Due to the complex flow field downstream of a filter, the actual sampling efficiencies might be different. The difference between the upstream and downstream sampling efficiencies was not corrected by the correlation tests. This might be one of the error sources for the filtration efficiency results.

References

Cheng Y., and Wang C., 1975, "Inertial deposition of particles in a bend," Journal of Aerosol Science, 6(2), pp. 139–145.

Cheng Y., and Wang C., 1981, "Motion of particles in bends of circular pipes," Atmospheric Environment, 15, pp. 301–306.

Durham M. D., and Lundgren D. A., 1980, "Evaluation of aerosol aspiration efficiency as a function of stokes number, velocity ratio and nozzle angle," Journal of Aerosol Science, 11(2), pp. 179–188.

Hangal S., and Willeke K., 1990a, "Aspiration efficiency: Unified model for all forward sampling angles," Environmental Science and Technology, 24(5), pp. 688–691.

Hangal S., and Willeke K., 1990b, "Overall efficiency of tubular inlets sampling at 0–90 degrees from horizontal aerosol flows," Atmospheric Environment. Part A. General Topics, 24(9), pp. 2379–2386.

Hinds W. C., 1999, "Aerosol technology," 2nd edition, Wiley-Interscience, New York, NY.

Kumar P., Fennell P., Symonds J., and Britter R., 2008, "Treatment of losses of ultrafine aerosol particles in long sampling tubes during ambient measurements," Atmospheric Environment, 42(38), pp. 8819–8826.

Liu B. Y. H., and Pui D. Y. H., 1981, "Aerosol sampling inlets and inhalable particles," Atmospheric Environment, 15, pp. 589–600.

Liu B. Y. H., Pui D. Y. H., Rubow K. L., and Szymanski W. W., 1985, "Electrostatic effects in aerosol sampling and filtration," Annals of Occupational Hygiene, 29(2), pp. 251–269.

McFarland A. R., Gong H., Muyshondt A., Wente W. B., and Anand N. K., 1997, "Aerosol deposition in bends with turbulent flow," Environmental Science and Technology, 31(12), pp. 3371-3377

Muyshondt A., Mcfarland A. R., and Anand N. K., 1996, "Deposition of aerosol particles in contraction fittings," Aerosol Science and Technology, 24, pp. 205–216.

Okazaki K., Wiener R. W., and Willeke K., 1987a, "Non-isoaxial aerosol sampling: mechanisms controlling the overall sampling efficiency," Environmental Science and Technology, 21(2), pp. 183–187.

Okazaki K., Wiener R. W., and Willeke K., 1987b, "The combined effect of aspiration and transmission on aerosol sampling accuracy for horizontal isoaxial sampling," Atmospheric Environment, 21(5), pp. 1181–1185.

Peters T. M., and Leith D., 2004, "Particle deposition in industrial duct bends," Annals of Occupational Hygiene, 48(5), pp. 483–490.

Pui D. Y. H., Romay-Novas F., and Liu B. Y. H., 1987, "Experimental study of particle deposition in bends of circular cross section," Aerosol Science and Technology, 7, pp. 301–315.

Strom L., 1972, "Transmission efficiency of aerosol sampling lines," Atmospheric Environment, 6, pp. 133–142.

Appendix B. Average residence time

The average aerosol residence time from injection to sampling location was measured with an optical particle counter (OPC) (Lasair 1002, Particle Measuring Systems, Inc., Boulder, CO). The four OPC channels used for particle counting are listed in TABLE B1. The first channel (0.3-0.4 μm) was not used as its range was not studied for viral aerosols. The last channel (>2 μm) was not used either, as its particle count was very small.

TABLE B1 The four OPC channels used for the residence time measurement.

Channel [μm]	0.4-0.5	0.5-0.7	0.7-1.0	1.0-2.0
Geomean [μm]	0.447	0.592	0.837	1.414

The residence time measured in this experiment was for a chamber ventilation rate of 15 ACH or 53 ft^3/min (1500 l/min), which was always used except in the HVAC filter tests. In this study, the chamber was always run isothermally, meaning that the temperatures of supply air and chamber boundaries were the same. However, operation of the vacuum pump and the two humidifiers might slightly affect the flow field for different thermal conditions. Measurements were thus taken under all five conditions (TABLE B2) used in this study. Four repeat runs were carried out for each condition.

TABLE B2 Conditions for residence time measurement.

Condition	1	2	3	4	5
Temp [˚C]	25	25	25	30	30
RH [%]	38	50	66	38	50
AH [g/m^3]	8.8	11.5	15.2	11.5	15.2

The experiment was performed using the same setup as in the viral aerosol tests except for two differences: the nebulizer fluid did not contain any virus, and the OPC was attached to the sampling tubing to draw a small amount of sampled air for concentration measurement. After injection started, the concentration measured by the OPC first increased, and then gradually

leveled off, depicting a step-up response. The increasing part was used to calculate the residence time. Concentration measurement was taken at 0, 1, 2, 3, 5, 7, and 10 min after injection started. 0 min measurement was the background concentration, and was used to subtract from the concentration at the other time points. The data points of each run were best fitted with the "DoseResp" (dose response) curve in Origin 8 (OriginLab Corp., Northampton, MA) with the form:

$$C = A_1 + \frac{A_2 - A_1}{1+10^{(LOGt_0 - t)p}}, \quad \text{(B1)}$$

where C is the particle concentration measured by OPC, and t is the time from the start of measurement. A_1, A_2, t_0, and p are the four coefficients determined by curve fitting (FIGURE B1). Due to subtraction of the background concentration at time 0, A_1 must be 0. To calculate the average residence time, the step-up equation was used:

$$Average\ residence\ time = \int_0^\infty \left(1 - \frac{C}{A_2}\right) dt = \int_0^\infty \left(1 - \frac{1}{1+10^{(LOGt_0 - t)p}}\right) dt. \quad \text{(B2)}$$

Individual curve fitting in Origin 8 and numerical integration in MATLAB 7.1 (The Mathworks, Inc.) were performed to calculate the residence time for each run. Then, statistical analysis was carried out for average residence time and its standard error. ANOVA was also carried out to look for significant factors.

Since the residence time measured by the OPC was the total time spent by aerosol in the chamber and in the sampling tubing, the time spent in the tubing must be subtracted from the total time to get the actual residence time in the chamber environment. The time spent in each section of the tubing could be calculated by dividing the volume of the tubing section with the corresponding volumetric flow rate. The total time spent in both injection and sampling tubing was about 30.5 s. Moreover, the OPC measured the average particle concentration of past 10 s, which was equivalent to a delay of 5 s in measurement. Considering both offsets, the final correction should be 35.5 s, which was subtracted from the numerical integration result.

By ANOVA, the particle size distribution did not significantly depend on time (from 0 to 10 min) (channel $p<0.001$, time $p<0.001$, size*time $p=0.523$), thus the residence time could be considered independent of particle size from 0.4 to 2 μm. The average residence time of particles from the

injection outlet to the sampling inlet was found to be 126+/-6 s, which did not depend on temperature (p=0.753), RH (p=0.513), or AH (p=0.665).

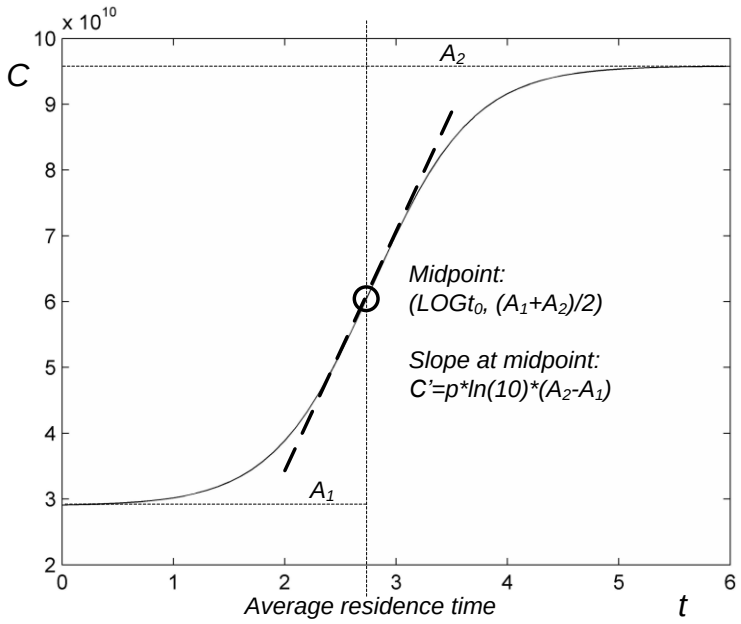

FIGURE B1 Step-up response for the calculation of average residence time of sampled particles.

Appendix C. Demonstration of data reduction for virus relative recovery and survival

The data reduction from raw data of live virus (LV) titer, total virus (TV) concentration, and fluorescence intensity (FI) to relative recovery and survival was similar for all tests. As a demonstration, the calculation procedure for MS2 at 25 ˚C, 50% RH without UVGI is presented. The tests were carried out on 06/04, 06/05, and 06/08, 2012. The live virus raw data in PFU/100 µl and normalized live virus titers are listed in TABLE C1. For the other viruses the unit used TCID50/100 µl instead of PFU/100 µl. In TABLE C1, the rows from "Impactor stage 0" to "Nebulizer post" are the raw data corresponding to stage and nebulizer samples. Geometric mean of "pre" and "post" nebulizer samples was first calculated for normalization of stage samples. The normalization was done by dividing an impactor stage value with the geometric mean of "pre" and "post". As uncertainty was assumed to be symmetric about the mean on a logarithmic scale, the normalized live virus titers were firstly converted to a logarithmic scale, and then the mean and standard deviation were calculated for the three repeats as shown in TABLE C2.

TABLE C1 LV raw data in [PFU/100 µl] and normalized LV (dimensionless) on the normal scale.

Date	**06/04**	**06/05**	**06/08**
Impactor stage 0	2.78E+06	7.20E+06	1.41E+03
Impactor stage 1	3.61E+06	5.80E+06	1.92E+03
Impactor stage 2	1.02E+07	1.72E+07	1.86E+03
Impactor stage 3	1.08E+08	7.80E+07	2.40E+04
Impactor stage 4	2.92E+08	2.12E+08	1.62E+04
Impactor stage 5	3.71E+08	2.47E+08	6.00E+04
Impactor stage 6	1.36E+08	1.18E+08	1.55E+04
Impactor stage 7	3.02E+07	2.52E+07	2.73E+03
Nebulizer "pre"	1.06E+10	1.07E+10	2.17E+06
Nebulizer "post"	1.20E+10	1.27E+10	3.43E+06
Geomean of "pre" and "post"	1.13E+10	1.17E+10	2.73E+06

Date	06/04	06/05	06/08
Normalized impactor stage 0	2.46E-04	6.18E-04	5.17E-04
Normalized impactor stage 1	3.20E-04	4.98E-04	7.04E-04
Normalized impactor stage 2	9.04E-04	1.48E-03	6.82E-04
Normalized impactor stage 3	9.58E-03	6.69E-03	8.80E-03
Normalized impactor stage 4	2.58E-02	1.82E-02	5.94E-03
Normalized impactor stage 5	3.29E-02	2.12E-02	2.20E-02
Normalized impactor stage 6	1.21E-02	1.01E-02	5.68E-03
Normalized impactor stage 7	2.68E-03	2.16E-03	1.00E-03

TABLE C2 Mean and standard deviation of normalized LV of impactor samples on a log-scale.

Statistic	Mean	Standard deviation
Normalized impactor stage 0	-3.36804	0.21155
Normalized impactor stage 1	-3.31683	0.17149
Normalized impactor stage 2	-3.01369	0.16964
Normalized impactor stage 3	-2.08299	0.08136
Normalized impactor stage 4	-1.85141	0.33357
Normalized impactor stage 5	-1.60483	0.10593
Normalized impactor stage 6	-2.05299	0.17104
Normalized impactor stage 7	-2.74571	0.22483

Figures were plotted after converting the mean and uncertainty back to the normal scale. Note that the uncertainty converted back to the normal scale was not symmetric about the mean. Similar processes were performed for the total virus concentration (TABLES C3 and C4) and fluorescence intensity (TABLES C5 and C6).

TABLE C3 TV raw data in [PFU/100 µl] and normalized TV (dimensionless) on the normal scale.

Date	06/04	06/05	06/08
Impactor stage 0	3.14E+07	7.50E+07	5.04E+05
Impactor stage 1	3.53E+07	1.41E+08	6.93E+05
Impactor stage 2	9.45E+07	1.35E+08	7.73E+05
Impactor stage 3	4.69E+08	6.84E+08	3.95E+06
Impactor stage 4	1.04E+09	1.83E+09	1.11E+07

Date	06/04	06/05	06/08
Impactor stage 5	1.87E+09	2.98E+09	1.65E+07
Impactor stage 6	7.73E+08	1.30E+09	1.02E+07
Impactor stage 7	1.75E+08	2.42E+08	2.82E+06
Nebulizer “pre”	1.92E+10	3.86E+10	2.73E+08
Nebulizer “post”	1.66E+10	4.48E+10	4.54E+08
Geomean of “pre” and “post”	1.78E+10	4.16E+10	3.52E+08
Normalized impactor stage 0	1.76E-03	1.80E-03	1.43E-03
Normalized impactor stage 1	1.98E-03	3.39E-03	1.97E-03
Normalized impactor stage 2	5.30E-03	3.23E-03	2.19E-03
Normalized impactor stage 3	2.63E-02	1.64E-02	1.12E-02
Normalized impactor stage 4	5.82E-02	4.39E-02	3.14E-02
Normalized impactor stage 5	1.05E-01	7.17E-02	4.70E-02
Normalized impactor stage 6	4.34E-02	3.12E-02	2.88E-02
Normalized impactor stage 7	9.82E-03	5.81E-03	7.99E-03

TABLE C4 Mean and standard deviation of normalized TV of impactor samples on a log-scale.

Statistic	Mean	Standard deviation
Normalized impactor stage 0	-2.78092	0.05557
Normalized impactor stage 1	-2.62609	0.13590
Normalized impactor stage 2	-2.47487	0.19195
Normalized impactor stage 3	-1.77142	0.18563
Normalized impactor stage 4	-1.36511	0.13410
Normalized impactor stage 5	-1.15084	0.17441
Normalized impactor stage 6	-1.46960	0.09419
Normalized impactor stage 7	-2.11385	0.11495

TABLE C5 FI raw data (dimensionless) and normalized FI (dimensionless) on the normal scale.

Date	06/04	06/05	06/08
Impactor stage 0	5.15E+02	4.84E+02	2.65E+02
Impactor stage 1	6.04E+02	6.90E+02	3.34E+02
Impactor stage 2	1.60E+03	1.63E+03	8.20E+02
Impactor stage 3	9.82E+03	7.87E+03	5.66E+03

Date	06/04	06/05	06/08
Impactor stage 4	2.32E+04	2.15E+04	1.49E+04
Impactor stage 5	3.74E+04	3.08E+04	2.54E+04
Impactor stage 6	1.47E+04	1.31E+04	9.71E+03
Impactor stage 7	2.54E+03	2.68E+03	1.68E+03
Nebulizer “pre”	5.96E+05	5.38E+05	8.19E+05
Nebulizer “post”	9.45E+05	9.27E+05	7.43E+05
Geomean of “pre” and “post”	7.51E+05	7.06E+05	7.80E+05
Normalized impactor stage 0	6.86E-04	6.86E-04	3.40E-04
Normalized impactor stage 1	8.04E-04	9.77E-04	4.28E-04
Normalized impactor stage 2	2.13E-03	2.31E-03	1.05E-03
Normalized impactor stage 3	1.31E-02	1.11E-02	7.25E-03
Normalized impactor stage 4	3.09E-02	3.05E-02	1.90E-02
Normalized impactor stage 5	4.98E-02	4.36E-02	3.26E-02
Normalized impactor stage 6	1.96E-02	1.86E-02	1.24E-02
Normalized impactor stage 7	3.39E-03	3.79E-03	2.16E-03

TABLE C6 Mean and standard deviation of normalized FI of impactor samples on a log-scale.

Statistic	Mean	Standard deviation
Normalized impactor stage 0	-3.26543	0.17588
Normalized impactor stage 1	-3.15770	0.18737
Normalized impactor stage 2	-2.76164	0.18845
Normalized impactor stage 3	-1.99198	0.13258
Normalized impactor stage 4	-1.58203	0.11986
Normalized impactor stage 5	-1.38340	0.09401
Normalized impactor stage 6	-1.78147	0.10782
Normalized impactor stage 7	-2.51924	0.12971

After the normalized LV, normalized TV, and normalized FI are calculated for these samples, their virus relative recovery (RR) and survival can be eventually determined using the following equations:

$$RR = \frac{(\frac{Stage}{Nebulizer})_{LV}}{(\frac{Stage}{Nebulizer})_{FI}} = \frac{Normalized\ LV}{Normalized\ FI}, \quad \text{(C1)}$$

$$Survival = \frac{(\frac{Stage}{Nebulizer})_{LV}}{(\frac{Stage}{Nebulizer})_{TV}} = \frac{Normalized\ LV}{Normalized\ TV}. \quad \text{(C2)}$$

The virus relative recovery and survival results are shown in TABLES C7 and C8. The data respectively correspond to FIGURES 5.3.7 and 5.3.9 in Chapter 5.

TABLE C7 Mean and standard deviation of virus relative recovery (dimensionless) of impactor samples.

Statistic	**Mean (log scale)**	**Mean (normal scale)**	**Standard deviation (log scale)**
Impactor stage 0	-0.10261	0.78956	0.31703
Impactor stage 1	-0.15912	0.69323	0.32919
Impactor stage 2	-0.25206	0.55969	0.10449
Impactor stage 3	-0.09102	0.81093	0.15763
Impactor stage 4	-0.26938	0.53780	0.21747
Impactor stage 5	-0.22143	0.60058	0.07980
Impactor stage 6	-0.27152	0.53516	0.06513
Impactor stage 7	-0.22648	0.59364	0.11637

TABLE C8 Mean and standard deviation of virus survival (dimensionless) of impactor samples.

Statistic	**Mean (log scale)**	**Mean (normal scale)**	**Standard deviation (log scale)**
Impactor stage 0	-0.58711	0.25875	0.23198
Impactor stage 1	-0.69073	0.20383	0.21279
Impactor stage 2	-0.53882	0.28919	0.21519
Impactor stage 3	-0.31157	0.48801	0.18019
Impactor stage 4	-0.48630	0.32636	0.20596
Impactor stage 5	-0.45399	0.35157	0.10864
Impactor stage 6	-0.58338	0.26098	0.11064
Impactor stage 7	-0.63186	0.23342	0.24377

Appendix D. Uncertainty analysis

Basic uncertainties

For N samples being studied, each one is denoted by x_i, and their mean is $\bar{x}$. Standard deviation (*Stdev*) shows how dispersed the data set is about the mean:

$$Stdev = \sqrt{\frac{\sum_{i=1}^{N}(x_i - \bar{x})^2}{N-1}}. \quad \text{(D1)}$$

Relative standard deviation (*RelStdev*) or coefficient of variation (CV or COV) is:

$$RelStdev(\%) = \frac{Stdev}{\bar{x}} \times 100\%. \quad \text{(D2)}$$

Standard error (*Stderr*) of the mean tells how far the sample mean is from the true mean:

$$Stderr = \frac{Stdev}{\sqrt{N}}. \quad \text{(D3)}$$

Relative standard error (*RelStderr*) is defined similarly as *RelStdev*:

$$RelStderr(\%) = \frac{Stderr}{\bar{x}} \times 100\%. \quad \text{(D4)}$$

Two-sided 95% confident interval was used for γ calculation for virus inactivation in the nebulizer. It is defined as the interval inside which the actual value could be on a 95% probability (frequency), or where the true mean could be on a 95% confidence level. To calculate the confidence interval, variance distribution is assumed to be normal. For log normal distribution as in the current study, the calculation was done on a logarithmic scale. To calculate the confidence interval, a t-distribution table is used to get the upper and lower limits of the interval:

$$Upper\ confidence\ limit = \bar{x} + t_{a,N-1}\frac{Stdev}{\sqrt{N}}, \quad \text{(D5)}$$

$$Lower\ confidence\ limit = \bar{x} - t_{a,N-1}\frac{Stdev}{\sqrt{N}}, \quad \text{(D6)}$$

where the subscript a is confidence level which is 0.95 (two-sided) for this case, and $t_{a,N-1}$ is the value obtained from the t-table based on a and $N-1$ (degree of freedom). Confidence interval is expressed as [*Lower confidence limit*, *Upper confidence limit*].

Pooled relative standard deviation

Uncertainties from different tests can sometimes be assumed to be identical. For example, the uncertainty of impactor stage 5 can be assumed constant for different humidity levels. In this case, the different uncertainties can be pooled together to calculate a single one to represent all similar tests. Usually, tests with a small number of repeats benefit from this process by getting more accurate uncertainties for further analysis. This applies to the current study since only triplicate tests were conducted.

Suppose a result contains three sets of data: *A*, *B*, and *C*. Each data set has N_A, N_B, and N_C number of repeats respectively. On a logarithmic scale, their mean values are *a*, *b*, and *c*, and their standard deviations are $Stdev_A$, $Stdev_B$, and $Stdev_C$. If their uncertainties can be assumed to be identical, the pooled standard deviation ($Stdev_{pool}$) on a logarithmic scale is:

$$Stdev_{pool} = \sqrt{\frac{\sum_{i=A,B,C}((N_i-1)\times Stdev_i^2)}{\sum_{i=A,B,C}(N_i-1)}}. \quad \text{(D7)}$$

As $Stdev_{pool}$ is on a logarithmic scale, converting the standard deviation back to the normal scale makes the uncertainty asymmetric about the mean:

$$RelStdev_{upper} = \frac{10^{m+Stdev_{pool}}-10^m}{10^m} = 10^{Stdev_{pool}} - 1, \quad \text{(D8)}$$

$$RelStdev_{lower} = \frac{10^m-10^{m-Stdev_{pool}}}{10^m} = 1 - 10^{-Stdev_{pool}}, \quad \text{(D9)}$$

where *m* is the mean of any set of the samples: *a*, *b*, or *c*. $RelStdev_{upper}$ and $RelStdev_{lower}$ are relative standard deviations on the upper and lower sides of the mean respectively.

Propagated uncertainty

To calculate the uncertainty (*U*) associated with a derived quantity (*Y*) such as relative recovery or filtration efficiency, the uncertainties of all independent variables (X_1, X_2 …) in the original equation need to be combined as:

$$U_Y = \sqrt{(\frac{\partial Y}{\partial X_1}U_{X_1})^2 + (\frac{\partial Y}{\partial X_2}U_{X_2})^2 + \cdots}. \quad \text{(D10)}$$

Particularly, for simple cases in the form of $C=A+B$:

$$U_C = \sqrt{U_A^2 + U_B^2}. \quad \text{(D11)}$$

For the relationship of $C=A/B$:

$$U_C = C\sqrt{(\frac{U_A}{A})^2 + (\frac{U_B}{B})^2}. \quad \text{(D12)}$$

Appendix E. Measurement repeatabilities

In this study, live virus was measured with cell-culture based titration, total virus was measured with PCR, and fluorescein was measured with a spectrofluorometer. In the viral aerosol results, the variation of fluorescence intensity was the smallest, and that of live virus titer was the largest. To further investigate the repeatability of each measuring method, a test was conducted. In the test, samples of MS2, AIV, and HAdV-1 were divided into similar aliquots, and diluted to different concentrations to simulate impactor and nebulizer samples. The relative standard deviation of 9 repeats for each case was calculated for the uncertainty associated with any single measurement (TABLE E1).

TABLE E1 Relative standard deviations [%] of 9 repeats for live virus titer, total virus concentration, and fluorescence intensity.

MS2		HAdV-1		AIV		Fluorescein	
Live	Total	Live	Total	Live	Total	Impactor	Nebulizer
+28/-22	+29/-22	+72/-42	+27/-21	+64/-39	+36/-27	+3/-2	+45/-31

The repeatabilities in TABLE E1 generally agree with the viral aerosol test results. For live virus, HAdV-1 and AIV had larger uncertainties than MS2, which had similar uncertainties for live virus and total virus. The greater uncertainties with the two animal viruses were most likely due to the low resolution in their raw data, where only three data points were used per 1-log range. For total virus, the repeatability did not seem to depend on virus or suspension, even though the PCR procedure for HAdV-1 was slightly different from that for MS2 and AIV.

For fluorescence intensity, the uncertainty with impactor stage samples was much lower than that with nebulizer samples, with the latter even larger than that with the total virus concentrations. The reason could be that the concentration of fluorescein in the nebulizer fluid was too high for the spectrofluorometer to measure directly, thus requiring more diluting and transferring steps of tiny amounts of fluid. As a result, the normalized fluorescence intensity may not be more accurate or repeatable than the normalized total virus concentration in this study.

Note that all repeatabilities were calculated based on one sample. Thus it only included the factors in the sample analysis procedures. A great part of the variations in the viral aerosol test results could be attributed to the factors in the aerosol test procedure, including the variations of temperature and humidity. These factors, however, should increase the uncertainties of live virus titer, total virus concentration and fluorescence intensity by the same rate, thus should not affect the comparison results.